UNIVERSITÀ DEGLI STUDI DI PALERMO

Corso di Dottorato di Ricerca in
"Energia e Tecnologie dell'Informazione - curriculum Fisica Tecnica e Ingegneria Nucleare"
Dipartimento di Ingegneria
Settore Scientifico Disciplinare ING-IND/19

MULTIPHYSICS OPTIMIZATION FOR WATER-COOLED BREEDING BLANKET DESIGN ENHANCEMENT

IL DOTTORE
RUGGERO FORTE

IL COORDINATORE
CH.MO PROF. MAURIZIO CELLURA

IL TUTOR
CH.MO PROF. PIETRO ALESSANDRO DI MAIO

CICLO XXXIII
ANNO CONSEGUIMENTO TITOLO 2020

To Marina, who unconditionally supports me in every choice I make.

To my parents, who have taught me to work hard for the things that I aspire to achieve.

Contents

List of Figures

List of Tables

Acronyms

EFDA European Fusion Development Agreement

H2020 Horizon 2020

DEMO DEMOnstration fusion power reactor

KDII Key Design Integration Issue

BB Breeding Blanket

BOP Balance of Plant

FW First Wall

TBR Tritium Breeding Ratio

WCLL Water-Cooled Lithium Lead

FEM Finite Element Method

D-T Deuterium-Tritium

HCPB Helium-Cooled Pebble Bed

WCLL Water-Cooled Lithium Lead

RAFM Reduced-Activation Ferritic/Martensitic

SB Segment Box

SW Side Wall

BP Back Plate

BZ Breeding Zone

BSS Back Supporting Structure

VV Vacuum Vessel

LOCA Loss Of Coolant Accident

CB Ceramic Breeder

NMM Neutron Multiplier Material

PWR Pressurized Water Reactor

SP Stiffening Plate

DWT Double-Walled Tube

HLM Heavy Liquid Metal

DBTT Ductile-to-Brittle Transition Temperature

TTS Transition Temperature Shift

MHD Magneto-Hydro Dynamics

CFD Computational Fluid Dynamics

CHF Critical Heat Flux

COB Central Outboard Blanket

DNB Departure from Nucleate Boiling

NO Normal Operation

OP Over-Pressurization

SL Supporting Line

Nomenclature

α	thermal expansion coefficient
Δp	pressure drop
$\Delta\varepsilon$	strain range
$\dot{m}$	mass flow rate
$\dot{\varepsilon}$	Uniaxial strain rate
$(\sigma)_b$	bending component of the stress
$(\sigma)_m$	membrane component of the stress
ν	Poisson modulus
$\overline{\sigma}$	equivalent Von Mises stress
ρ	density
σ	uniaxial stress
σ_{ij}	component of the stress tensor
ε	uniaxial strain
ζ	coefficient of fluid resistance
A	Norton material specific constant
C	Larson-Miller Parameter material specific constant
D_h	hydraulic diameter
E	Young modulus
f	Fanning friction factor
h	heat transfer coefficient
Ja	Jacob number

n	Norton stress exponent
Nu	Nusselt number
P	Larson-Miller Parameter
Pr	Prandtl number
r	random number between 0 and 1
R_0	bend radius
$R_{m,min}$	minimum tensile strength
$R_{p02,min}$	minimum yield strength
Re	Reynolds number
S	allowable stress
T	Temperature
t_r	time-to-rupture
U	creep usage factor
u	fluid velocity
V	fatigue usage factor
W	creep rupture usage factor
x_i	design variable
x_i^l	lower limit of the design variable
x_i^u	upper limit of the design variable
$\mathbf{F}$	peak stress tensor
$\mathbf{P}$	primary stress tensor
$\mathbf{P}_b$	primary bending stress tensor
$\mathbf{P}_L$	local primary membrane stress tensor
$\mathbf{P}_m$	primary membrane stress tensor
$\mathbf{Q}$	secondary stress tensor
$\mathbf{X}$	design vector

$\mathbf{X}_{end}$ array of the final complex

$\mathbf{X}_{h}$ complex point with highest objective function value

$\mathbf{X}_{i}$ i^{th} complex point

$\mathbf{X}_{r}$ reflected complex point

$\mathbf{X}_{start}$ array of the initial complex

c_p specific heat at constant pressure

k thermal conductivity

q''' volumetric density of heat power

q'' surface heat flux

Disclaimer

This work has been carried out within the framework of the EUROfusion consortium and has received funding from the Euratom research and training programme 2014-2018 and 2019-2020 under grant agreement No 633053.

The views and opinions expressed herein do not necessarily reflect those of the European Commission.

Abstract

The commercial feasibility of the first fusion power plant generation adopting D-T plasma is strongly dependent upon the self-sustainability in terms of tritium fueling. Within such a kind of reactor, the component selected to house the tritium breeding reactions is the breeding blanket, which is further assigned to heat power removal and radiation shielding functions. As a consequence of both its role and position, the breeding blanket is heavily exposed to both surface and volumetric heat loads and, hence, its design requires a typical multiphysics approach, from the neutronics to the thermo-mechanics. During last years, a great deal of effort has been put in the optimization of the breeding blanket design, with the aim of maximizing the tritium breeding and heat removal performances without undermining its structural integrity. In this dissertation, a derivative-free optimization method named "Complex method" is applied for the design optimization of the European DEMO Water-Cooled Lithium Lead breeding blanket concept. To this purpose, a potential tritium production performances-based objective function is defined and a multiphysics model of the blanket is developed inside COMSOL environment in order to solve the coupled thermo-mechanical problem, while the optimization algorithm implemented in MATLAB leads the design towards a minimum optimum point compliant with the prescribed requirements. Once the optimized design is obtained, its nuclear, thermal-hydraulic and structural performances are assessed by means of specific neutron transport and multiphysics simulations, respectively. Finally, the structural integrity is verified by means of the application of the RCC-MRx design criteria.

Introduction

With the aim to both reduce CO_2 emissions and satisfy the constant increasing of energy demand, the development of technologies targetting the exploitation of nuclear fusion to obtain electric energy has been pursued a lot by European Union during last years. In 2013, the European Fusion Development Agreement (EFDA) published the first Fusion Roadmap: *Fusion Electricity – A roadmap to the realisation of fusion energy*, a fundamental document to align the priorities in fusion research and development towards the ultimate goal of achieving electricity from fusion energy.

During the last framework programme funding research *Horizon 2020* (H2020), EFDA has been replaced by EUROfusion, a consortium of national fusion research institutes located in the European Union, Switzerland, Ukraine and UK, acting as the "umbrella" organisation of Europe's fusion research laboratories. The EUROfusion consortium funds fusion research activities in accordance with an updated version of the above-mentioned roadmap, renamed as *European Research Roadmap to the Realisation of Fusion Energy* [1]. The main steps outlined in the roadmap to achieve the leading goal by means of a fusion magnetic confinement machine can be summarized as follow:

1. Technical demonstration of large scale fusion power – this is the first goal of ITER machine [2] (500 MW for 400 seconds);

2. Electricity delivered to the grid via a DEMOnstration Fusion Power Plant (DEMO) which would generate, early in the second part of this century, hundreds of MW of electricity for several hours and operate with a closed fuel cycle and include other features that could be extrapolated to early commercial fusion power plants;

3. In parallel, a science, technology, innovation and industry basis to allow the transition from the demonstration fusion plant to affordable devices suitable for large-scale commercial deployment (stellarators might prove particularly attractive);

4. Large scale industrial production of fusion plants.

Financed during H2020, EUROfusion consortium has carried out the pre-conceptual design of the European DEMO machine, indicating the road for the next conceptual design phase to be conducted during the next Framework Programme for Research and Technological Development 2021-2027 (FP9), *Horizon Europe*.

During the pre-conceptual phase, different DEMO design options have been explored, focusing on a design integration approach based on systems engineering, which had to start from day one to classify and face several engineering and operational issues, and prioritise the proper technology and physics research activity [3]. In fact, the selection of suitable plant design parameters and technical characteristics of the systems begins with the definition of the plant requirements and implicates some compromise between technological advantages and practical hazard issues related to the different design choices. These kind of design options involve so many plant features that they have a considerable impact on a lot of systems and, for this reason, they must be selected with a full integration view, in such a way to make risks, design problems and overall complexity to decrease together with costs.

In particular, eight design issues, the so-called *Key Design Integration Issues* (KDIIs), have been identified for being analysed during the pre-conceptual design phase, as their impact on whole plant design architecture, safety, maintainability and licensing might be crucial [4]. Focusing on the KDII-2 reported in [4] and named as *Breeding Blanket design and ancillary systems: helium or water as a coolant*, one of the most challenging choices to be made in the further development of the DEMO machine is the one regarding the coolant selection for the Breeding Blanket (BB) system.

Due to the high number of ancillary systems that are linked to the BB, the choice of the coolant plays a key role in the integration aspects for DEMO, influencing the whole plant architecture, with significant effects on several design issues such as integration, maintenance and safety. The choice of the coolant for the BB is still under discussion and two options are presently considered: water and helium. Technical issues having an impact on this choice encompass [5]: (a) thermal power conversion efficiency; (b) pumping power requirements; (c) required power handling capabilities of the blanket First Wall (FW); (d) mechanical properties of the structural material under irradiation; (e) neutron shielding requirements; (f) achievable Tritium Breeding Ratio (TBR); (g) tritium extraction from the breeder; (h) tritium permeation, inventory and control; (i) chemical reactivity, coolant leakages and chronic release; (j) design integration and feasibility of Balance of Plant (BoP); (k) design of safety system.

My research activity carried out during the XXXIII cycle of the Ph.D. course in Energy and Information Technologies takes place within the framework of the

R&D activities on the DEMO Breeding Blanket, promoted and supported by the EUROfusion Consortium. In particular, the main topic of the research activity concerns the development of a multiphysics tool to be used for design enhancement of the water-cooled breeding blanket concept foreseen for DEMO, taking into account its nuclear, thermal-hydraulic and thermo-mechanical design aspects. During last years, a great deal of effort has been put in the optimization of the water-cooled breeding blanket concept, with the aim of maximizing the tritium breeding and heat removal performances without undermining its structural integrity.

In this dissertation, a derivative-free optimization method named *Complex Method* has been applied for the design optimization of the European DEMO Water-Cooled Lithium Lead (WCLL) breeding blanket concept. To this purpose, a potential performances-based objective function has been defined and a specific multiphysics model of the blanket concept developed inside a Finite Element Method (FEM) code environment in order to solve the coupled thermo-mechanical problem, while the optimization algorithm has led the design towards a minimum optimum point compliant with the prescribed requirements. Once obtained the optimized design, its nuclear and thermo-structural performances have been investigated with more detailed numerical models, highlighting the improvements achieved as well as the remaining issues to be solved in the next future.

The research activity described in this dissertation has been carried out during my Ph.D. course from the end of 2017 to the second half of 2020, at both University of Palermo and University of California, Los Angeles (UCLA), where I spent a six-months period as a visiting researcher.

Chapter 1

Fusion Reactor Blankets

1.1 Introduction

Since when nuclear fusion reactions have been investigated to be exploited to produce energy, magnetic confinement machines such as the TOKAMAK have been considered as the most feasible and competitive option to heat up and confine very high temperature plasma.

TOKAMAK machines such as ITER and DEMO use very strong magnetic fields to confine ions and electrons within the toroidal plasma chamber, making high rates of fusion reactions occur and protecting, at the same time, the integrity of the structures around. The reference nuclear fusion reaction to be exploited in future fusion power plant is the Deuterium-Tritium (D-T) reaction [6].

While deuterium is moderately easy to supply and manage, tritium is not. Being radioactive with a relatively short half-life (12.32 years), its supply and management represent one of the toughest challenges in the development of future fusion power plants. The potential solution figured out by the scientific community is to produce tritium on site, and specifically inside one of the plasma facing components of the machine.

1.2 Main Functions and Design Requirements

The structure immediately surrounding the majority of the fusion reaction chamber is called *blanket* and carries out several functions, among which are the following: (a) to sustain a sufficiently clean plasma domain, (b) to recover energy from the emitted radiation and reaction products, (c) to shield the surrounding structures and personnel, and (d) to breed the tritium required in a D-T reactor (*breeding* blanket).

Such component plays a pivotal role for the operation of the machine. In fact, while the fusion reaction region is generally maintained at plasma condition such

that (at the best) an energy self-sufficient reaction chain is established, it is indeed in the blanket where neutron and radiation energy released from plasma are deposited, and which will finally provide the energy transformable for external utilization. Hence, the blanket has to be composed of materials that well withstand the neutron damage, without compromising the purity of the plasma (i.e. low sputtering effect), as well as keep good thermal-mechanical properties under high-energy neutron irradiation. Moreover, the blanket is considered as the first barrier to shield the external components and personnel from plasma radiation. This is a very relevant aspect in a TOKAMAK machine since, for instance, the superconducting magnets might be very sensitive even to extremely low external heating and undergo to several failures if not well shielded. As to the energy transferred from, it has to be equipped with a proper cooling system able to remove efficiently the heat power therein deposited and/or generated. In fact, the competitiveness in the energy market of future fusion reactors will also be strongly dependent upon the global effectiveness of the power conversion system of the whole plant.

Finally, the necessity of breed tritium forces the blanket design to foresee the presence of a certain amount of lithium, either as a pure substance or in compounds, so that neutrons emitted by plasma are captured by the lithium to produce tritium, by means of both the following nuclear reactions:

$$n + {}^{6}Li \longrightarrow T + \alpha \tag{1.1}$$

$$n + {}^{7}Li \longrightarrow n + T + \alpha \tag{1.2}$$

In Figure 1.1, a schematic view of the blanket concept for magnetic fusion reactors is shown, highlighting the three main functions of shielding, tritium breeding and heat power removal.

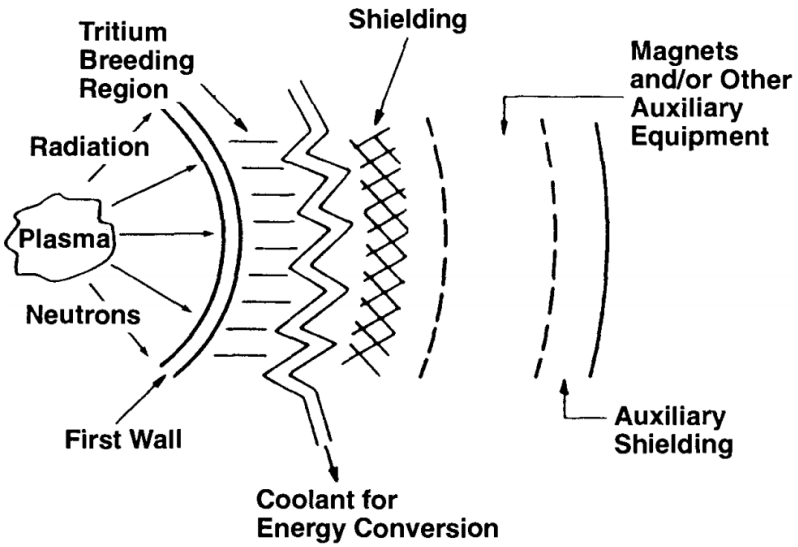

Figure 1.1: Blanket concept scheme for magnetic fusion reactors [6].

1.3 General Design Description

As stated before, the blanket covers the major part of the plasma facing region inside a TOKAMAK machine ($\approx 80\%$). The remaining part is covered by Divertor, and other systems such as the ones responsible for Heating and Current Drive and Diagnostics. For the sake of brevity, only the most advanced existing blanket concepts will be presented in this section: the ITER blanket and the two breeding blanket concepts under investigation for the European DEMO.

1.3.1 ITER Blanket

The ITER blanket differs from the blanket concept to be installed in the future fusion power plant: it does not have to breed tritium. In other words, the ITER blanket will not be a *breeding* blanket, and not contain any breeder material. The two remaining functions are, hence, the removal of the heat power deposited in it, and the shielding of the external components.

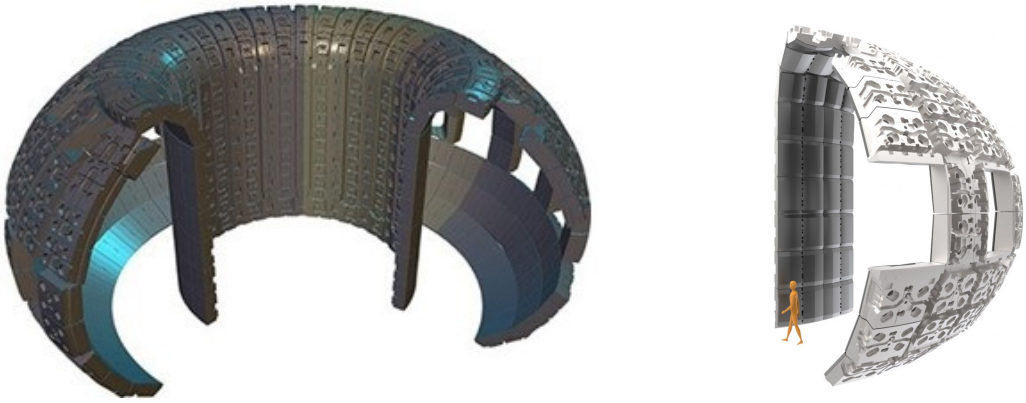

Figure 1.2: ITER Blanket (left) and Blanket sector (right) [2].

As shown in Figure 1.2, the ITER blanket is composed of 9 sectors, each one subdivided into modules, both in inboard and outboard side. Each module is composed of two main parts: the shielding block and the FW panel, as reported in Figure 1.3.

The former is conceived as a stainless steel water-cooled structure to sustain the FW panel and contribute to both thermal and nuclear shielding of the vacuum vessel, superconducting magnets and other outer vessel components. Its cooling system is made of a complex network of cooling channels and plates, wherein coolant flows to remove the nuclear heating deposited.

The FW panel is, instead, a multi-metallic water-cooled structure designed to withstand heat and particle fluxes arising from plasma during normal and transient loading operations. The FW is composed of a stainless steel central poloidal beam and a system of toroidally oriented plasma facing units, articulated into two symmetric wings and structurally sustained by the poloidal beam. Each

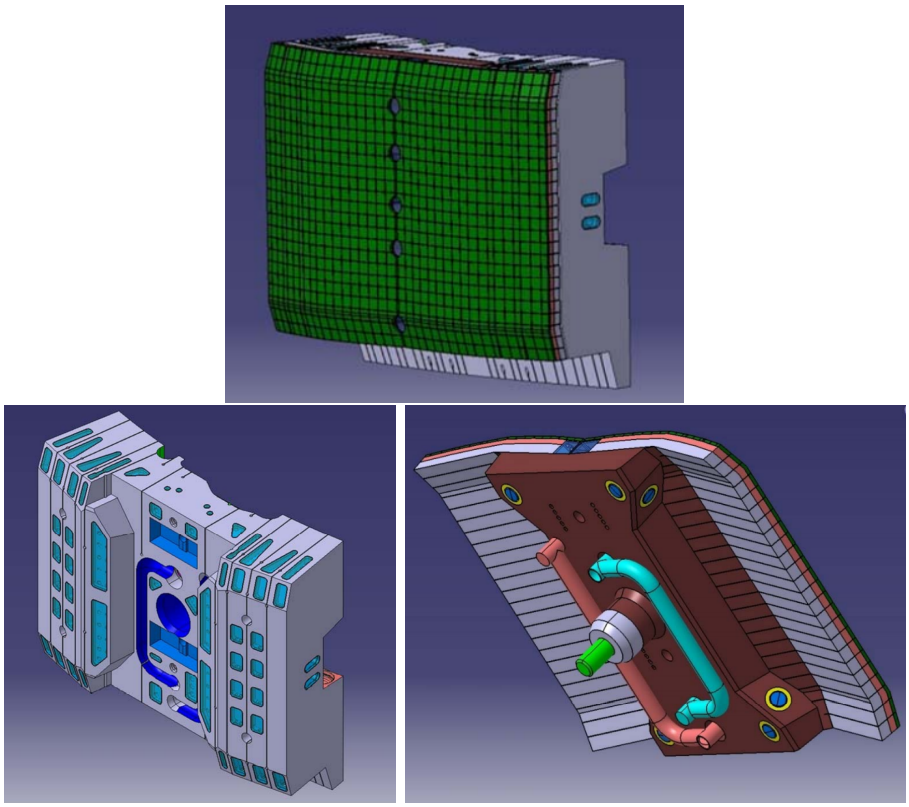

Figure 1.3: ITER Blanket module (top). Shielding block (bottom left). FW panel (bottom right) [7].

unit, also named *finger*, is made of three different layers (i.e. stainless steel, copper-chromium-zirconium and pure copper) covered with beryllium tiles.

In particular: the stainless steel provides for mechanical robustness and structural integrity under the effects of heavy thermal and mechanical loads; the CuCrZr acts as a heat sink showing a very high thermal conductivity as well as strength at high temperatures; the Cu is placed as an interlayer between the heat sink and the Be tiles, which has been chosen as a plasma-facing material mainly thanks to its low atomic number, low sputtering and high thermal conductivity.

As to its cooling circuit, each finger is equipped with a circular tube inside the steel layer to mainly remove the nuclear heating, and with either two circular tubes or a *hypervapotron* channel, depending upon the type of module (i.e. Normal or Enhanced Heat Flux), to cool down the plasma facing region exposed to high heat flux ($1 \div 4.7$ MW/m^2) [7]. In Figure 1.4, the structure and a cross section of a FW finger for Normal Heat Flux type are depicted.

Although the main blanket is not *breeding*-type, ITER reactor will also be equipped with a Test Blanket System [9] that is going to be pivotal for the development of fusion energy. In particular, such system will house four different Test Blanket Modules (relying on different tritium breeding concepts) to be tested in dedicated *ports* in the vacuum vessel. Another main experience to get from ITER exploitation will be, thus, to evaluate the tritium breeding performances of different

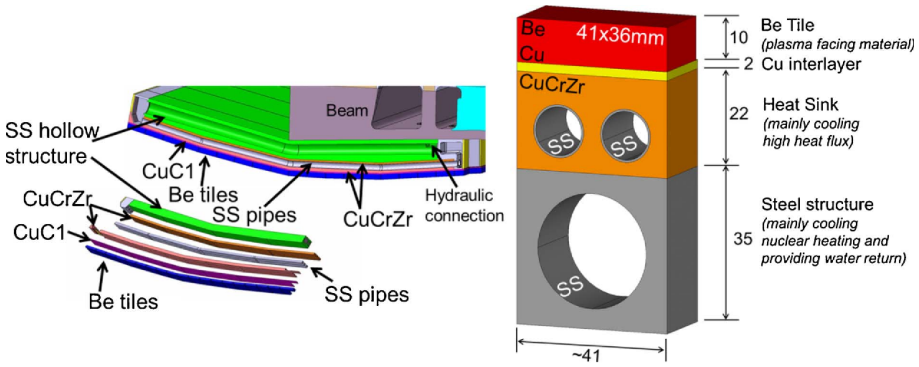

Fig. 1. NHF finger structure and cross section (units in 'mm').

Figure 1.4: ITER FW finger structure and cross section (Normal Heat Flux type) [8].

breeding blanket concepts and obtain important data for the design development of the future DEMO breeding blanket.

1.3.2 DEMO Breeding Blanket

As far as the DEMO blanket concepts are concerned, their design shows many differences with respect to the ITER blanket, mainly due to the tritium breeding requirement.

Nowadays, two breeding blanket concepts are being investigated for DEMO: the Helium-Cooled Pebble Bed (HCPB) concept, the Water-Cooled Lithium Lead (WCLL) concept. The former adopts helium as coolant and make use of a solid ceramic lithium with beryllium/beryllides material as breeder and neutron multiplier, whereas the latter is cooled by pressurized sub-cooled water and foresees an eutectic lithium-lead (PbLi) liquid mixture as breeder and neutron multiplier. Despite of their intrinsic differences, the two concepts share a common architecture that relies on the same DEMO baseline: breeding blanket toroidally distributed in 16 sectors, each one composed of two inboard and three outboard segments. Furthermore, both concepts rely on the use of Eurofer97, a Reduced-Activation Ferritic/Martensitic (RAFM) steel, as structural material.

Regarding the segment architecture, each segment is conceived as a single module and made up of a poloidally continuous steel external box named as Segment Box (SB) and composed of FW, Side Walls (SWs), caps and Back Plate (BP), that houses the Breeding Zone (BZ), where almost all the tritium breeding reactions occur. Behind the SB, manifolds and a Back Supporting Structure (BSS), which acts as a backbone supporting the entire segment, connect the module to the Vacuum Vessel (VV). Moreover, the FW plasma-facing surface of DEMO blanket is covered by a 2mm-thick tungsten layer, also called *W-armour*.

As to the current HCPB BB concept [10], it relies on the use of Li_4SiO_4+35%Li_2TiO_3 pebble beds to breed tritium and on hexagonal prismatic

blocks of $Be_{12}Ti$ as neutron multiplier. Helium is used as both coolant and purge gas (with 0.1% vol. H_2) to remove out the heat and the tritium, respectively. The HCPB BB internals are shown in cross sections A-A and B-B in Figure 1.5. The BZ volume is delimited by the complex of SW-FW-SW and the BP and houses hexagonal pressure tubes radially arranged to connect the FW with the BP, in order to have sufficient structural stiffness to prevent a failure against an in-box Loss Of Coolant Accident (LOCA).

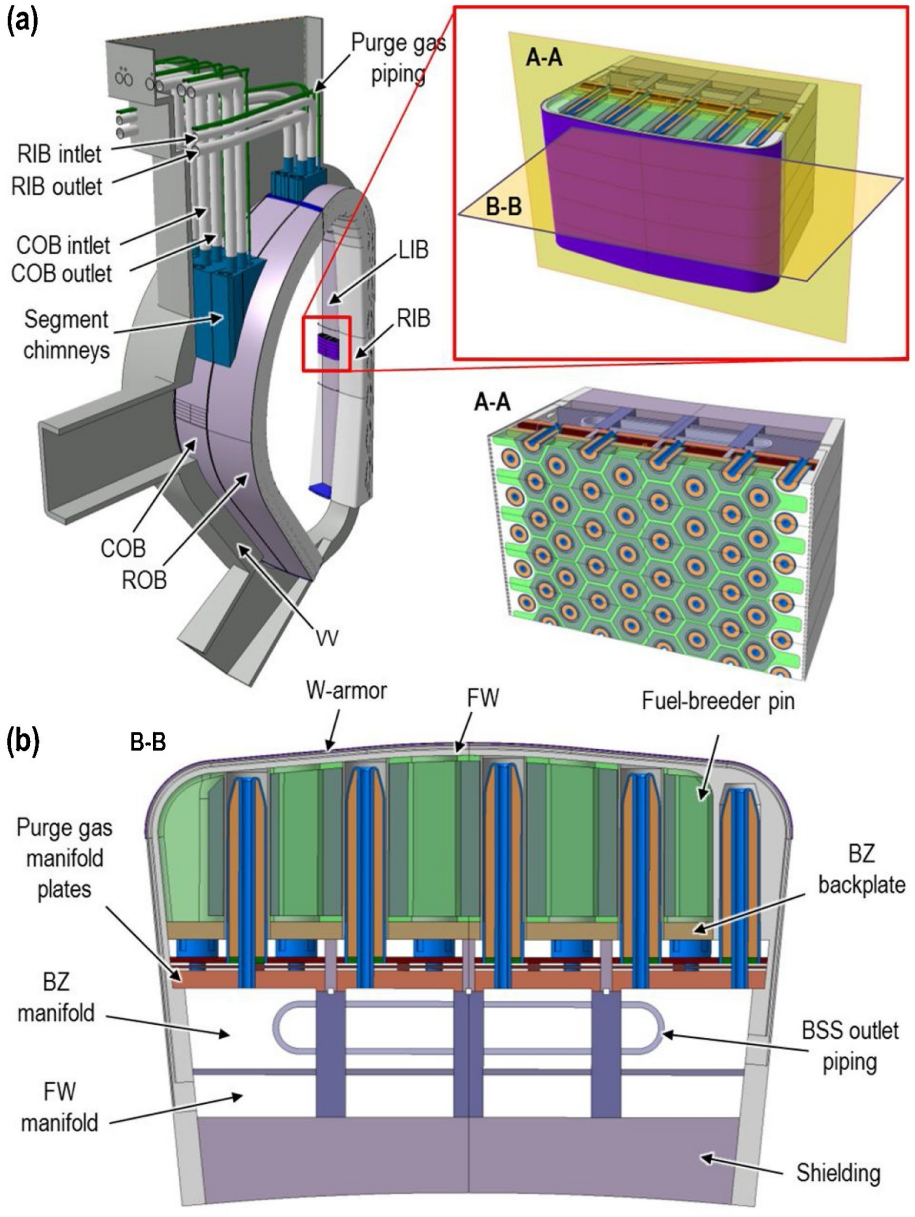

Figure 1.5: DEMO HCPB BB. Design with fuel-breeder pin hexagonal assembly [10].

The so-called fuel-breeder pins are housed into the pressure tubes and connected to the BP. A fuel-breeder pin, as shown on the top of Figure 1.6, is composed of a system of two coaxial cylinders, namely the outer and inner cladding, delimiting an

annular region filled with a tritium Ceramic Breeder (CB) material, the so-called *KALOS CB*, in form of a pebble bed (pebble size 250 µm to 1250 µm). It contains lithium enriched in ^{6}Li at 60% to ensure enough tritium breeding performances. An advantage of the fuel pin configuration is that the enrichment in a pin can be easily tailored along the radial direction of the pin, e.g. increasing the ^{6}Li content at the back of the pin to effectively tune and further enhance the radial distribution of tritium breeding, nuclear heating and temperature distribution. The $Be_{12}Ti$ has been selected as Neutron Multiplier Material (NMM) to improve tritium breeding with enhanced safety features. As discussed in [11], the $Be_{12}Ti$ is in form of hexagonal prismatic blocks with a central bore, where the corresponding pressure tubes take place. Tritium is produced in both CB and NMM and it is extracted out

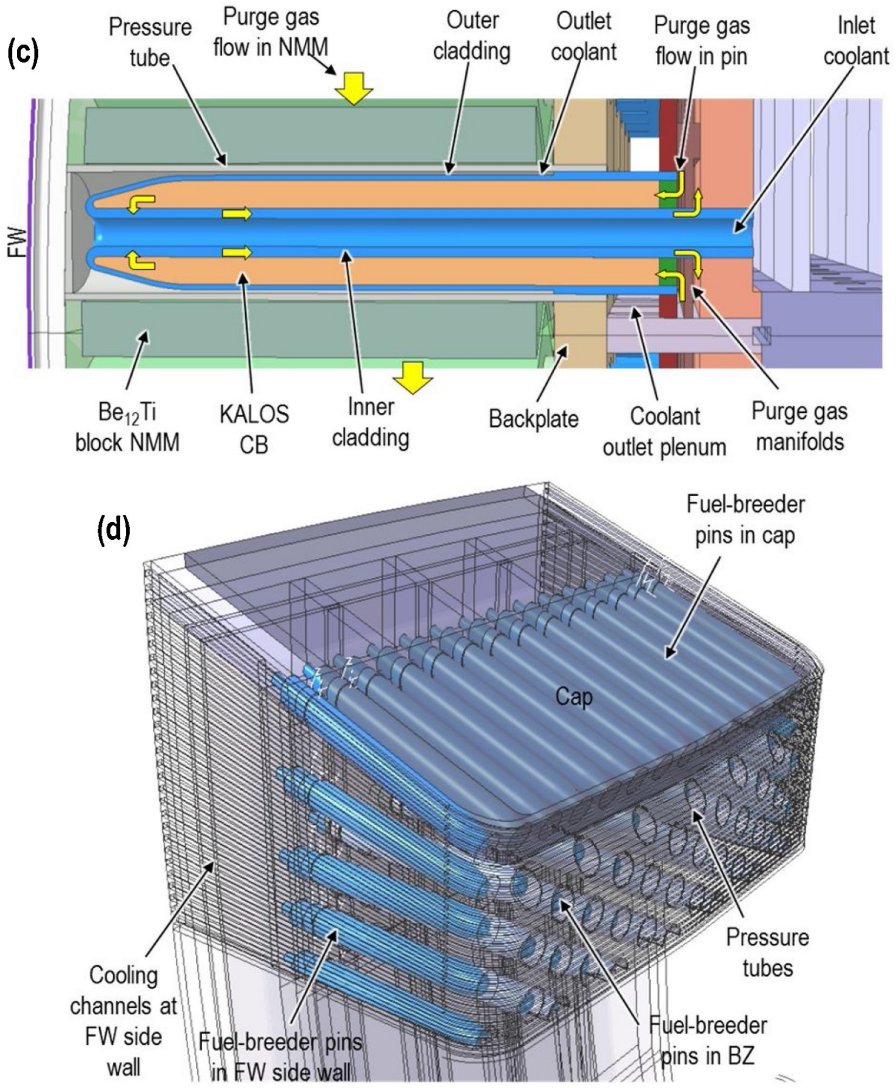

Figure 1.6: DEMO HCPB BB. Fuel-breeder pin (c); Detailed view of the segment top cap (d) [10].

of the segments by means of a purge gas, that enters the NMM prismatic blocks first and sweeps them from top to bottom. In a second step, the purge gas enters

the pins (all connected in parallel), flushing the CB beds from the BP to the front of the pins. The purge gas is collected into ducts machined in the 6 mm thick inner cladding and it is directed to the purge gas outlet manifold, on its way out of the segment (see Figure 1.5). As stated above, Helium is used to remove the heat power deposited and cool down the blanket structures.

The complex of FW-SWs, subjected to both surface (heat flux) and volumetric (nuclear heating) heat loads, is cool down by the presence of internal square cooling channels (11x11 mm), able to withstand a heat flux of around 0.3 MW/m^2 under nominal operating conditions [11]. The BZ cooling is provided by the coolant flowing inside the coaxial tubes, as shown in Figure 1.6.

The coolant temperature window is set then to 300–520 °C. The main drawbacks of gas cooling are compressibility and low density, that can result in large parasitic plant power re-circulation if attention is not given to reduce the pressure drop and limit its heat transfer capability [12]. In order to enhance the heat transfer with a limited penalty on pressure losses, the adoption of turbulence promoters (i.e. augmented heat transfer structures) is essential.

The segments are closed on top and bottom with the so-called caps (see Figure 1.6). These components are basically thick plates (provisional thickness of around 100 mm) in which deep holes are drilled radially in order to house fuel-breeder pins. The cap makes thus the function of a row of (connected) pressure tubes, it is directly cooled by the same coolant as the pins and serves as structural element against in-box LOCA. The lateral pins at the SWs, as well as the FW cooling channels, are varied in their orientation in order to have a moderate transition from the segment to the cap region, thus avoiding large uncooled regions at the SWs.

As far as the WCLL BB concept design [13] is concerned, different solutions have been adopted due to totally different features and performances between either the coolants and the breeder materials. The WCLL BB foresees the adoption of water acting as coolant and a liquid eutectic alloy of Pb and Li (the latter at 17%) as neutron multiplier (Pb), breeder material (Li) and tritium carrier. The coolant is pressurized sub-cooled water undergoing a thermal cycle very similar to the one adopted in the well-known fission Pressurizer Water Reactor (PWR), with an operating pressure of 15.5 MPa and inlet/outlet temperatures of 295 °C/328 °C.

The SB of the WCLL BB concept is basically equivalent to the HCPB one, but equipped with slightly higher thicknesses due to the higher operating coolant pressure (15.5 MPa vs 8 MPa). In Figure 1.7, the WCLL BB internals are shown. The BZ, reinforced by Stiffening Plates (SPs), consists of the liquid breeder and its cooling system, articulated in submerged bundles of Double-Walled Tubes (DWTs), made of Eurofer97. A structure composed of both cooling water and breeder manifolds and the BSS is finally attached to the BP. According to such design, each segment can be conceived as made of a poloidal repetition of *elementary cells*,

delimited by two consecutive toroidal-radial SPs, except for the top and bottom caps whose design should be determined "ad hoc" [14]. The SW-FW-SW cooling is

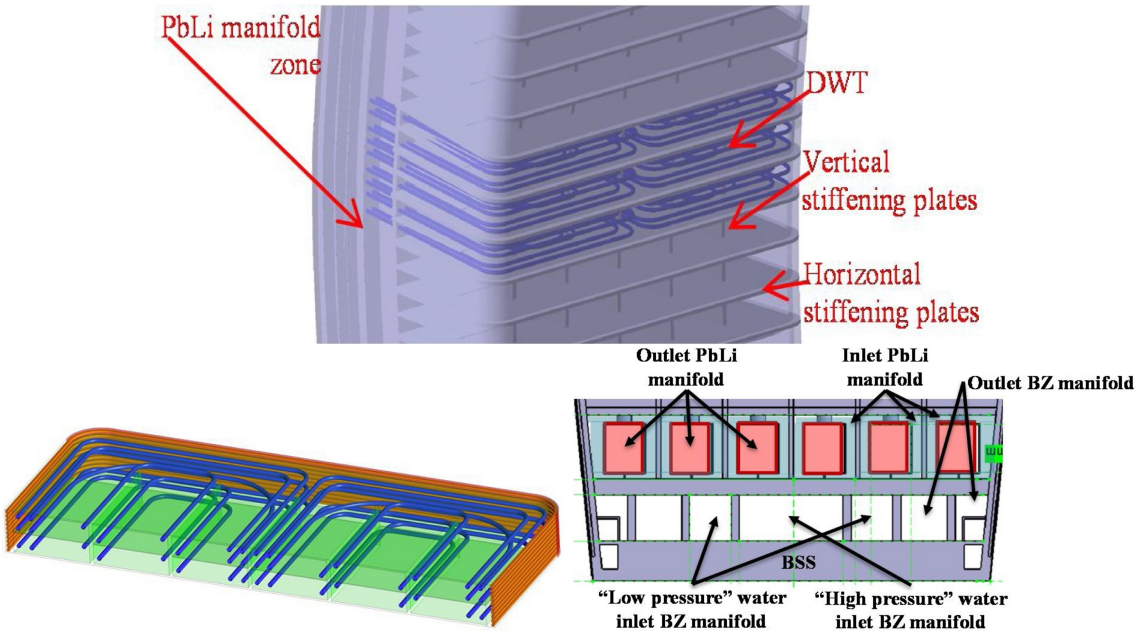

Figure 1.7: DEMO WCLL BB. Outboard segment (top). Elementary breeding cell (bottom left). Rear region of Inboard segment (bottom right) [13].

provided by internal square cooling channels (7x7 mm) where water counter-current flow occurs, whereas the BZ cooling is mainly in charge of the DWTs, where water flows in and undergoes the same thermal rise as the FW cooling circuit. Such DWTs have been selected in order to reduce crack propagation inside the tube wall and prevent the dangerous water-Heavy Liquid Metal (HLM) chemical reaction, which is exothermic and potentially catastrophic for such component [15].

An internal grid of SPs is necessary in order to guarantee the structural integrity of the SB in case of thermo-mechanical and electro-magnetic loads postulated during normal, off normal and accidental conditions (e.g in-box LOCA). As to the latter, following a rupture of one (or more) DWT, the SB undergoes a consequential over-pressurization from the liquid breeder operating pressure of 0.5 MPa to the cooling water one of 15.5 MPa, plus the still unclearly estimated effect of the water-HLM interaction (assumed today as an increase of around 20-25% of the water pressure)[16].

The WCLL BB design is particularly demanding also due to MHD effects on the liquid metal breeder flow. In order to reduce the related pressure drop losses, the PbLi flow path in the blanket is designed to maintain throughout a relatively low velocity (e.g. 13 mm/s in the manifolds and 0.01 mm/s in the BZ) [13].

More details on the WCLL BB design will be given in Chapter 3, where such concept will be the object of the design optimization activity.

1.4 Structural Materials for Fusion Blanket Applications

Owing to high thermal and neutron wall fluxes combined with time-dependent mechanical loads, the choice of the structural material is a pivotal aspect in blanket design.

In a TOKAMAK machine, during normal operation, the plasma does not physically touch the materials directly surrounding it, but those materials are subjected to intense thermal radiation, and to bombardment by 14.1 MeV neutrons, 3.5 MeV α-particles, as well as ions, neutral particles and impurities with relatively low energies (E <10 keV). The high-energy neutrons penetrate deeply into the components enclosing the plasma and contribute additional thermal energy and irradiation damage throughout the volume of the FW/blanket structures by interacting with the associated materials.

The high-energy neutrons interact with the FW/blanket materials by transferring kinetic energy to lattice atoms causing them to be displaced from their lattice sites. Displacement damage is also accompanied by nuclear reactions, which cause transmutation of the atoms of the structural materials into other solid elements and gases, such as He and H [17].

Plasma-facing structures are generally only a few millimeters thick, so the volumetric heating in these materials is small in comparison to the radiative surface-heating component. The magnitude of the surface heat flux depends on the specific design features of the fusion power system, but a comparison of heat fluxes in a variety of technologies and nature is presented in Figure 1.8. The steady-state heat flux on important components of a fusion power system ranges from 1 to 20 MW/m^2. Note, the steady-state heat flux is comparable to that endured by rocket nozzles and requires a highly capable heat transfer system in order to remove these high thermal loads. In addition, to steady-state heat loads, FW materials are also subjected to off-normal plasma events (e.g. plasma disruptions) that deposit extremely large quantities of heat in small regions over a very short period of time. Structural materials for proposed advanced fission power systems (Gen. III$^+$ and Gen. IV) will face many of the same technical challenges that fusion materials will face with respect to the need for resistance to high levels of neutron-induced displacement damage (dpa) and, for cladding, the capability to operate under severe thermo-mechanical conditions of high temperatures and stresses. However, while the experience gained from materials technology for advanced fission reactors is highly pertinent to fusion materials development, there are significant differences. Figure 1.9 illustrates the substantially more demanding service environment that proposed advanced fission and fusion power systems will encounter compared to currently operating nuclear power plants. It is notable that the upper operating

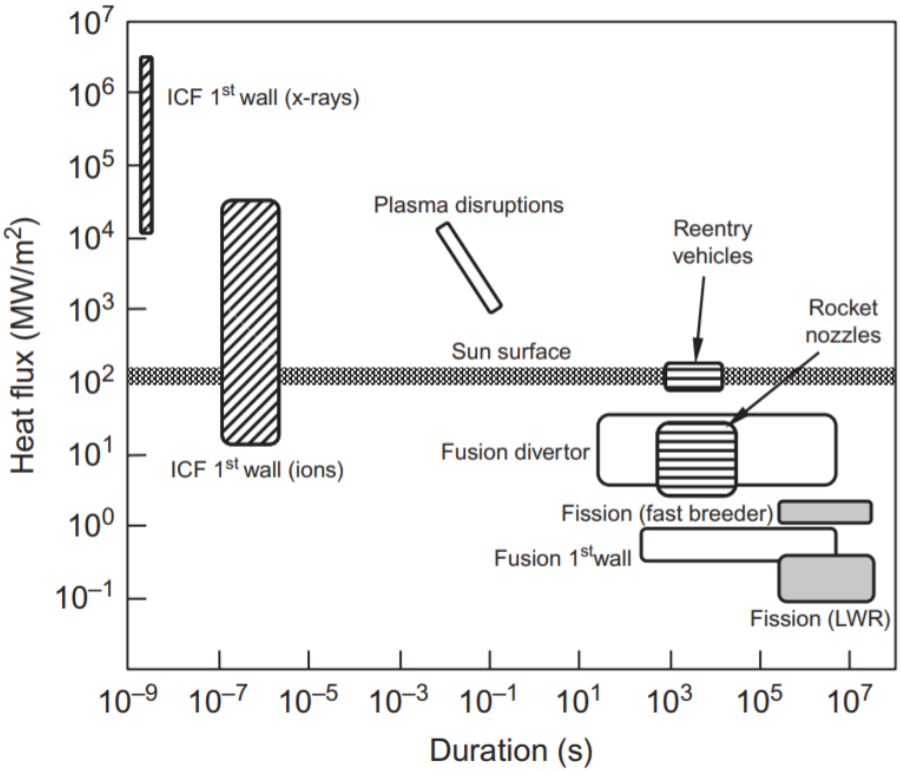

Figure 1.8: Typical steady-state and transient heat fluxes of different systems [17].

temperature limits of advanced fission and fusion systems are hundreds of degrees higher than conventional fission, and the foreseen damage limits are 2–4 times, or more, greater in some cases. Most significantly, the thermo-mechanical structural challenges of fusion systems are singular and unique.

While there are similarities in the fission and fusion operating environments, the 14.1 MeV neutrons produced in the D-T fusion reaction are unique and must be considered. In fact, despite on differences concerning primary knock-on atom energy spectra (almost three times the value obtained in conventional fission reactors [17]), a much more important factor than fission versus fusion displacement damage is that 14.1 MeV fusion neutrons are above the threshold energy for (n,α) and (n,p) transmutation reactions, which cause significant production of He and H.

The effects of high levels of such gas production on the micro-structural stability of FW materials are not fully understood, since no fusion-relevant neutron source exists yet for carrying out experiments to end-of-life doses.

While the fusion nuclear environment is extremely challenging, the fusion thermo-mechanical environment may be even more problematic. As illustrated in Figure 1.8, the steady-state heat flux on the FW is very high, and time varying. Transient heat loads associated with plasma disruptions deposit gigawatts of thermal energy into very small regions of the FW over a very short time. In addition, plasma-facing heat transfer structures are thicker (e.g. few millimeters) and geometrically much more complex than typical fast reactor fuel cladding.

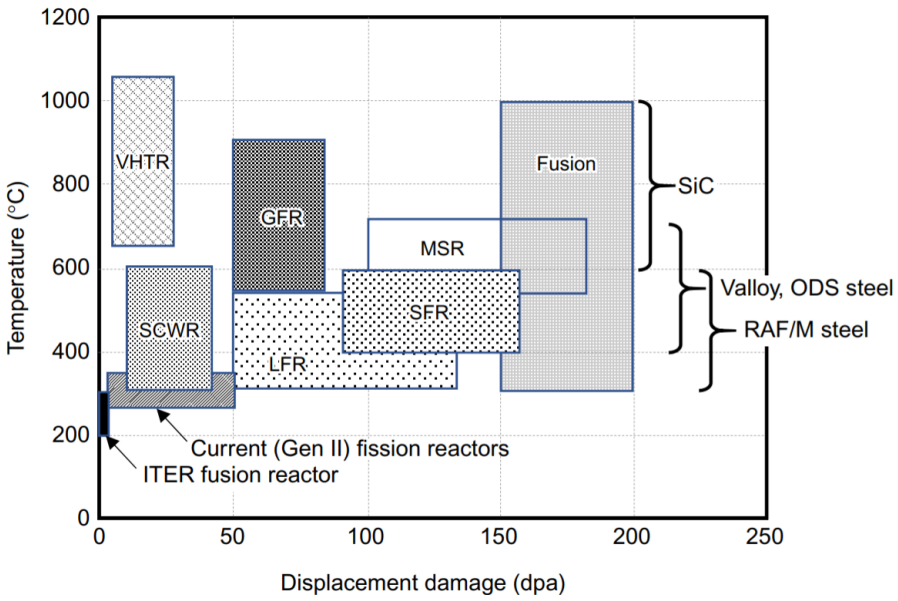

Figure 1.9: Operating temperature vs displacement damage regimes for fission and fusion systems [18].

Although the steady-state heat load on a fusion FW is comparable to that on thin-wall fast-neutron reactor cladding, the thermal stresses in plasma facing and FW components are considerably larger and more complex. Stresses will also arise from differential thermal expansion and radial temperature gradients that occur over distances of meters and in three dimensions. These stresses and strains must be accommodated in massive interconnected structures that must maintain precise dimensional tolerances. The thermo-mechanics is further complicated by spatially varying dimensional instabilities (swelling and creep) and property evolution. This leads to extremely complex time varying stresses and strains.

From Figure 1.9 it is apparent that thermodynamically attractive fusion power reactor structures must operate at temperatures near the thermal creep regime. The combination of severe time varying temperatures and stresses suggests that material degradation mechanisms, such as thermal creep, creep-fatigue, and creep crack growth, will all be much more significant than in a fission system. In summary, it is no exaggeration to state that the ultra-severe thermo-mechanical environment of fusion structures is unprecedented and represents a grand challenge feasibility issue regarding the potential for future fusion power plants.

Another significant challenge that is unique to fusion is the need to control the flow of large quantities of tritium. This will be a huge technical challenge because of the very large inventory of tritium involved, and the potential for significant retention of hydrogen isotopes in irradiated materials.

Finally, the experience of the commercial fission power industry to address the challenge of high-level radioactive waste has motivated development of high-performance materials that minimally impact the environment. Radioactive

isotope inventory and release paths are important considerations in designing for safety. Consequently, a worldwide materials development strategy has emerged that is focused on low or reduced activation materials, including (1) Fe-Cr-based alloys that are RAFM steels, (2) VCrTi alloys, (3) SiC composites, and (4) W alloys.

The leading candidate materials are RAFM steels, which achieve reduced activation compositions by replacement of high activation elements, such as Mo and Nb with V and W. Nowadays, those steels are the most technologically mature FW and breeding blanket structural material, and are the leading candidates for nearer term applications, such as test blanket modules for ITER and advanced plasma devices, such as the proposed Fusion Nuclear Science Facility and DEMO. Some of the advantages enjoyed by these steels over other low-activation alternatives, such as V alloys and SiC composites, include (1) lower cost, (2) the existence of more mature, or many might say the only basically feasible, structural design, and fabrication technologies, (3) compatibility with a wide range of coolants, and (4) resistance to radiation-induced swelling.

Among a wide range of RAFM steels developed throughout the world, the most promising option, both for fast-neutron reactor and fusion applications, was found to be a ferritic/tempered-martensitic steel with a composition in the 7–9Cr range, owing to their superior resistance to degradation from neutron irradiation and significant corrosion and oxidation resistance. While commercial 9Cr-1Mo steels (Grade T91) were first investigated, alloy development efforts, involving compositional modifications, were soon initiated.

Many different kinds of RAFM 7–9Cr steels have been produced in Japan (F82H), Europe (Eurofer97), Korea (ARAA), USA (9Cr-2WVTa), India (INRAFM), Russia (RUSFER) and more recently in China (CLAM) [17]. Their compositions differ slightly, but the various RAFM steels are otherwise generally similar. For the sake of brevity and since the European DEMO relies on Eurofer97, only its chemical composition is reported in Table 1.1. In all cases, 7–9Cr RAFM steels

-	C	S	P	Si	Mn	Ni	Cr	Mo	W
min	0.09	-	-	-	0.20	-	8.5	-	1.00
max	0.12	0.005	0.005	0.05	0.60	0.005	9.5	0.005	1.20
-	Ta	V	Nb	Cu	B	Al	Co	N_2	Fe
min	0.10	0.15	-	-	-	-	-	0.015	Bal.
max	0.14	0.25	0.001	0.005	0.001	0.01	0.005	0.045	Bal.

Table 1.1: Eurofer97 chemical composition in weight% [19].

exhibit a typical microstructure resulting from a two-step final heat treatment: (1) normalization at about 1000 °C for about 0.5 h, and (2) tempering around 750 °C for about 1 h. Of course, the specific temperatures must be optimized for each particular composition.

For fusion reactor applications, the chemical composition and heat treatments applied to the unirradiated steels were designed to optimize the tensile and creep strength up to about 550 °C, which can be considered as their upper temperature limit. The operating temperature window has been, hence, estimated by some to be about 200 °C wide, with a lower operating temperature limit of about 350 °C, governed by irradiation-induced hardening and embrittlement.

Before discussing irradiation-induced changes on the mechanical properties of RAFM steels, we briefly summarize their unirradiated tensile properties. The tensile properties of RAFM steels are close to those of the conventional T91. While these alloys differ slightly in chemical composition, production routes, and final heat treatment, all show relatively similar tensile properties, as shown in Figures 1.10 and 1.11. As can be easily noted, RAFM steels lose their strength at temperatures above around 550 °C.

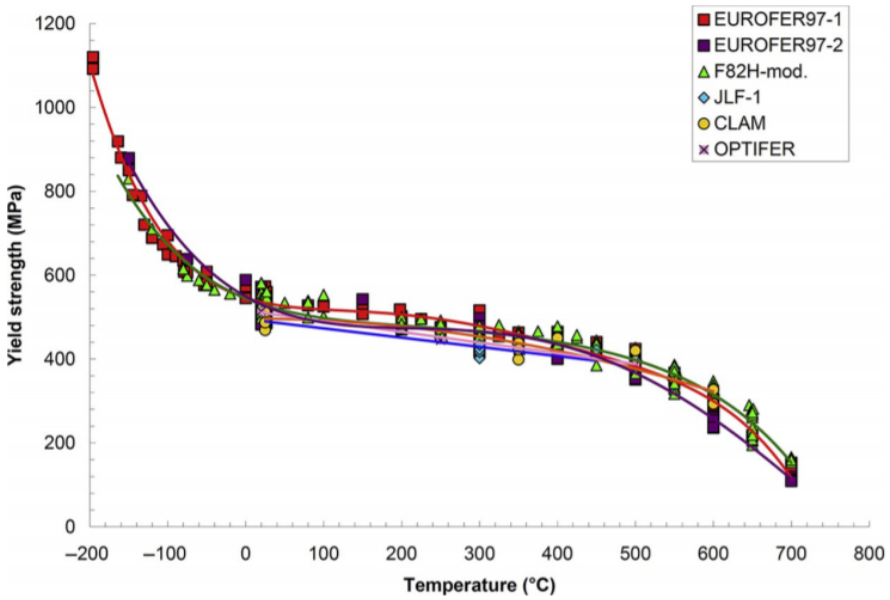

Figure 1.10: Yield strength versus temperature of various unirradiated RAFM steels [20].

As stated above, the lower operating temperature limit (around 350 °C) is governed by irradiation-induced hardening and embrittlement. Figure 1.12 shows the temperature dependence of the tensile yield strength for RAFM steels under irradiated conditions over a range of dpa levels. The data clearly show that irradiation hardens significantly below 350 °C, with yield stress (σ_y) increases ($\Delta\sigma_y$) of up to 600 MPa.

Conversely, as the irradiation temperature increases to 400 °C, or more, hardening falls to low levels and softening may occur at even higher temperatures. Furthermore, experimental evidence indicates that hardening of RAFM steels saturates by a dose of 10 dpa for fission irradiations from 300°C to 335°C, as shown in Figure 1.13.

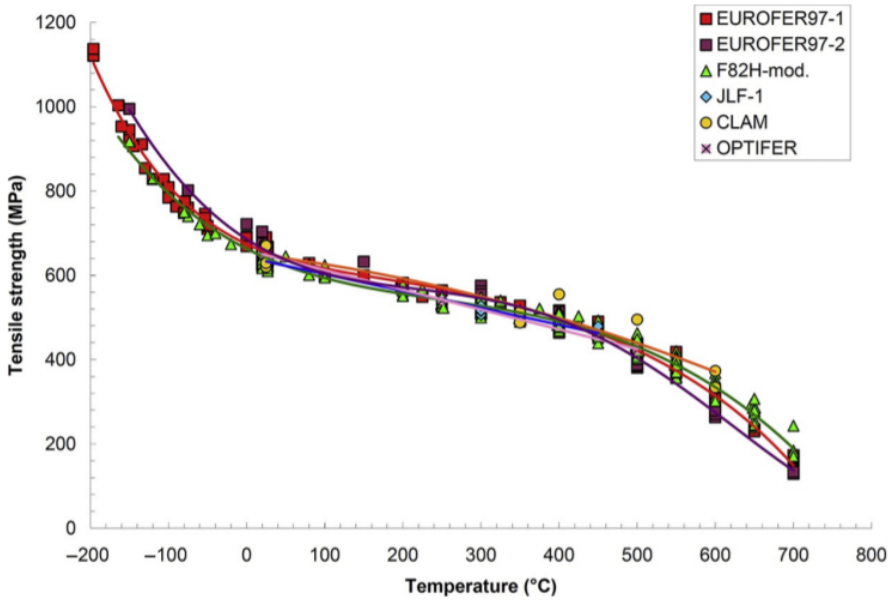

Figure 1.11: Tensile strength versus temperature of various unirradiated RAFM steels [20].

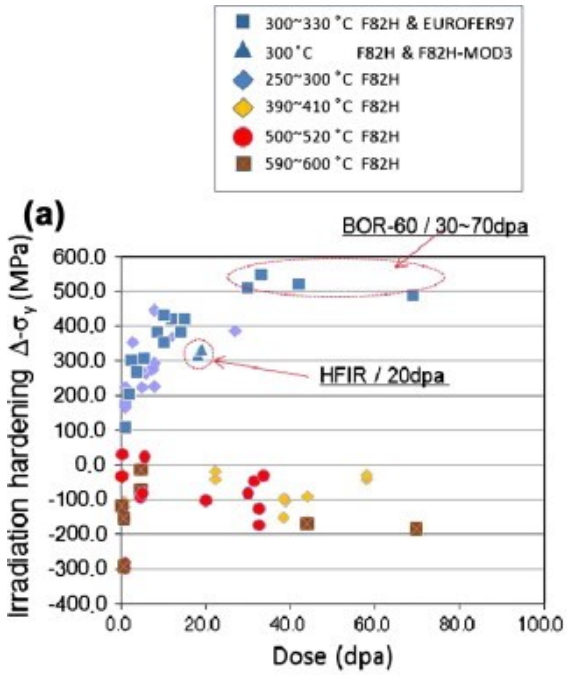

Figure 1.12: Dose dependence of RAFM yield strength at different temperatures [21].

Irradiation hardening is also directly associated with irradiation embrittlement, which manifests itself as a loss of fast fracture resistance, or degraded fracture toughness (K_C). Even in unirradiated conditions, a characteristic of body-centered cubic metals like ferritic steels is a strong temperature dependence of both yield stress and fracture toughness. As the test temperature decreases, these steels undergo a transition in fracture mode from high-energy driven ductile tearing to

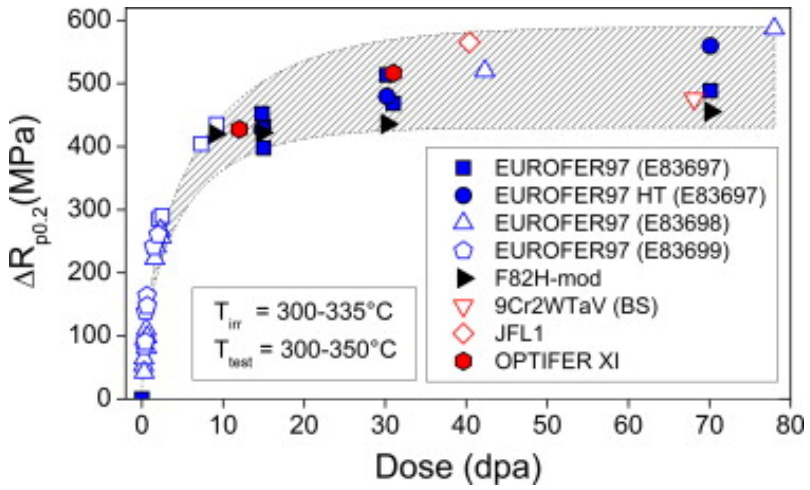

Figure 1.13: Shift of yield strength ($\Delta R_{p,02}$) vs. irradiation dose for Eurofer97 and other RAFM steels for T_{irr}=300–335 °C and T_{test}=300–350 °C [22].

low-energy brittle cleavage fracture. This transition is typically indexed by the so-called Ductile-to-Brittle Transition Temperature (DBTT).

Low-temperature neutron irradiation embrittlement results in increases in the DBTT, or Transition Temperature Shifts (TTS). The TTS depend on irradiation temperature as illustrated in Figure 1.14 for several RAFM steels based on sub-sized Charpy V-notch tests. The magnitude of the TTS is largest up to 330 °C, decreasing sharply at higher temperatures.

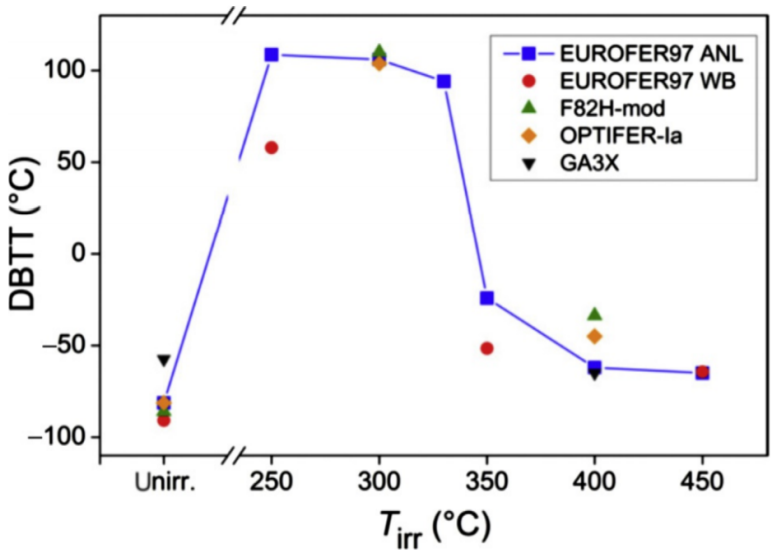

Figure 1.14: Effect of irradiation temperature on the DBTT for several RAFM steels (average neutron dose = 15-16.3 dpa) [22].

At intermediate operating temperatures, irradiation-induced creep and volumetric swelling control the dimensional stability of RAFM steels.

Irradiation creep is a constant volume deformation process in a material subjected to a stress below the static yield stress that is enabled by the displacement

damage-induced supersaturation of vacancies and self-interstitial atoms.

Void swelling is an isotropic volume increase of a material caused by nucleation and growth of internal voids. Ferritic/martensitic steels are much more swelling resistant than austenitic stainless steels, basically due to lower He generation rates caused by the absence of Ni.

At high temperatures (above 400 °C), thermal creep generally arises in RAFM steel. A significant database has been developed on creep rates and creep rupture times of unirradiated RAFM steels Eurofer97 and F82H. Figure 1.15 shows the relation between the minimum creep strain rate and the applied stress for Eurofer97, which is generally described by a power law (or Norton equation) given by,

$$\dot{\varepsilon} = A\sigma^n$$

where A is a material specific constant and n is the Norton stress exponent, indicative of the acting deformation mechanism. Indeed, it is possible to observe that high temperature with low stress corresponds to a low stress exponent (diffusion-based creep), whereas temperatures lower than 550 °C with high stress shows greater stress exponent indicating dislocation-based creep.

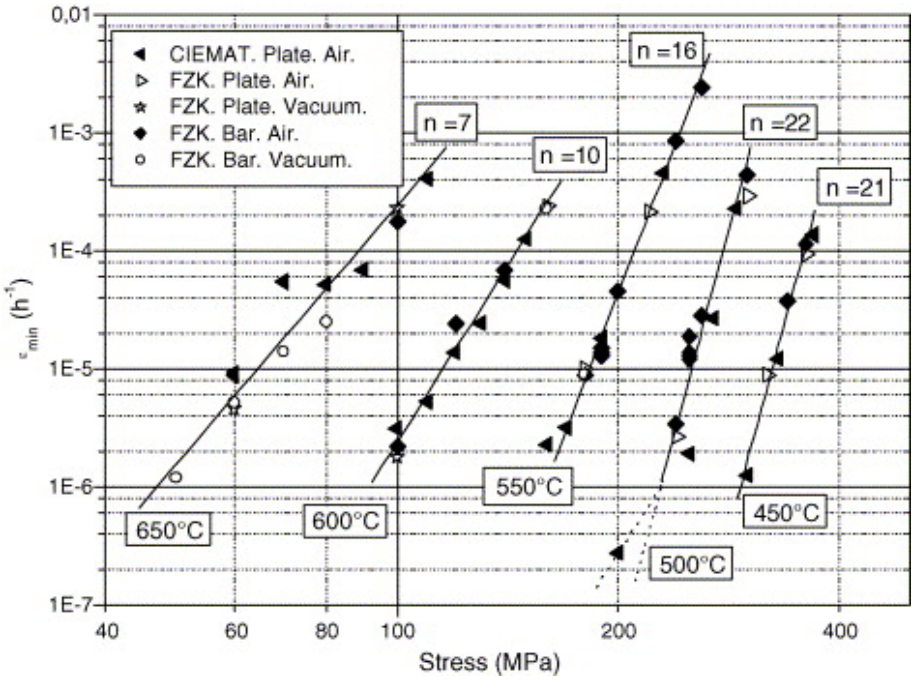

Figure 1.15: Minimum creep strain rate ($\dot{\varepsilon}_{min}$ [h^{-1}]) vs. applied stress for the Eurofer97 steel [23].

Creep rupture times can be drawn from a creep master curve (see Figure 1.16) linking the applied stress to the Larson-Miller Parameter (P or LMP) expressed by,

$$P(or LMP) = T[\log t_r + C]$$

where T is the temperature [°C], t_r is the time to rupture [h] and C is a material specific constant.

From the design point of view, a more practical measure of creep strength is related to the dimensional stability, which is particularly important for fusion structures. The primary plus secondary creep strain limit is typically taken as 1% although this may be higher or lower for a particular component. Instead of time to rupture, creep master curves (stress vs LMP) are built-up considering the time bringing to 1% strain (see [19]).

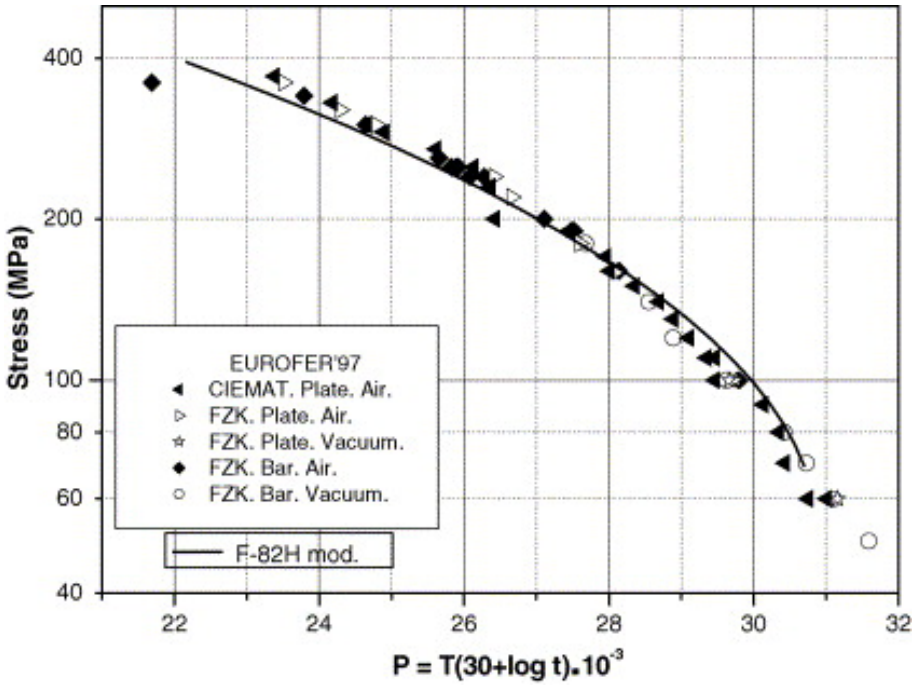

Figure 1.16: Stress vs. Larson–Miller Parameter curves for Eurofer97 and F82H steels (as-received condition) [23].

First-wall structures and components will also be exposed to complex, time varying, thermo-mechanical loadings at high operating temperatures that will limit their lifetimes, even in the absence of radiation damage. In this environment, severe mechanical damage can occur by the interaction of creep deformation with cyclic loading, known as fatigue. For example, high-temperature strain controlled fatigue typically causes significant strength decreases in RAFM steels and can lead to macroscopic component-scale dimensional instabilities, such as ratcheting (i.e. progressive deformations).

The effects of cyclic plastic loading are generally far more severe than under pure monotonic creep, especially in regimes with very damaging long tensile hold times and out of phase thermal and mechanical fatigue. The development of creep cracks, especially on grain boundaries, could lead to very short component lifetimes.

Creep-fatigue interaction is a complex process that depends on a large number of mechanical and metallurgical variables, such as test temperature, strain-rate,

hold-time, environment, and the microstructure of the material, and has been recently investigated for Eurofer97 [24][25].

Current high-temperature design and regulatory codes are very approximate at best, and typically based more on experience than mechanistic insight. For many applications, these codes are adequate because they are very conservative. However, it is not at all clear that such conservatism extends to very complex and intricate fusion structures that experience time-dependent dimensional changes, gradients, plastic strains, and short and longtime stress re-distributions.

Thus, fusion materials community is putting a great deal of effort to replace simple structural design rules with sophisticated multi-physics computational design tools in order to make fusion become a viable power production technology.

These considerations are further amplified by the potential for synergistic interactions between the effects of irradiation, thermal, chemical, and mechanical environments.

Last but not least, corrosion and compatibility are also key issues. Since one of the *driver* blanket concepts under consideration for the European DEMO relies on liquid lithium-lead eutectic (e.g. Pb-17Li) for breeding tritium and partially cooling the RAFM steel structure, it is essential to know the corrosion characteristics of those components in Pb-Li because deposition of activated corrosion products could have serious implications for plant operations and safety. Several studies have been and are being conducted on RAFM corrosion in liquid metal environments [27][28], taking into account many interacting variables that affect the corrosion process, including temperature, chemical composition of the structural material and the coolant, coolant flow velocity and velocity profile, coolant impurity concentration, radiation and also Magneto-Hydro Dynamics (MHD) effects.

Chapter 2

Optimization in Engineering Multiphysics Problems

2.1 Introduction

In modern engineering activities, the design procedure for a component encompasses several aspects, from the choice of the materials to the manufacturing processes, and each of them represents a cost voice in the final design. In order to reduce the total cost without undermining the performance, modern engineering activities consider the adoption of optimization methods along with the design definition process.

In case of fusion energy components, their cost and performance will play a significant role in the success of the future fusion power plants. Moreover, the design of those systems is featured by the need to handle contextually several physics aspects such as neutronics, thermal-hydraulics, thermo-mechanics and electro-magnetics, each one characterized by specific requirements. According to that, an engineering approach based on complex systems (i.e. systems engineering) that relies on the use of modern optimization methods has begun to be adopted [29][30]. Indeed, the overall view of the design parameters and their requirements can lead to the selection of an optimized design from the materials selection to the manufacturing, taking into account costs, reliability and benefits.

2.2 Multiphysics Design Approach

Complex energy systems, especially nuclear ones, usually need a multiphysics approach to be designed. The coupled effects of neutronics, thermal-hydraulics and mechanics (including the presence of eventual electro-magnetic loads) need to be evaluated together.

Each physics is described by its own set of governing equations (usually partial

differential equations) to be solved in a specific spatial domain with proper boundary conditions. Modern numerical tools relying on either deterministic or stochastic approaches have been developed during the second-half of last century, that are able to solve the numerical problems even in domains with complex geometry, loads and boundary conditions.

Among the deterministic methods, the most widely diffused are (1) the finite difference method, (2) the finite volume method and (3) the finite element method (FEM) [31]. While the first method is generally used to solve any kind of engineering problems involving differential equations in relatively simple domains, the second one got relevance for its use in Computational Fluid Dynamics (CFD) simulations, i.e. solving Navier-Stokes equations-based problems. The FEM method is, conversely, the most used method for multiphysics problem, that may involve heat transfer, structural mechanics, electro-magnetics, etc.

As to the stochastic methods, one of the most famous is definitely the Monte Carlo method [32], which relies on repeated random sampling to obtain numerical results. This method is nowadays applied for several problems, among which engineering ones such as optimization, integration and, especially, neutron-photon transport simulations.

Descriptions of the above-mentioned deterministic and stochastic numerical methods are not here provided for the sake of brevity, but interested readers are addressed to the following references [33][34][35] for Monte Carlo-based neutron transport simulations, computational fluid dynamics simulations by finite volume method and various FEM applications, respectively.

The importance of the application of a multiphysics approach for a complex engineering component will be briefly discussed in the following, taking into account the design of a breeding blanket for future fusion reactors as an example [36][37].

Fusion breeding blankets are subjected to heavy radiation and particles fluxes coming from the plasma wherein fusion reactions occur. Ions, neutrons and photons deposit their energy into the blanket in terms of both surface and volumetric heat loads. In particular, the power released by α-particles escaping from the plasma domain and hitting the plasma-facing surfaces can be simulated as a surface heat flux [W/m^2] onto the FW, whereas the power deposited inside the blanket by neutrons and photons is basically responsible for the volumetric heat generation (nuclear heating) [W/m^3] in structure, coolant, breeder, etc.

While the non-uniform surface heat flux values acting onto different regions of the blanket are computed by means of specific plasma MHD calculations [38], the nuclear heating profiles in the blanket materials are usually calculated by specific neutron-photon transport calculations [39]. This kind of simulation can also be used to compute the TBR and the damage induced by neutron irradiation (dpa), as well as the helium and hydrogen production [40].

The overall non-uniform heat power deposited needs to be removed by a proper cooling system in order to (1) use that power to generate electricity and (2) keep the temperature in structure and other materials below their specific limit value. Once designed, the efficiency of the cooling system (usually composed of tubes, cooling channels and/or cooling plates) can be properly assessed by means of fluid flow (CFD or simplified equivalent approaches) and heat transfer analyses. By these analyses, it is possible to determine mass flow rates, fluid velocity and pressure profiles and the temperature distributions in coolant, breeder and structure [41][42].

Both temperature, pressure and eventually neutron irradiation-induced damage distributions can be finally used for the structural analyses of the blanket, where the displacements, strain and stress fields arising within the structure are computed by means of FEM thermo-mechanical simulations [9].

All the results obtained adopting such a kind of multiphysics approach are used to assess and finalize the design of a fusion breeding blanket. In particular, several requirements for different aspects need to be fulfilled.

From the nuclear point of view, a minimum value of TBR > 1.0 is required together with a maximum neutron irradiation-induced damage which must be lower than a material-specific limit value [43].

As to the thermal-hydraulics, requirements on maximum temperature in the structure, maximum thermal rise, pressure drop, velocity of the coolant (and liquid breeder, if any) as well as a minimum margin against Critical Heat Flux (CHF) are foreseen [13].

Last but not least, a structural integrity assessment according to the applied nuclear Codes&Standards is mandatory, relying on the evaluation of specific maximum stress and strain values throughout the structural domain that must be lower than prescribed allowable limits [44].

2.3 Optimization Methods in Engineering Design

As stated above, complex multiphysics engineering problems require a system approach able to consider simultaneously all the variables, constraints and performances of the system.

Optimization methods in engineering make use of such a kind of approach, allowing the designers to improve performances and reduce costs, while complying with a set of either physical or functional constraints.

The basic principles of an optimization problem rely on the definition of an objective function $f(\mathbf{X})$ to be minimized (or maximized), where $\mathbf{X} = \{x_1, x_2, ..., x_n\}$ is the so-called *design vector*, containing the n design variables.

Hence, an optimization problem can be stated as follow [45]

$$\text{find} \quad \mathbf{X} = \{x_1, x_2, ..., x_n\} \qquad \text{which minimize (or maximize)} \quad f(\mathbf{X})$$

subject to the constraints

$$g_j(\mathbf{X}) \leq 0 \qquad j = 1, 2, ..., m$$

$$h_k(\mathbf{X}) = 0 \qquad h = 1, 2, ..., p$$

$$x_i^{(l)} \leq x_i \leq x_i^{(u)}$$

where $g(\mathbf{X})$ and $h(\mathbf{X})$ are functions called *functional constraints*, while $x_i^{(l)}$ and $x_i^{(u)}$ are the lower and upper limits of the i^{th} design variable, respectively. Lower and upper limits of each variable are also called *side constraints*.

Just for the sake of clarity, it must be stressed that in optimization, the choice of *minimizing* or *maximizing* a function (i.e. finding the optimum point) does not imply the use of different statement or techniques. Indeed, to minimize the function $f(\mathbf{X})$ is equivalent to maximize the opposite function $-f(\mathbf{X})$, as shown in Figure 2.1.

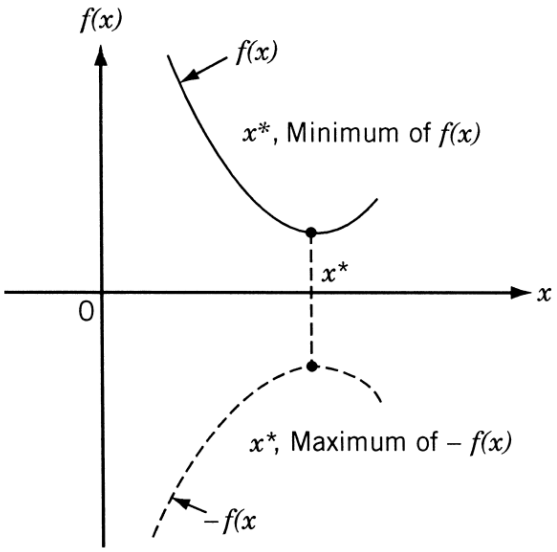

Figure 2.1: Minimization of $f(\mathbf{X})$ is the same as maximization of $-f(\mathbf{X})$ [45].

If there are no constraints, either *inequality* or *equality* ones, the problem is called *unconstrained optimization problem*, otherwise it will be *constrained*. The number of variables n and the number of constraints m and/or p are not necessary related in any way. In case of an optimization problem involving multiple objective functions, the problem is called *multiobjective* problem, where the overall objective function

can be stated as linear combination of the multiple objective functions

$$f(\mathbf{X}) = \sum_i \alpha_i f_i(\mathbf{X})$$

Various techniques are available for the solution of different types of optimization problems.

The classical optimization methods use differential calculus to find the unconstrained maxima and minima of a function of several variables. These methods assume that the function is differentiable twice with respect to the design variables and the derivatives are continuous [45]. For problems with equality constraints, the *Lagrange multiplier method* can be used. If the problem has inequality constraints, the *Kuhn–Tucker conditions* can be used to identify the optimum point. Nevertheless, these methods lead to a set of nonlinear simultaneous equations that may be difficult to solve.

Conversely, techniques of linear and nonlinear programming can be used for the solution of several kind of problems with easier and faster approaches. Most of these methods are numerical techniques wherein an approximate solution is sought by proceeding in an iterative manner by starting from an initial solution.

Linear programming techniques are optimization methods applicable for the solution of problems in which the objective function and the constraints appear as linear functions of the decision variables [46]. The constraint equations in a linear programming problem may be in the form of equalities or inequalities. Although its application has been widely used in several engineering problems, the complexity of modern technological challenges make nowadays this method very tough to be applied.

Unlike linear programming, nonlinear programming is the most general method of optimization that can be used to solve any optimization problem [47]. It deals with problems where objective functions and/or constraints are nonlinear and either very complicated to handle with or impossible to state as explicit functions of the design variables [45]. Basically, two kinds of problem may be encountered, as reported in Table 2.1.

Unconstrained Problem	**Constrained Problem**
Derivative-based methods	Direct methods
Derivative-free methods	Indirect methods

Table 2.1: Nonlinear programming techniques [45].

Where no constraints are present, the nonlinear techniques are classified into two main categories: derivative-based and derivative-free methods, also named as *descent* and *direct search* methods, respectively. While the former can be used only when it is possible to compute the gradient of the objective function, the latter require

only the objective function values but not the partial derivatives of the function. Famous descent methods are the *Steepest (or Cauchy) method*, the *Fletcher–Reeves method* and the *Newton's method*, whereas among the most relevant direct search ones can be listed the *Random Search method* (i.e. Monte-Carlo based methods), the *Powell's method* and the *Neldear-Mead (or Simplex) method* [45].

For constrained optimization problems, the programming techniques have been mainly developed starting from the bases built in the unconstrained problems and subdivided in *direct* and *indirect* methods.

The former are featured by the fact that constraints are handled in an explicit manner, whereas in the latter the constrained problem is solved as a sequence of unconstrained minimization problems [45]. The most popular direct methods are the *Random Search method* (again) and the *Complex method*, while probably the *Augmented Lagrange Multiplier method* can be assumed as the reference among the indirect methods.

There are also other optimization methods that have not been outlined here in this thesis such as *geometric*, *dynamic* and *integer* methods [45], solving the particular class of problems indicated by the name of the technique.

Finally, new, modern methods of optimization, including genetic algorithms, fuzzy optimization, and neural network-based optimization need also to be listed as very promising for the future of engineering optimization.

2.4 Derivative-free Methods for Constrained Optimization Problems

Recently, derivative-free algorithms have undergone a wide spread in engineering optimization. Finding optimum solutions in modern, complex engineering systems may require dealing with performances (or cost) based objective functions and constraints whose information about their derivatives is unavailable, unreliable or impractical to obtain. An example can be well represented by a structure wherein you want to minimize the peak stress by changing the dimensions. As the dimensions change, the location of the peak stress can shift from one point to another, being the objective function non-analytical and requiring inevitably a derivative-free approach.

On the other hand, as the number of design variables increases, derivative-free methods lose efficiency in terms of required computational time with respect to gradient-based algorithms, that are able to handle hundreds, or even thousands, of design variables with very low increase in computational cost.

Modern, complex engineering problems such as fusion energy devices require a multiphysics approach, usually described by non-linear governing equations and subjected to multiple constraints. Optimizing them require objective functions that might be non-smooth, or time-consuming to evaluate, or in some way noisy, so

that methods that rely on derivatives or approximate them via finite differences are unconvenient.

According to that, the most suitable optimization algorithms might be the ones based on gradient-free approach and able to deal with multiple constraints, either physical and functional. In the following subsection, a derivative-free optimization method for constrained problems named *Complex method* will be described. Owing to both its flexibility and ease coding, this method is the one used in Chapter 3 to optimize the design of the First Wall of a water-cooled breeding blanket concept, improving the layout of the internal cooling channels.

2.4.1 The Complex Method

The Complex method is an extended version of the derivative-free Nelder-Mead method (also called as *Simplex method*) [48], that can be used for constrained minimization/maximization problems. It relies on the use of a geometric entity called *complex*, formed by a set of $k \geq n+1$ points in an n-dimensional space where n is the number of design variables. According to the studies carried out by Box [49], the best performance is obtained setting $k = 2n$. Figure 2.2 reports an example of a complex in a 2-dimensional space composed of four points, each one identified by a combination of values of the two design variables (x_1, x_2). The leading idea

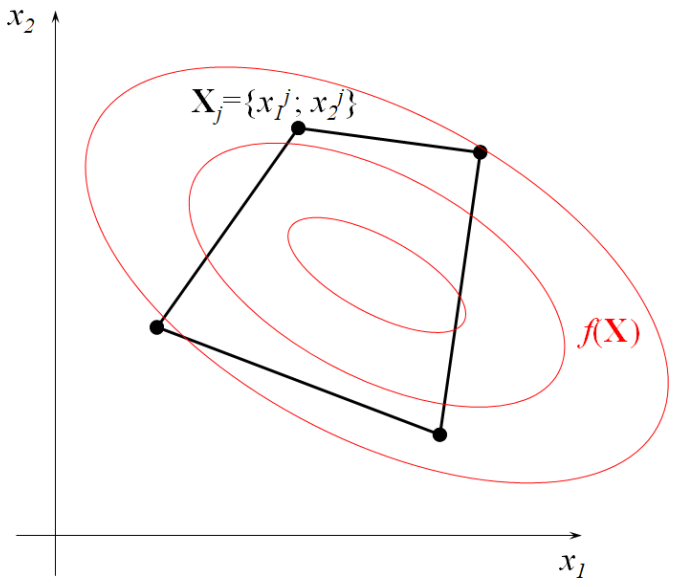

Figure 2.2: Complex in a 2-dimensional space.

in the Complex method is to compare the values of the objective function at the k vertices of a general complex and move it gradually towards the optimum point (i.e. a minimum of the objective function) during an iterative process. The movement of the complex is achieved by using an operation known as *reflection*. The iterative

procedure to be pursued in order to reach the minimum of the objective function can be summarized by the following steps:

1. Find $k \geq n+1$ points, each satisfying all m constraints. Practically, it starts with only one feasible point $\mathbf{X}_1$ (it must feasible), and the remaining $k-1$ points are found one at a time by the use of random numbers generated in the range 0 to 1, as

$$x_i^j = x_i^{(l)} + r(x_i^{(u)} - x_i^{(l)}) \qquad i = 1, 2, ..., n \qquad j = 2, 3, ..., k \tag{2.1}$$

   where x_i^j is the ith component of the point $\mathbf{X}_j$ and r is a random number lying in the interval (0,1). If $\mathbf{X}_j$ violates any of the constraints, the trial point $\mathbf{X}_j$ is moved halfway toward the centroid of the remaining, already accepted points (where the given initial point $\mathbf{X}_1$ is included). The centroid $\mathbf{X}_0$ of the already accepted points is given by

$$\mathbf{X}_0 = \frac{1}{j-1} \sum_{l=1}^{j-1} \mathbf{X}_l \tag{2.2}$$

   If the trial point $\mathbf{X}_j$ so found still violates some of the constraints, the process of moving halfway in toward the centroid $\mathbf{X}_0$ is continued until a feasible point $\mathbf{X}_j$ is found. By proceeding in this way, we will ultimately be able to find the required feasible points $\mathbf{X}_2$, $\mathbf{X}_2$,..., $\mathbf{X}_k$.

2. Once the initial complex is built up, the objective function is evaluated at each of the k points (i.e. vertices of the complex). If the vertex $\mathbf{X}_h$ corresponds to the highest function value, the process of *reflection* is used to find a new point $\mathbf{X}_r$ as

$$\mathbf{X}_r = (1+\alpha)\mathbf{X}_0 - \alpha \mathbf{X}_h \tag{2.3}$$

   where $\alpha \geq 1$ (Box suggested $\alpha = 1.3$ [49]) and $\mathbf{X}_0$ is the centroid of all vertices except $\mathbf{X}_h$

$$\mathbf{X}_0 = \frac{1}{k-1} \sum_{\substack{l=1 \\ l \neq h}}^{k} \mathbf{X}_l \tag{2.4}$$

3. Since the problem is a constrained one, the point $\mathbf{X}_r$ has to be tested for feasibility. If the point $\mathbf{X}_r$ is feasible and $f(\mathbf{X}_r) < f(\mathbf{X}_h)$, the point $\mathbf{X}_h$ is replaced by $\mathbf{X}_r$, and we go to step 2.

   If $f(\mathbf{X}_r) \geq f(\mathbf{X}_h)$, the first version of the algorithm foresaw the new trial point $\mathbf{X}_r^{(new)}$ to be obtained moving the old one halfway towards the centroid of all the vertices except $\mathbf{X}_h$, by the following relation

$$\mathbf{X}_r^{(new)} = \frac{1}{2}(\mathbf{X}_0 + \mathbf{X}_r) \tag{2.5}$$

and tested for the satisfaction of the relation $f(\mathbf{X}_r) < f(\mathbf{X}_h)$. If $f(\mathbf{X}_r) \geq f(\mathbf{X}_h)$, the procedure of finding a new point $\mathbf{X}_r$ moving it halfway towards the centroid $\mathbf{X}_r$ is repeated again.

Modified versions of the algorithm were then developed following the improvements suggested by Guin [50], who investigated the situations when the centroid of the complex is located either at a local minimum or inside an unfeasible region, and by Krus [51], who modified the algorithm avoiding the new reflected point and the minimum (maximum) point to get very close to each other and make the complex to collapse. A successful version of the method was also implemented by Andersson [52], where the use of a random value to be added to the new reflected point allowed to solve the above-mentioned issues. Moreover, although randomness requires some extra effort in searching for a better point in the neighborhood of the minimum (maximum) value, it also helps to reduce the probability to get the complex stuck in a local minimum rather than the global minimum of the objective function. According to [52], in case of minimization problem Equation (2.5) is replaced by

$$\mathbf{X}_r^{(new)} = \frac{\left[\mathbf{X}_r^{(old)} + \epsilon\mathbf{X}_0 + (1-\epsilon)\mathbf{X}_l\right]}{2} + (\mathbf{X}_0 - \mathbf{X}_l)(1-\epsilon)(2r-1) \tag{2.6}$$

with

$$\epsilon = \left(\frac{n_r}{n_r + k_r - 1}\right)^{\frac{n_r+k_r-1}{n_r}}$$

where $\mathbf{X}_l$ is the point with the lowest objective function value, k_r is the number of times the reflected point has repeated itself as the one with higher objective function value with respect to the worst point $\mathbf{X}_h$, n_r is a constant (Andersson suggested $n_r = 4$ [52]), and r is a random number in the range 0 to 1. This procedure is repeated until a new point that satisfies the relation $f(\mathbf{X}_r) < f(\mathbf{X}_h)$ is found.

If an improved point $\mathbf{X}_r$, with $f(\mathbf{X}_r) < f(\mathbf{X}_h)$, cannot be obtained after a prescribed number of steps (when k_r=8, ϵ is already lower than 0.1), the point $\mathbf{X}_r$ is discarded and the entire procedure of reflection is restarted by using the point $\mathbf{X}_p$, which has the second-highest function value instead of $\mathbf{X}_h$. The procedure is usually stopped when not even picking the point with the third-highest function value leads to an improved reflected point.

4. If at any stage any, the reflected point $\mathbf{X}_r$ (found in Step 3) violates any of the variable limits or constraints, the following procedure is applied:

   (a) if any *side* constraint is not fulfilled, the i^{th} component of $\mathbf{X}_r$ is replaced

according to

$$\begin{cases} x_i^r = x_i^{(l)} & \text{if } x_i^r < x_i^{(l)} \\ x_i^r = x_i^{(u)} & \text{if } x_i^r > x_i^{(u)} \end{cases}$$

(b) if any *functional* constraint is not fulfilled, Equation (2.6) is applied as in Step 3 until the point becomes feasible.

5. Each time the worst point $\mathbf{X}_h$ of the current complex is replaced by a new point, the complex gets modified and we have to test for the convergence of the process. In particular, the convergence is obtained when the standard deviation of the function value among the complex points becomes sufficiently small, that is

$$\left(\frac{1}{k} \sum_{j=1}^{k} [f(\mathbf{X}_0) - f(\mathbf{X}_j)]^2 \right)^{1/2} < \varepsilon \tag{2.7}$$

where $\mathbf{X}_0$ is the centroid of all the k vertices of the current complex, and ε is a specified small number greater than 0. Considering the scope of the method, here the standard deviation can represent contextually two main features: (1) the distance among the points of the complex (i.e. points with similar objective function value are probable to be close in variables space) and (2) the ratio of the variation of the objective function value among the points to the related error.

The method just described will move and modify the complex toward the minimum (maximum) of the function until all the points of the complex are featured by very similar values of the objective function, i.e. the complex is going to collapse into its centroid in proximity of the optimum point (see Figure 2.3).

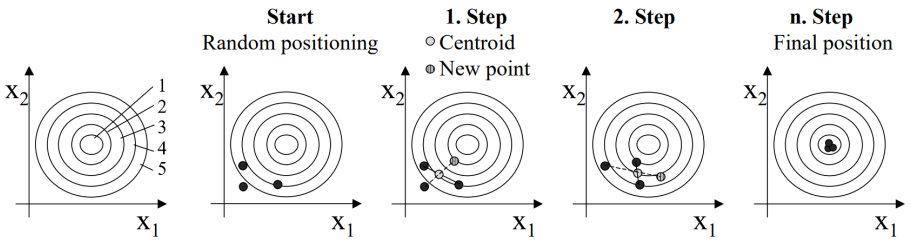

Figure 2.3: Progress of the Complex method for a 2-dimensional example of minimization problem [52].

As described above, the main operation of the Complex method is represented by the *reflection*. In fact, as shown in Figure 2.3 for a minimization problem, reflecting the point with the highest objective function with respect to the centroid of the remaining two points gives a new point whose function value is lower than both the reflected point and the other points of the complex. Of course, not all the reflections give improved (and feasible) points at first trial, and several steps are needed to warp

and move the complex until it becomes small enough to have all the points in very proximity of the minimum of the function.

The Complex method has been applied to a wide range of problem areas such as fluid power system design [52], physics [53], structural engineering [54], etc. Although it was originally developed for problems with continuous variables, Haque [54] has shown that the Complex method could also be applied to mixed continuous and discrete variable problems.

2.5 Implementation of the Complex Method in MATLAB and Code Validation

The Complex method described in the previous section has been used in this work to optimize the European water-cooled breeding blanket concept for DEMO reactor. Before applying it to the blanket, a preliminary coding of the algorithm has been carried out into MATLAB [55], and applied to a very simple exercise drawn from [45] in order to validate it. The MATLAB code is reported in Appendix A and the example used for the validation is here below described.

The problem consists in the design of a uniform column of tubular section, with hinge joints at both ends, (see Figure 2.4) to be optimized for minimum cost.

The column has to carry a compressive load $P = 2500$ kgf, and it is made up of a material that has a yield stress $\sigma_y = 500$ kgf/cm^2, elastic modulus $E = 0.85 \cdot 10^6$ kgf/cm^2, and density $\rho = 0.0025$ kgf/cm^3. The length of the column is $l = 250$ cm.

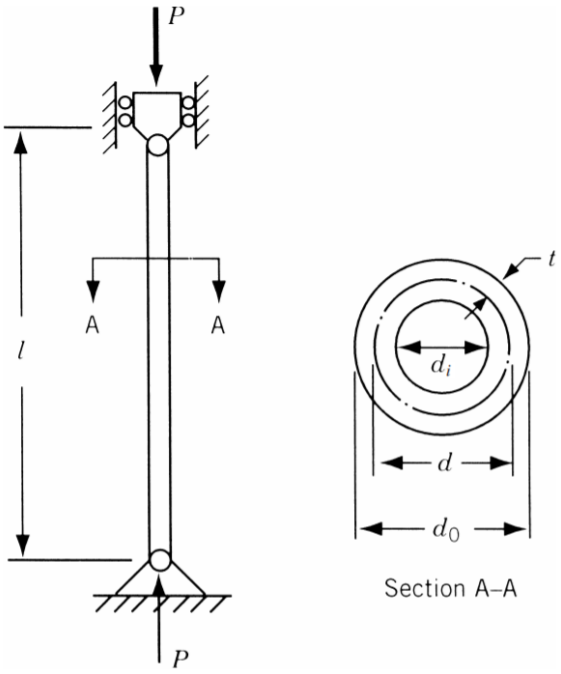

Figure 2.4: Tubular column under compression to be optimized [45].

The stress σ induced in the column must be less than the buckling stress σ_b as well as the yield stress. As to the variables limits, the mean diameter of the column is restricted to lie between 2 and 14 cm while thicknesses outside the range 0.2 to 0.8 cm are not available in the market. The cost of the column includes material and construction costs and can be taken as $5W + 2d$, where W is the weight in kilograms force and d is the mean diameter of the column in centimeters. The design variables are, thus, the mean diameter d and the tube thickness t:

$$\mathbf{X} = \{x_1, x_2\} = \{d, t\}$$

The objective function to be minimized, expressed in terms of the design variables, is given by

$$f(\mathbf{X}) = 5W + 2d = 5\rho l\pi dt + 2d = 9.82x_1x_2 + 2x_1 \tag{2.8}$$

The functional constraints can be expressed as

$$\sigma \leq \sigma_y \tag{2.9}$$

$$\sigma \leq \sigma_b \tag{2.10}$$

where the induced stress and the buckling stress are respectively given by

$$\sigma = \frac{P}{\pi dt} = \frac{P}{\pi x_1 x_2}$$

$$\sigma_b = \frac{\pi^2 EI}{l^2}\frac{1}{\pi dt} = \frac{\pi^2 E(x_1^2 + x_2^2)}{8l^2}$$

with I equal to the moment of inertia of cross section expressed by

$$I = \frac{\pi}{64}(d_o^4 - d_i^4) = \frac{\pi}{8}x_1x_2(x_1^2 + x_2^2)$$

Conversely, the side constraints are given by

$$2 \leq d \leq 14 \tag{2.11}$$

$$0.2 \leq t \leq 0.8 \tag{2.12}$$

In view of what stated in Section 2.3, the whole set of inequality constraints can be expressed in standard form as

$$g_1(\mathbf{X}) = \frac{2500}{\pi x_1 x_2} - 500 \leq 0 \tag{2.13}$$

$$g_2(\mathbf{X}) = \frac{2500}{\pi x_1 x_2} - \frac{\pi^2(0.85 \cdot 10^6)(x_1^2 + x_2^2)}{8(250)^2} \leq 0 \tag{2.14}$$

$$g_3(\mathbf{X}) = -x_1 + 2.0 \leq 0 \tag{2.15}$$

$$g_4(\mathbf{X}) = x_1 - 14.0 \leq 0 \tag{2.16}$$

$$g_5(\mathbf{X}) = -x_2 + 0.2 \leq 0 \tag{2.17}$$

$$g_6(\mathbf{X}) = x_2 - 0.8 \leq 0 \tag{2.18}$$

where Equations (2.13) and (2.14) refer respectively to the functional constraints Equations (2.9) and (2.10), whereas Equations (2.15) to (2.18) represent the side constraints expressed in Equations (2.11) and (2.12).

Since there are only two design variables, the problem can be solved graphically as shown here below in Figure 2.5.

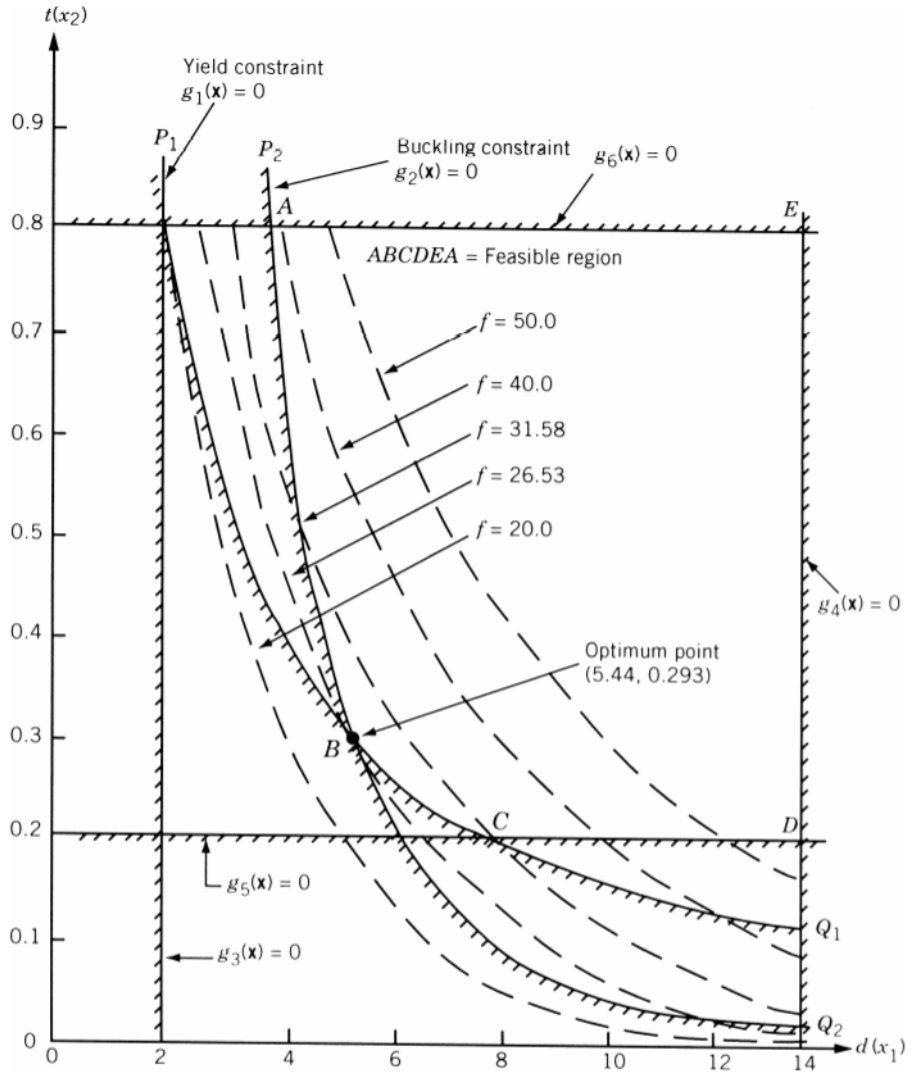

Figure 2.5: Solution of the optimization problem of a tubular column under compression from [45].

The feasible region is enclosed by the six inequality constraints (ABCDE). Reporting the contour plot of the objective function in the same plot allowed authors in [45] to easily find the optimum point B, characterized by an objective function

value of 26.53. The optimal design is, hence, featured by a mean diameter of 5.44 cm with a thickness of 0.293 cm.

The same exercise has been solved by using the Complex method, in the form as implemented in Appendix A. Since the method relies on random numbers to build up the initial complex, multiple runs have been carried out in order to assess the strength of the code, in terms of getting the minimum of the objective function with a reasonable number of steps. As reported below, five runs have been enough to validate the method as implemented in MATLAB. Since the method works only if the first point of the complex is feasible, the point $\mathbf{X}_1 = \{d_1, t_1\} = \{8, 0.5\}$ has been selected looking at the feasible region in Figure 2.5. The results of the optimization simulations are reported in Table 2.2.

For each run carried out, the following items are reported in the table:

- the array $\mathbf{X}_{start}$ corresponding to the initial complex, wherein each row corresponds to a point of the complex, identified by a combination of values of the selected design variables (d,t). The first row contains always the first feasible point ($d = 8$ cm, $t = 0.50$ cm). As stated above, the number of points (rows) of the complex is equal to two times the number of design variables.

- the vector $f(\mathbf{X}_{start})$, which contains the values of the objective function corresponding to each point of the complex $f(\mathbf{X}_{start})$.

- the array $\mathbf{X}_{end}$, that is the final complex obtained at the end of the optimization.

- the vector $f(\mathbf{X}_{end})$, which contains the values of the objective function corresponding to each point of the complex $f(\mathbf{X}_{end})$.

- the total number of reflections (Reflections) needed to reach the minimum of the objective function.

- the standard deviation σ, defined as in Equation (2.7), obtained at the end of the optimization. For this simulation, the minimum threshold ε has been set to $1{\cdot}10^{-4}$, as explained below.

- the percentage error (Error [%]) between the minimum value of the objective function calculated by using the Complex method (highlighted in bold) and the result obtained graphically in [45], that is $min[f(\mathbf{X})] = 26.53$.

As shown in the table, all the five optimization runs have given basically the same output, i.e. the combination of $d \simeq 5.45$ cm, $t \simeq 0.29$ cm with an objective function value of around 26.52, showing an error lower than 0.06% with respect the one reported in [45].

Run	$\mathbf{X}_{start}$	$f(\mathbf{X}_{start})$	$\mathbf{X}_{end}$	$f(\mathbf{X}_{end})$	Reflections	σ	Error [%]
#1	$\begin{pmatrix} 8.0000 & 0.5000 \\ 13.0691 & 0.4746 \\ 7.5872 & 0.4391 \\ 5.9850 & 0.5841 \end{pmatrix}$	$\begin{pmatrix} 55.2400 \\ 86.9878 \\ 47.8547 \\ 46.2663 \end{pmatrix}$	$\begin{pmatrix} 5.4512 & 0.2920 \\ \mathbf{5.4512} & \mathbf{0.2920} \\ 5.4512 & 0.2920 \\ 5.4512 & 0.2920 \end{pmatrix}$	$\begin{pmatrix} 26.5155 \\ \mathbf{26.5154} \\ 26.5155 \\ 26.5156 \end{pmatrix}$	65	$6.5263{\cdot}10^{-5}$	0.0549
#2	$\begin{pmatrix} 8.0000 & 0.5000 \\ 9.0271 & 0.4580 \\ 6.8442 & 0.3795 \\ 10.3508 & 0.2490 \end{pmatrix}$	$\begin{pmatrix} 55.2400 \\ 58.6139 \\ 39.1682 \\ 45.9853 \end{pmatrix}$	$\begin{pmatrix} 5.4510 & 0.2920 \\ 5.4510 & 0.2920 \\ \mathbf{5.4511} & \mathbf{0.2920} \\ 5.4511 & 0.2920 \end{pmatrix}$	$\begin{pmatrix} 26.5162 \\ 26.5161 \\ \mathbf{26.5160} \\ 26.5160 \end{pmatrix}$	43	$8.0449{\cdot}10^{-5}$	0.0527
#3	$\begin{pmatrix} 8.0000 & 0.5000 \\ 7.0135 & 0.4860 \\ 5.4160 & 0.4514 \\ 11.0024 & 0.5919 \end{pmatrix}$	$\begin{pmatrix} 55.2400 \\ 47.4678 \\ 34.8173 \\ 85.8882 \end{pmatrix}$	$\begin{pmatrix} 5.4505 & 0.2921 \\ \mathbf{5.4503} & \mathbf{0.2921} \\ 5.4503 & 0.2921 \\ 5.4503 & 0.2921 \end{pmatrix}$	$\begin{pmatrix} 26.5188 \\ \mathbf{26.5187} \\ 26.5188 \\ 26.5189 \end{pmatrix}$	45	$6.0636{\cdot}10^{-5}$	0.0426
#4	$\begin{pmatrix} 8.0000 & 0.5000 \\ 13.6937 & 0.6952 \\ 7.1585 & 0.3989 \\ 6.3803 & 0.4164 \end{pmatrix}$	$\begin{pmatrix} 55.2400 \\ 120.7823 \\ 42.3282 \\ 38.8223 \end{pmatrix}$	$\begin{pmatrix} \mathbf{5.4512} & \mathbf{0.2920} \\ 5.4511 & 0.2920 \\ 5.4511 & 0.2920 \\ 5.4512 & 0.2920 \end{pmatrix}$	$\begin{pmatrix} \mathbf{26.5155} \\ 26.5158 \\ 26.5157 \\ 26.5156 \end{pmatrix}$	40	$9.5439{\cdot}10^{-5}$	0.0545
#5	$\begin{pmatrix} 8.0000 & 0.5000 \\ 11.9310 & 0.3135 \\ 13.2192 & 0.5194 \\ 7.4880 & 0.5793 \end{pmatrix}$	$\begin{pmatrix} 55.2400 \\ 60.5538 \\ 93.7905 \\ 57.5283 \end{pmatrix}$	$\begin{pmatrix} \mathbf{5.4510} & \mathbf{0.2920} \\ 5.4512 & 0.2920 \\ 5.4515 & 0.2920 \\ 5.4511 & 0.2920 \end{pmatrix}$	$\begin{pmatrix} \mathbf{26.5162} \\ 26.5163 \\ 26.5162 \\ 26.5164 \end{pmatrix}$	60	$6.6480{\cdot}10^{-5}$	0.0519

Table 2.2: Results obtained using the Complex method as implemented in Appendix A to solve the optimization problem of a tubular column drawn from [45]. The optimum point obtained is highlighted in bold.

The movement and shaping of the complex to reach the minimum of the objective function (while complying with constraints) can be visualized by the following plots.

Figure 2.6 shows in a log-log graph the objective function value at the centroid of the complex $f(\mathbf{X}_0)$ vs. the number of reflections completed. In agreement with the previous one, Figure 2.7 shows in a log-log graph the standard deviation value of the complex σ (as defined in Equation (2.7)) vs. the number of reflections completed.

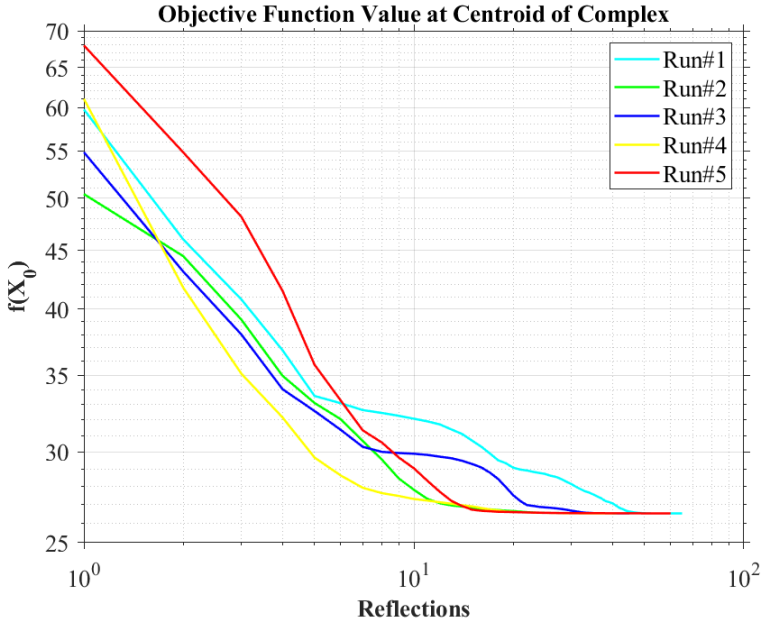

Figure 2.6: Objective function value at centroid vs. number of reflections, obtained solving the exercise in [45] using the Complex method.

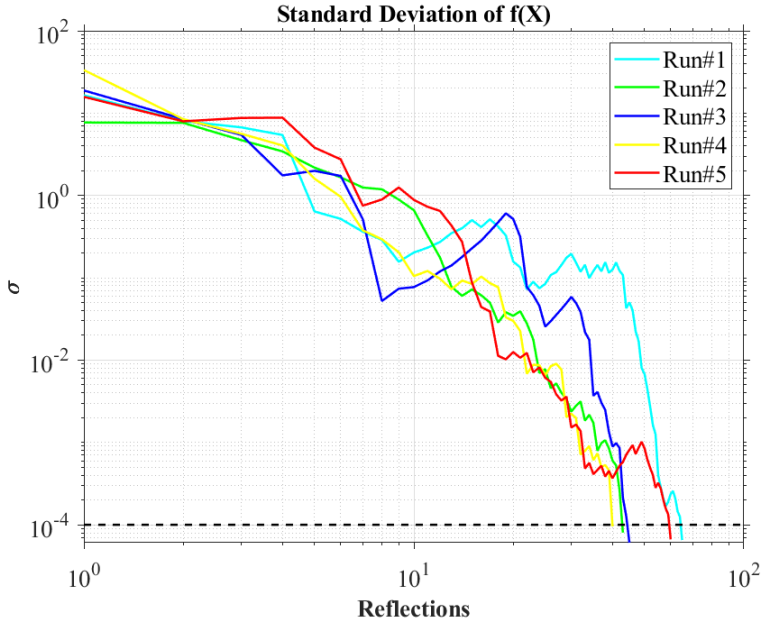

Figure 2.7: Standard deviation of $f(\mathbf{X})$ vs. number of reflections, obtained solving the exercise in [45] using the Complex method.

As easily observable, even though each run starts from a different starting "point" due to random numbers used to generate the initial complex, all of them reach the optimum point after around 40÷65 reflections. Moreover, while increasing the number of reflections, the standard deviation of the complex is reducing.

Once the minimum threshold ε is reached, the optimization run is stopped. As to the latter, aiming to have a deviation between the objective function value at each point and the value at the centroid lower than $1{\cdot}10^{-3}$ on average, ε has been set to $1{\cdot}10^{-4}$ for this problem.

Chapter 3

Design Optimization of Water-Cooled Breeding Blanket Concepts

3.1 Introduction

The design of a rational, functional breeding blanket able to guarantee the tritium self-sufficiency of the plant is an unescapable requirement for any next-step nuclear fusion facility beyond ITER [3]. Just as an example, the European DEMO reactor with a fusion power of about 2 GW will consume around 111 kg of tritium per full power year (fpy), and this clearly underlines the indispensable requirement for the breeding blanket to produce and enable extraction of the tritium bred to achieve fuel self-sufficiency.

Worldwide, breeding blanket concepts are substantially being designed as helium-cooled or water-cooled. While using helium as a coolant may be considered as a more innovative and promising option than water, on the other hand, the latter can rely on a widely developed and adopted technology behind. Indeed, the great majority of both conventional and nuclear power plants relies on water-based thermodynamic cycles to generate electricity. Nevertheless, the adoption of water as a coolant for the breeding blankets shows some relevant drawbacks, having a strong impact on the tritium breeding performance as well as on the strength against irradiation embrittlement of the material.

Many of these aspects will be discussed in this chapter, taking as reference example a novel, alternative design option for the WCLL BB concept of the European DEMO reactor. With the aim of presenting a rational methodology to design a water-cooled breeding blanket taking into account as many aspects as possible, a specific optimization-based procedure that relies on the above-presented Complex method is developed and presented in this chapter. In particular, the

attention has been focused on optimizing the layout of the internal cooling channels in the First Wall, trying to increase the tritium breeding performances while complying with several thermal and structural requirements.

3.2 The European DEMO WCLL BB Concept: Alternative Design Option

As already stated in Chapter 1, the Water-Cooled Lithium Lead BB is one of the two breeding blanket concepts currently under investigation to become the *driver* blanket for the European DEMO reactor.

Instead of referring to the current *reference* version of the WCLL BB (whose detailed description can be found in [13][56][57]), the work presented here relies on the alternative design option for the WCLL BB conceived at the University of Palermo, also in collaboration with ENEA [14][58] (see Figure 3.1). While using the same design for most of the structure, the alternative concept foresees a different layout of DWTs inside the BZ, implying consequently slight modifications of the rear manifold parts.

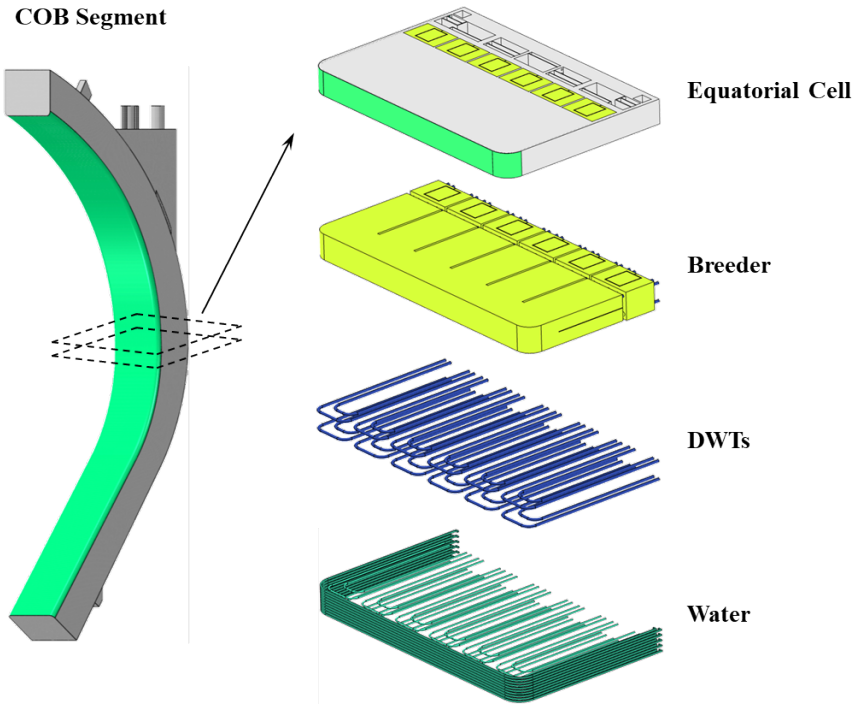

Figure 3.1: Alternative design option of the WCLL Central Outboard Blanket segment.

Regarding the architecture of the European DEMO Breeding Blanket, it is sub-divided in sixteen toroidal sectors, each one composed of five single module segments: two inboard segments and three outboard segments. Taking the Central Outboard Blanket (COB) segment as reference, it can be thought as composed

of a poloidal stack of *elementary cells*, each one identified by two consecutive toroidal-radial SPs, as shown in Figure 3.1.

Looking at Figure 3.2, the structure of the *equatorial* cell is based on a Segment Box (composed of the W-armour, the FW, the two SWs and the BP), two toroidal-radial SPs, five poloidal-radial SPs, a rear manifold region (for either water and PbLi) and the BSS.

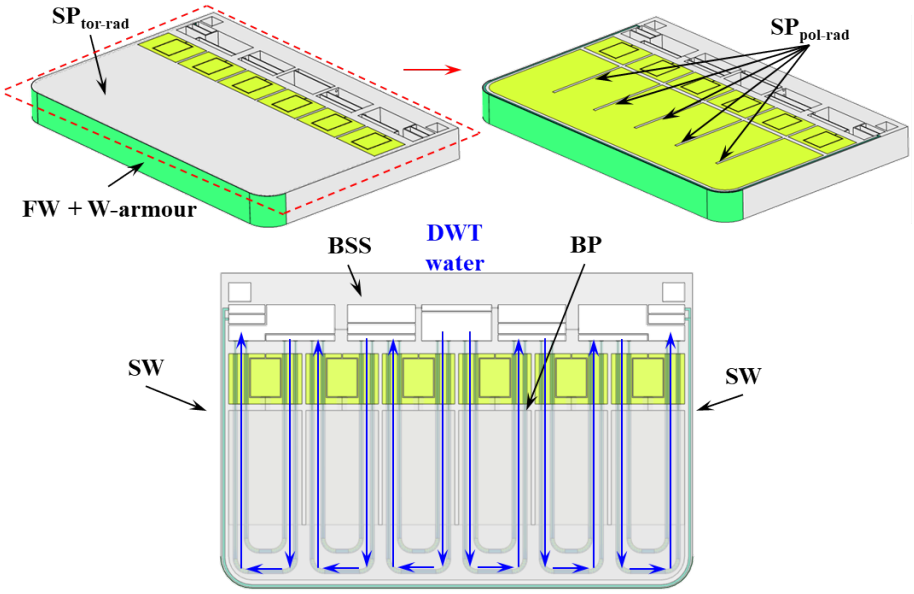

Figure 3.2: Internal view of the alternative design option of the WCLL COB segment. Particular on the DWT water flow path.

Figure 3.2 shows also the new layout of the DWTs inside the BZ, featuring this alternative design. With the aim of improving the cooling of the SP grid as well as increasing the amount of breeder inside the BZ, a former optimization campaign carried out at University of Palermo [58] came out with a proposed layout made of shorter 24 U-shaped DWTs placed poloidally closer to the toroidal-radial SPs. Thanks to such layout (which is also very similar to the recent ITER WCLL-TBM Set [59]), it is possible to reduce the maximum temperature reached in the Eurofer97 components as well as the area of the thermal hot-spots on them. Moreover, in order to have higher heat transfer coefficients, a triple-pass layout of the cooling water has been envisaged in the BZ, making the required mass flow rate to flow in an overall-reduced cross-sectional area so to increase the average velocity, still without undermining pressure drop requirements.

Such modification has, thus, required a revision of the manifold region. While the breeder manifold region was not affected by the change in DWTs layout, the water manifolds needed to be re-conceived, as shown in Figure 3.3. Although both reference and alternative manifold designs rely on the one recently proposed by ESTEYCO [60] and improved by the WCLL BB design team [16], the latter has been conceived making some modifications in the DWT-side of the water manifolds.

Figure 3.3: Alternative manifold design of the WCLL COB segment.

In order to have a toroidally-symmetric thermal field in the structure [13], the water inlet manifold is foreseen at the center (4), while the outlet is at both sides of the manifold region (5). The triple-pass of the coolant is obtained by means of proper collectors (6). Even if all the design modifications have been implemented trying to keep the cross-sectional areas as they were so to maintain the same average velocities, it must be pointed out that such a design is only conceptual, and the evaluation of the best cross-sectional areas, the check on its feasibility and its correct integration is yet to be performed.

As to the FW-SWs cooling system, Figure 3.4 shows the internal square cooling channels, where water counter-current flow occurs, whose poloidal pitch can vary along the development of the segment depending upon the heat load distribution.

In order to make the reader more comfortable with such design concept, the main geometrical features of the equatorial cell are reported in Table 3.1 [16].

As every breeding blanket concept, the final design has to be compliant with a set of specific requirements, that can be particularly demanding. Meeting those requirements and ensuring certain performances will do make the difference in the selection of one blanket design with respect to another. In the next three subsections, the main nuclear, thermal-hydraulic and structural requirements prescribed for the DEMO WCLL BB concept will be outlined.

3.2.1 Nuclear Requirements

The main requirement of a breeding blanket from the nuclear point of view is definitely the minimum net TBR ≥ 1.0. In case of a water-cooled blanket such as

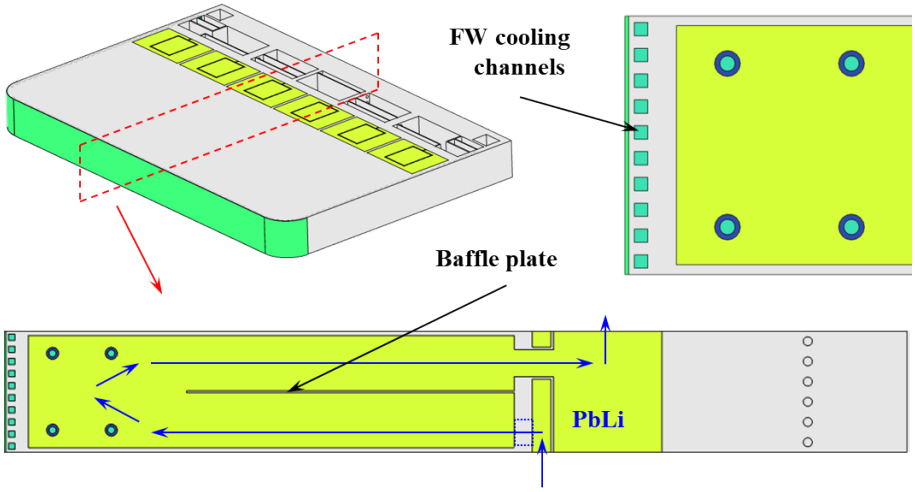

Figure 3.4: Detailed view of the FW cooling channels design. Particular on the PbLi flow path.

the DEMO WCLL BB, the tritium breeding performances can be strongly affected by the water amount used to cool down the structure, especially in the region close to plasma. This is mainly due to both its simultaneous moderation and absorption effects onto the neutrons coming from plasma.

As reported in [43], the evaluation of the tritium breeding performances in DEMO reactor is based on Monte Carlo techniques for neutron transport calculation. Of course, this approach is affected by lots of uncertainties that must be taken into account in order to exceed the minimum TBR by a *safety* margin.

The goal for the specification of a minimum design target value is to ensure a net TBR ≥ 1.0 for DEMO, independently from the considered blanket concept and effects which are not taken into account in the TBR calculation, such as uncertainties of the nuclear data, blanket openings, lithium burn-up and tritium losses in the fuel cycle.

The last updated design target value for DEMO [43] has been set starting from a minimum TBR requirement ($= 1.05$), evaluated by specific fuel cycle calculations, plus a design margin that encompasses all uncertainty sources involved in the TBR calculations and the incomplete computational model due to the absence of non-breeding systems in the full BB model, as used in the TBR calculations. Based on this rationale, the TBR design target value for the European DEMO has been set to 1.15, to be obtained by 3D Monte Carlo-based neutron transport calculations under proper modelling assumptions.

The second important nuclear-type requirement involves the shielding performances of the blanket [61]. In particular, the following shielding requirements must be fulfilled for a fusion power reactor: (1) the sufficient protection of the super-conducting toroidal field coils, (2) the irradiation induced damage accumulation in structural materials needs to be limited to prevent properties

Parameter	**Unit**	**Value**
Toroidal length of the cell	[m]	1.5
Radial depth of the cell	[m]	1.0
Poloidal height of the cell	[mm]	135
Radial depth of the BZ	[mm]	540
W-armour thickness	[mm]	2
FW thickness	[mm]	25
$SP_{tor-rad}$ thickness	[mm]	10
$SP_{pol-rad}$ thickness	[mm]	12
BP thickness	[mm]	20
BSS thickness	[mm]	100
Number of FW channels per cell	[-]	4÷10
FW channel dimensions	[mm]	7x7
Number of DWTs per cell	[-]	24
DWT inner-outer diameters	[mm]	8-13.5

Table 3.1: Main geometrical features of the alternative design of the WCLL BB concept [16].

degradation, (3) the re-weldability of components and connections/pipes made of steel must be ensured.

With regards to the former, the most crucial radiation loads to the toroidal field coils are the fast neutron fluence to the superconductors, the peak nuclear heating in the winding pack, the radiation damage to the copper insulator and the radiation dose absorbed by the Epoxy resin insulator. The related radiation design limits are the criteria for assessing the shielding efficiency which must also be met at the inboard mid-plane of the reactor where minimum space is available for shielding. Under DEMO conditions, the limit for the fast neutron flux is around 1×10^9 $cm^{-2}s^{-1}$, whereas the maximum allowable nuclear heating for the super-conducting toroidal field coil is extremely low (≈ 50 W/m^3).

Another crucial value for structural components (both in-vessel and ex-vessel) is the displacement damage accumulation, which together with the operating temperature, will determine the component lifetime and also has an impact on the choice of the material used. A target limit of 50 dpa is assumed for the DEMO First Wall made of Eurofer97 steel, which can be translated into a blanket lifetime of 5 fpy. Radiation induced degradation of the material strength is another issue for the austenitic stainless steel assumed for the vacuum vessel. A recent evaluation concluded that the dpa level, accumulated over the full DEMO plant lifetime, should be lower than 2.75 dpa to ensure that the fracture toughness is reduced by no more than 30%.

Last but not least, the assumption is that re-welding of stainless steel is should

be successful at He concentrations below 1 appm, value that must be checked by 3D neutronic calculations in correspondence of locations where re-welding of steel components will be required during the assumed DEMO lifetime.

3.2.2 Thermal-Hydraulic Requirements

From the thermal-hydraulic point of view, several aspects need to be considered during the conception of a breeding blanket. In particular, thermal-hydraulic requirements can be basically subdivided into two main categories: (1) the requirements concerning the component itself, and (2) the requirements regarding the integration with other systems.

Focusing the attention on the WCLL BB concept, the first category regards the main aspects related to both cooling water and liquid breeder flows inside the blanket.

The cooling water works under PWR conditions, i.e. 15.5 MPa as operating pressure and 295-328 °C as inlet-outlet temperatures. While flowing within the blanket, the main aim is to cool down the structural components extracting the heat power deposited inside coming from the plasma.

Inside both the FW-SWs cooling channels and the DWTs, the water velocity must stay within specific limits: an upper limit of 7 m/s is due to erosion effects [57], whereas the lower limit depends basically on Departure from Nucleate Boiling (DNB) issue, in which steam bubbles no longer break away from the solid surface of the channel, bubbles dominate the channel or surface, and the heat flux dramatically decreases. Vapor essentially insulates the bulk liquid from the hot surface. During DNB, the surface temperature must therefore increase substantially above the bulk fluid temperature in order to maintain a high heat flux. This phenomenon happens when the heat flux of a potential boiling systems reaches the Critical Heat Flux value. In particular, lower is the velocity, lower is the so-called *CHF ratio*, that is the ratio of the CHF (using for instance the TONG-75 correlation [62]) to the peak heat flux on the wetted surface. As to the latter, the presence of a minimum CHF ratio has to be verified during the design of a water-cooled FW.

In addition to that, the water cooling system must guarantee the temperature of the structure to stay within the prescribed range of the material. For Eurofer97, the operating window is suggested to be 350-550 °C, as will be described in the next paragraph, and thus the identification of the best layout of cooling channels and tubes is pivotal for breeding blanket operations.

Concerning the liquid breeder, the two main aspects to be considered are definitely the corrosion effect due to the chemical interactions between liquid metal and steel and, above-all, the huge pressure losses due to MHD effects. In order to ensure an overall pressure drop of the PbLi system reasonably lower than 2.0 MPa, the lithium-lead flow path in the blanket is designed to maintain throughout a relatively

low velocity (e.g. ≈ 13 mm/s in the manifolds and ≈ 0.01 mm/s in the BZ) [13].

As far as the integration with other DEMO systems is concerned, very important requirements need to be considered from the thermal-hydraulic point of view. Being the blanket the component in charge of extracting around the 80% of the fusion power released by the plasma, its thermal-hydraulic performances play a pivotal role in the Balance of Plant.

Furthermore, since DEMO is going to work with a *pulsed mode* (see Figure 3.5), the design of a water-based DEMO BOP is very demanding, because conventional water-based power conversion systems, such as steam turbines and steam generators, usually work under steady-state conditions. Accordingly, the breeding blanket as well will be designed to work under conditions (e.g. coolant inlet temperature, mass flow rates, etc.) potentially varying a lot through the different phases existing in each cycle, such as the *flat top* and the *dwell time*.

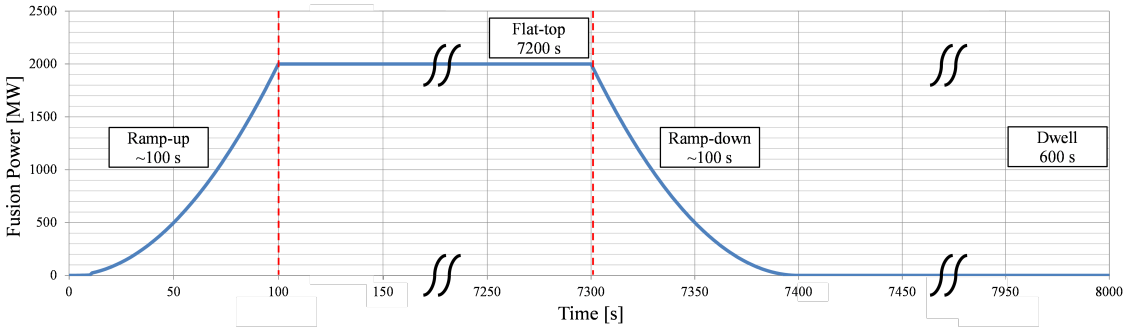

Figure 3.5: DEMO power cycle [12].

As to the PbLi side, the WCLL BB is also part of the so-called *PbLi loop*, that is the system in charge of making the PbLi circulation through the blanket at about 330 °C, carrying the tritium generated in the BB (about 270–280 g/day) towards the Tritium Extraction and Removal System, contributing in the tritium extraction, controlling PbLi chemistry and purifying the PbLi from impurities (e.g. activated corrosion products) [13].

3.2.3 Structural Requirements

Due to the extreme environment under which the DEMO BB will operate, the thermo-mechanics plays a pivotal role in its design. As common in RAFM steels, Eurofer97 is characterized by good high-temperature mechanical properties (e.g. strength, ductility, creep, toughness, etc.) as well as a sufficient resistance to fast-neutron irradiation damage. However, other issues have been recognized in the application of this structural material, such as the degradation of the mechanical properties beyond a temperature of about 550 °C, corrosion effects under lithium-lead environment and the irradiation embrittlement at low temperature.

The structure of the WCLL BB concept must be designed, hence, to work under an average temperature greater than 350 °C in the region close to the plasma, so to avoid unsustainable positive shifts of the DBTT, and, at the same time, with a maximum temperature below the upper limit of 550 °C due to properties degradation. On the other hand, such high temperatures might entail to deal with potential large creep deformations as well as relevant thermal stresses, which may involve dangerous failure modes such as plastic flow localization, exhaustion of ductility and ratcheting.

According to that, the design of the WCLL BB concept has to be developed considering all the different loading scenarios it might undergo and its structural integrity must be assessed by means of specific (nuclear) codes and standards. As far as DEMO blanket design is concerned, the EUROfusion project has selected the French nuclear standards RCC-MRx [63] as reference.

As in all the main nuclear standards (e.g. ASME BPVC, SDC-IC, RCC-M), the design criteria reported in the RCC-MRx consider essentially all the above-mentioned failure modes, classified in different service levels depending upon the loading scenarios. In particular, three service levels are defined:

- *Level A*, including the first (SF1) and the second (SF2) operating conditions, where both refer to conditions to which component may be subjected in the course of normal operation, including normal operating incidents (upset), start-up and shutdown.

- *Level C*, including the third operating conditions (SF3), that are emergency conditions, corresponding to very low probability of occurrence but which must nonetheless be considered, and which imply shut down and appropriate inspection of the component or of the plant.

- *Level D*, including the fourth operating conditions (SF4), that represent the faulted conditions, which are highly improbable but whose consequences on component are studied among others for safety reasons.

The structural integrity assessment must be carried out taking into account both normal and accidental conditions, verifying the fulfillment of the related design criteria. In order to do that, the stress linearization procedure must be applied to the most critical regions (sections) of the component. This method consists in breaking down the stress tensor obtained along the thickness into membrane, bending and non-linear components as well as in primary, secondary and peak stress according to the specific design rules. For each failure mode, the so-called *utilization factor* can be obtained by the ratio of the combined equivalent stress to the specific allowable stress of the material reported in the standards, depending on both criterion and service level.

An outline of the RCC-MRx design rules to be applied for the design of the DEMO WCLL BB is given here-below. Due to the high nuclear classification of the breeding blanket (N1Rx component as per RCC-MRx), the design-by-analysis rules RB 3200 reported in Section III Tome 1 Subsection B used for Class N1Rx must be satisfied (see Table 3.2). Those criteria are the same as N2Rx components (RC 3200) that have been also proposed for the design of the ITER WCLL-TBM Set [64].

Different rules have to be considered depending upon whether creep and/or irradiation effects can be considered as negligible or not. For each combination, P-type and S-type damages are caused by monotonic and cyclic loads, respectively. The P-type failure modes are those which could result from applying constantly increasing loads, such as excessive deformation and plastic instability. Conversely, the S-type failure modes are those which could only result by repeatedly applying loads, such as progressive deformations (ratcheting) and fatigue.

	Negligible Creep	**Significant Creep**
Negligible Irradiation	RB 3251.1 (P-type damage) RB 3261.1 (S-type damage)	RB 3252.1 (P-type damage) RB 3262.1 (S-type damage)
Significant Irradiation	RB 3251.2 (P-type damage) RB 3261.2 (S-type damage)	RB 3252.2 (P-type damage) RB 3262.2 (S-type damage)

Table 3.2: RCC-MRx RB 3200 rules breakdown [63].

The application of the design rules relies on the classification of the stresses based on the nature of the loads generating those as well as the position in the structure. In particular, the stress can be classified as:

- *Primary stress* **P**. The primary stress is defined as that portion of the total stress which is required to satisfy equilibrium with the applied loading and which does not diminish after small scale permanent deformation. Small scale deformation is taken to mean deformation which does not lead either to appreciable change in geometry (large displacements) or to significant stretching (large local deformation). Along the wall thickness, the primary stress can also be subdivided into:
  - *General primary membrane stress* $\mathbf{P}_m$, which represents the thickness-averaged value of the primary stress tensor, where each component is given by

$$(\sigma_{ij})_m = \frac{1}{h}\int_{-h/2}^{+h/2} \sigma_{ij} dx \tag{3.1}$$

    where h is the wall thickness and x is the direction adjacent to the supporting line where the stress is computed through the thickness h.

  - *Primary bending stress* $\mathbf{P}_b$, which designates the stress distributed linearly through the thickness which has the same moment as the primary stress. It is obtained applying the following operation to the primary stress tensor as follow

$$(\sigma_{ij})_b = \frac{12x}{h^3} \int_{-h/2}^{+h/2} x\sigma_{ij} dx \tag{3.2}$$

  - *Local primary membrane stress* $\mathbf{P}_L$, defined as the sum of the general primary membrane stress $\mathbf{P}_m$ and an additional membrane stress denoted by $\mathbf{L}_m$, that is caused by mechanical loads applied to a gross structural discontinuity, or simply by the presence in the structure of a gross structural discontinuity

$$\mathbf{P}_L = \mathbf{P}_m + \mathbf{L}_m$$

    Although it does not have all the characteristics of a primary stress, prudence dictates that this stress $\mathbf{P}_L$ be classified as a primary stress.

- *Secondary stress* $\mathbf{Q}$. It represents that portion of the total stress (minus peak stresses, as defined below), which can be relaxed as a result of small scale permanent deformation. The basic characteristic of a secondary stress is that it is self-limiting. Local yielding and minor distortions can eliminate the conditions which cause the stress to occur. The stress classification $\mathbf{Q}$ includes only the constant (membrane) and linearly varying (bending) part of the secondary stress. $\mathbf{Q}$ is calculated by applying the procedures in Equations (3.1) and (3.2) to the secondary stress tensor and summing the membrane and bending parts. All thermal stresses, swelling stresses, and stresses due to imposed displacements or deformations are classified as secondary stresses.

- *Peak stress* $\mathbf{F}$. It is the increment of stress which is additive to the primary-plus-secondary stresses by reason of local discontinuities or local thermal stresses including the effects, if any, of stress concentrations. This additional stress, generally very localized and redistributed by plasticity, cannot cause an overall deformation of the structure. For ductile materials, it is objectionable only as a possible source of fatigue cracking or fast fracture damage and, at high temperature, of local cracking damage due to creep or creep-fatigue.

Negligible Creep and Negligible Irradiation

The rules RB 3251.1 (P-type damages) are conceived to assess the structural integrity of the component against two modes of failure directly related to the primary stress intensity in the material: immediate plastic collapse and immediate

plastic instability. If a structure is loaded above the yield strength of the material, plastic deformation occurs until the structure collapses either because of excessive deformation or necking. The limitation of primary stresses are defined by

$$\overline{P_m} \leq S_m \tag{3.3}$$

$$\overline{P_L + P_b} \leq 1.5 S_m \tag{3.4}$$

where the overline stands for the equivalent value of the stress tensor (i.e. Von Mises equivalent stress), 1.5 is a factor called *plastic collaboration coefficient*, well described in [65], and S_m is the allowable stress of the material defined in Level A by the following

$$S_m = \min \left[\frac{1}{2.7} R_{m,min}(20°); \frac{1}{2.7} R_{m,min}(T_{ave}); \frac{2}{3} R_{p02,min}(20°); \frac{2}{3} R_{p02,min}(T_{ave}) \right]$$

where $R_{m,min}$ is the minimum tensile strength, $R_{p02,min}$ is the minimum yield strength (conventionally assumed as the stress corresponding to a plastic deformation of 0.2%) and T_{ave} is the average temperature in the section considered. In case of Level C and Level D, the following relations are used to evaluate the allowable stresses S_m^C and S_m^D, respectively

$$S_m^C = \min \left[1.35 S_m; R_{p02,min} \right]$$

$$S_m^D = \min \left[2.4 S_m; 0.7 R_{m,min} \right]$$

As shown above, for this kind of criteria there is no limitation on secondary stresses.

The rules RB 3261.1 (S-type damages) are conceived to assess the structural integrity of the component against failure modes due to cyclic loads. In particular, the rule RB 3261.111 is about the ratcheting damage and the rule RB 3261.112 is about fatigue damage.

The ratcheting is the accumulation of plastic deformation in structures subjected to cyclic stressing with a non-zero primary stress. When a structure is subjected to cyclic loading, the structure may show signs of permanent deformation at the end of the first cycle. During subsequent cycles, two cases may arise: after a few cycles, the overall deformation is stable and the progressive incremental inelastic deformation is absent (i.e. shakedown or cyclic plasticity); the permanent overall deformation continues to increase as every loading cycle induces additional deformation and the structure gradually changes from its original shape until it eventually collapses. This behavior is called progressive deformation or ratcheting. The RCC-MRx reports two different approaches to check against the ratcheting failure mode: the main criterion based on efficiency diagrams and the alternative rule (RB 3261.1118). Since the

latter is both more conservative and easier to apply, it has been decided to use that instead of the efficiency diagrams. The rule is defined as follow

$$\max\left[\overline{P_L + P_b}\right] + \overline{\Delta Q} \leq 3S_m \tag{3.5}$$

where either the maximum of the local membrane plus bending primary stress and the range of the total secondary stress are defined inside the cycle.

Fatigue is a damage mode that may appear under cyclic loading. If the cyclic loads are too high, cracks can nucleate, propagate, and lead to the rupture of the component. The rule RB 3261.112 is defined in terms of fatigue usage factor V as follow

$$V = \sum_i \frac{n_i}{N_i} \leq 1 \tag{3.6}$$

where the index i refers to the i^{th} set of cycles of the same loading scenario, n_i are the specified number of cycles the component has to undergo and N_i are the allowable number of cycles derived from strain life curves of the material.

Assuming only one cyclic load (i.e. $i = 1$), N_i can be calculated once the total strain range intensity $\overline{\Delta\varepsilon}$ during a cycle is known. On the other hand, the adoption of a linear elastic approach does not allow a direct estimation of the total strain range, since the effects of plasticity above the yield point are not considered. In the RCC-MRx, the estimation of the *real* total strain range $\overline{\Delta\varepsilon}$, based on results from elastic analyses, is performed assuming that it is composed of four components, as follow

$$\overline{\Delta\varepsilon} = \overline{\Delta\varepsilon}_1 + \overline{\Delta\varepsilon}_2 + \overline{\Delta\varepsilon}_3 + \overline{\Delta\varepsilon}_4 \tag{3.7}$$

In particular,

- $\overline{\Delta\varepsilon}_1$ is the strain range evaluated from the outcomes of a linear elastic analysis as follow

  $$\overline{\Delta\varepsilon}_1 = \frac{2}{3}\frac{1+\nu}{E}\overline{\Delta\sigma_{tot}} \tag{3.8}$$

  where E is the Young modulus at maximum temperature in the cycle, ν is the Poisson modulus and $\overline{\Delta\sigma_{tot}}$ is the total elastic stress at the point under investigation such as $\overline{\Delta\sigma_{tot}} = \overline{\Delta\left(P + Q + F\right)}$

- $\overline{\Delta\varepsilon}_2$ is the *plastic* strain increase due to potential ranging of primary stress (negligible for blanket normal operation)

  $$\overline{\Delta\varepsilon}_2 = \overline{\Delta\left[P_m + 0.67\left(P_b + P_L - P_m\right)\right]} \tag{3.9}$$

- $\overline{\Delta\varepsilon}_3$ is the plastic strain drawn from the cyclic stress-strain curve of the material at the maximum temperature reached during the cycle. Its value is given by the intersection of the cyclic stress-strain curve with the Neuber

hyperbola $\overline{\Delta\sigma\Delta\varepsilon} = \overline{\Delta\varepsilon}_1\overline{\Delta\sigma_{tot}}$ (when $\overline{\Delta\varepsilon}_2 = 0$). It can be also computed by means of the factor K_ε describing the effects of plasticity in the material and given by the standards, as follow

$$\overline{\Delta\varepsilon}_3 = (K_\varepsilon - 1)\,\overline{\Delta\varepsilon}_1 \qquad \text{when } \overline{\Delta\varepsilon}_2 = 0 \tag{3.10}$$

- $\overline{\Delta\varepsilon}_4$ represents the strain increase due to triaxiality. As previously, it can be computed by means of a correction factor K_ν reported in the standards, as follow

$$\overline{\Delta\varepsilon}_4 = (K_\nu - 1)\,\overline{\Delta\varepsilon}_1 \qquad \text{when } \overline{\Delta\varepsilon}_2 = 0 \tag{3.11}$$

Nevertheless, the rules of RB 3261.112 only apply if the rule RB 3261.111 (ratcheting) is satisfied.

As can be easily agreed, no S-type damages can be addressed to off-normal conditions (i.e. Level C and Level D).

Negligible Creep and Significant Irradiation

When irradiation effects are not negligible, rules RB 3251.2 and RB 3261.2 must be applied for P-type and S-type damages, respectively.

Concerning the former, the following rules RB 3251.2121 and RB 3251.2122 are conceived for preventing failure against immediate plastic flow localization and immediate fracture due to exhaustion of ductility in linear elastic analyses, respectively.

$$\overline{P_m + Q_m} \leq S_{em} \tag{3.12}$$

$$\overline{P_m + P_b + Q + F} \leq S_{et} \tag{3.13}$$

where S_{em} and S_{et} are two different maximum allowable stresses, depending both upon temperature, neutron irradiation damage and service level.

Regarding the verification against S-type damages, the RB3261.2 rules state that, when irradiation is significant, the rules in RB 3261.112 for elastic analysis should be verified using the cyclic curve without irradiation (and the associated K_ε and K_ν coefficients) and fatigue curve under irradiation. If the latter is not provided, the fatigue curve without irradiation can be used.

Significant Creep and Negligible Irradiation

The rules RB 3252.1 and RB 3262.1 must be checked when creep effects are not negligible. In particular, for P-type damages, the rule is defined in terms of creep usage factor U as follow

$$U\left(\Omega\overline{P_m}\right) = \sum_j \frac{t_j}{T\left(\Omega\overline{P_m}\right)_j} \leq 1 \tag{3.14}$$

$$U\left(\overline{P_L + \Phi P_b}\right) = \sum_j \frac{t_j}{T\left(\overline{P_L + \Phi P_b}\right)_j} \leq 1 \tag{3.15}$$

where the index j refers to the j^{th} interval, t_j is the duration of the specified time interval and T_j is the maximum time interval duration allowed as a function of the primary stresses, computed by means of stress-time to 1% strain curves. The coefficients Ω ($\approx$1) and Φ ($\approx$0.67) introduce the effect of the local membrane stresses as well as multiaxial stress states and of the redistribution of stresses because of relaxation, respectively. However, if conservatively the (maximum) temperature is considered as constant during the whole operating period [62], Equations (3.18) and (3.19) can be simplified in

$$\Omega\overline{P_m} \leq S_t\left(T_m, t\right) \tag{3.16}$$

$$\overline{P_L + \Phi P_b} \leq S_t\left(T_m, t\right) \tag{3.17}$$

where T_m is the thickness-averaged temperature, t is the operating time and S_t is the creep allowable stress given by

$$S_t = \min\left[\frac{2}{3}S_r; S_{c,1\%}; 0.8S_{min,3^{rd}}\right]$$

where S_r is the minimum stress to cause creep rupture in time t at given temperature, $S_{c,1\%}$ is the minimum stress to produce 1% strain in time t at given temperature and $S_{min,3^{rd}}$ is the minimum stress causing tertiary creep after time t at given temperature. As the above-mentioned rule applies basically to normal operating conditions, creep failure during accidental conditions are checked by means of the creep rupture usage factor W defined as follow

$$W\left(1.35\Omega\overline{P_m}\right) \leq 1 \tag{3.18}$$

$$W\left[1.35\left(\overline{P_L + \Phi P_b}\right)\right] \leq 1 \tag{3.19}$$

The creep rupture usage fraction W is calculated as the creep usage fraction U, but using the minimum stress to rupture S_r.

Cyclic loads combined with holding time at high temperatures (i.e. during the flat top of the cycle), fatigue and creep effects act simultaneously and into creep-fatigue failure mode may arise, as described in rules RB 3262.1. In RCC-MRX, the damage resulting from the accumulation of the effects of creep and fatigue is estimated relying on combination of the fatigue usage fraction $V\left(\Delta\varepsilon\right)$ and the creep rupture usage fraction $W\left(\sigma\right)$, which must fall inside the allowable area given by the *creep-fatigue interaction diagram* of the material.

Under elastic conditions, the value of the total strain range must be corrected for

the effects of creep in the calculation of the fatigue usage fraction, as follow

$$\overline{\Delta\varepsilon_{tot}} = \overline{\Delta\varepsilon_{el+pl}} + \overline{\Delta\varepsilon_c} \tag{3.20}$$

where $\overline{\Delta\varepsilon_{el+pl}}$ is the same as Equation (3.7), and $\overline{\Delta\varepsilon_c}$ is the additional creep strain that can be obtained in the following way:

1. determine the *real* stress $\overline{\Delta\sigma^*}$ from the cyclic stress vs. strain curve of the material (computed at the maximum temperature of the cycle T^*) corresponding to the strain $\overline{\Delta\varepsilon_{el+pl}}$

2. determine the symmetrization coefficient K_S obtained as a function of the ratio $\overline{\Delta\sigma^*}/2R_{p02,min}(T^*)$. For Eurofer97 this value is given as constant and equal to 0.5.

3. calculate the highest value during the holding time of primary stress intensity given by
$$\overline{P_{max}} = \max\left[\overline{P_m + 0.67\,(P_b + P_L - P_m)}\right] \tag{3.21}$$

4. compute the primary stress range $\overline{\Delta P}$, as done for Equation (3.9). As already stated, this value is negligible for blanket applications.

5. calculate the secondary stress range as
$$\overline{\Delta S^*} = \overline{\Delta\sigma^*} - \overline{\Delta P} \approx \overline{\Delta\sigma^*} \tag{3.22}$$

The value of $\overline{\Delta\varepsilon_c}$ is then the creep strain due to the stress $\sigma_k = \overline{P_{max}} + K_S\overline{\Delta S^*}$ applied for a time t^*. Such value can be obtained using isochron stress vs. strain curves of the material, evaluated at temperature T^*.

Once the total strain $\overline{\Delta\varepsilon_{tot}}$ is determined, the maximum allowable number of cycles N_j can be thus drawn from the strain life design curves, and the fatigue usage fraction $V_{f,j}$ for the j^{th} type of cycle can be finally computed as

$$V_{f,j} = \frac{n_j}{N_j} \tag{3.23}$$

where n_j is the number of cycles (j^{th} type of cycle) the component is supposed to perform.

The computation of the creep rupture usage fraction for the creep-fatigue damage mode is carried out in the same way as done in Equation (3.18), with the except of using the stress $\sigma_{k,j}/0.9$, where j stands for the j^{th} type of cycle, instead of the primary stress $1.35\Omega\overline{P_m}$, by using the stress to rupture curves evaluated at T^*. Once determined the maximum allowable time before rupture T_j, the creep rupture usage

fraction $W_{c,j}$ is given by

$$W_{c,j} = \frac{t_j}{T_j} \tag{3.24}$$

where t_j is the operating time of the component.

The final creep-fatigue damage rule is finally computed by summing the two contributions, that has to be lower than a certain damage limit D',

$$\sum_j \frac{n_j}{N_j} + \sum_j \frac{t_j}{T_j} \leq D' \tag{3.25}$$

where j is the number of different cycles the component undergoes. A smart approach to determine the remaining lifetime of the component is given by the use of the *creep-fatigue interaction diagram* (see Figure 3.6), where the creep rupture usage factor $W_c = \sum_j (t_j/T_j)$ and the fatigue usage factor $V_f = \sum_j (n_j/N_j)$ are reported in the y-axis and x-axis, respectively. Instead of using linear accumulation,

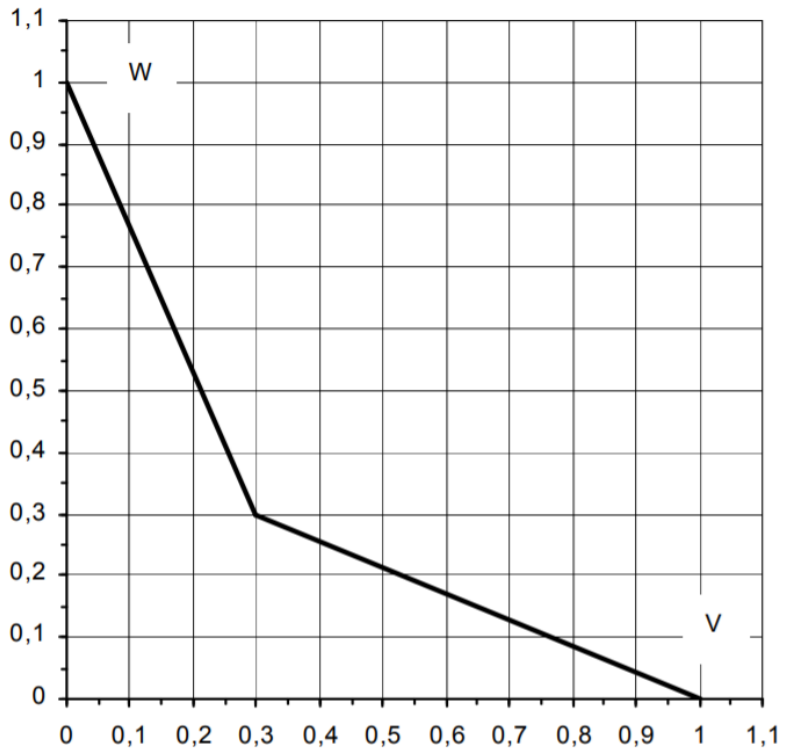

Figure 3.6: Creep-fatigue interaction diagram as per RCC-MRx.

a central point (0.3;0.3) is defined to change the shape of the safe region in the diagram, i.e. the area below the curves.

Nonetheless, the main concern for the applicability of this rule is again the cyclic softening of the material, which decreases creep resistance and increases creep strain rates. Several competing effects must be taken into account and more experimental tests are needed in order to complete the validation of the diagram.

Significant Creep and Significant Irradiation

When both creep and irradiation effects are significant, the rules RB 3252.2 and RB 3262.2 must be applied for P-type and S-type damages, respectively. While for the latter only rules for austenitic steels have been developed (out of our scope), the criterion for monotonic loads foresees the verification of the rules of 3252.1 (significant creep and negligible irradiation) using the limits on usage fractions U and W equal to 0.1 instead of 1.

3.3 First Wall Optimization

Once introduced the main features and requirements of the European DEMO WCLL BB concept, the optimization process carried out to improve the FW cooling channels layout will be described in this section.

Firstly, a description of the parametric FE model representative of the equatorial cell of the DEMO WCLL BB, built-up in COMSOL, will be given. The numerical model is needed, indeed, in order to evaluate the thermo-structural performances of the blanket, included as part of the constraints in the optimization problem, that can vary with different cooling channels layout.

Secondly, the set-up of the constrained optimization problem will be discussed. With the aim to improve the tritium breeding performances of the WCLL BB concept, a series of MCNP neutron transport simulations have been carried out in order to identify a potential objective function whose minimization allows improvements in tritium breeding performances.

Being also a constrained problem, the whole set of inequality constraints imposed to the problem will be described, based on the description of the requirements reported in the previous section.

Finally, the results of the optimization problem solved by using the Complex method will be reported and critically discussed.

3.3.1 Parametric FE Model of the DEMO WCLL BB

According to what stated above, the assessment of the thermo-mechanical performances of the blanket is pivotal to lead the designers toward the optimum point. In fact, the best design is featured not only by the best performances, but also by the compliance with all the prescribed requirements.

For complex systems as the fusion breeding blankets, the only reliable way to evaluate their thermo-structural response is the FEM analysis. According to that, a parametric FE model of the DEMO WCLL BB concept described above has been implemented in COMSOL environment, and all its features are here-below reported.

FE Model and Geometrical Parameters

The numerical model built-up in COMSOL relies on the equatorial cell of the WCLL COB segment. In particular, the model considers the structural domains (i.e. W-armour, SB, DWTs) and the breeder (see Figure 3.7). In order to reduce a lot the huge computational time usually required for optimization studies, the water domain has not been modelled, but its cooling effect replaced by means of specific convective boundary conditions that will be described in the following sections. Moreover, exploiting its toroidal symmetry, only half model of the elementary cell has been simulated.

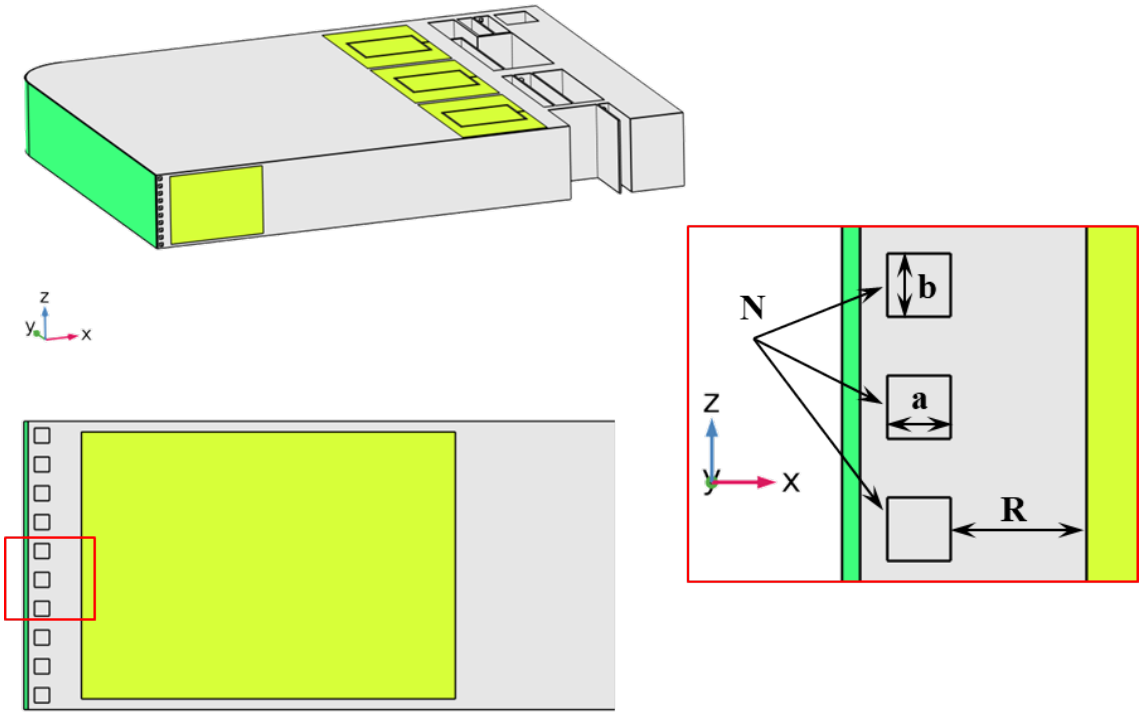

Figure 3.7: Geometrical parameters of the FW cooling channels layout.

Since the optimization study aimed at identifying the best topology and position of the FW cooling channels layout, the geometrical model has been parametrized depending upon the definition of a certain number of design parameters related to the cooling channels layout. In particular, the uniqueness of the channels layout can be defined by means of four geometrical parameters (see Figure 3.7):

- **N** [-], which is the number of channels per cell;
- **R** [mm], which represents the radial (x-axis) distance between the BZ-side of the cooling channels and the BZ itself;
- **a** [mm], which is the radial (x-axis) dimension of the cooling channel;
- **b** [mm], which represents the poloidal (z-axis) dimension of the cooling channel.

Because of the parametrization, both the geometrical and the related FE model are updated in every step of the optimization study, according the values of the parameters at that step.

Even though the mesh varies from one step to another, each one has been built-up adopting quadratic tetrahedral elements (see Figure 3.8), for both thermal and mechanical analyses, with an average number of $1{\cdot}10^5$ nodes connected into $5{\cdot}10^5$ elements, on average.

Such a mesh size has been selected after a preliminary sensitivity analysis aimed at reducing the number of nodes as much as possible (so to reduce the huge computational time required for optimization studies) while keeping an acceptable accuracy of the results.

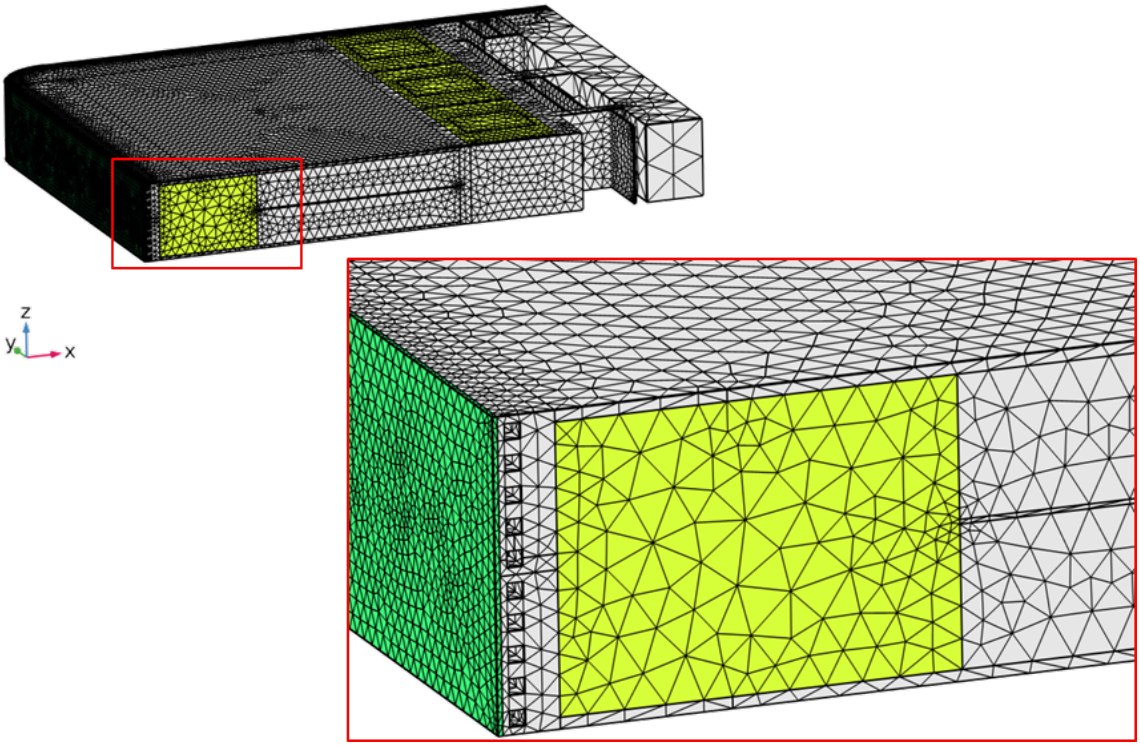

Figure 3.8: Parametric FE model of the equatorial cell of the WCLL COB segment.

Material Properties

The full thermo-mechanical assessment of the breeding blanket requires the knowledge of the thermal field arising within the structure under the effect of heat loads and boundary conditions. Since material properties can vary a lot with temperature, temperature-dependent thermo-physical properties of the material have been assigned to each domain.

However, mechanical properties (i.e. Young modulus, Poisson modulus and thermal expansion coefficient) have been implemented only to Eurofer97, being the Segment Box the only component considered for the structural analyses.

In fact, even the W-armour has been excluded from the latter, being it foreseen as composed of a set of non-continuous *tiles* that should not act any significant compressive/tensile action onto the FW. As to the latter, thermo-mechanical analyses presented in [16] have shown that, if modelled as continuum solid, the presence of the W-armour adds an unrealistic compressive effect onto the FW structure, mainly due to the difference in terms of thermal expansion coefficient.

For Eurofer97, data have been drawn mainly from the RCC-MRx [63] and, when missing, from the EUROfusion material handbook [19]. The whole set of data implemented have been reported in Table 3.3.

T [°C]	$\boldsymbol{\rho}$ [kg/m^3][63]	**k** [W/(m·°C)][19]	$\mathbf{c}_p$ [J/(kg·°C)][19]	$\boldsymbol{\alpha}$ [10^{-6}/°C][19]	**E** [GPa][63]	$\boldsymbol{\nu}$ [-][63]
20	7760	28.08	439	10.3	217	0.3
100	7740	29.79	490	10.7	213	0.3
150	7727				210	0.3
200	7713	30.38	523	11.2	207	0.3
250	7699				205	0.3
300	7685	30.01	546	11.6	202	0.3
350	7670				199	0.3
400	7655	29.47	584	11.9	196	0.3
450	7640				194	0.3
500	7625	29.58	660	12.2	190	0.3
550	7610				183	0.3
600	7594	31.12	800	12.3	176	0.3

Table 3.3: Eurofer97 thermo-physical properties [19][63].

As to the tungsten, the analyses have been carried out considering the data presented in [66]. The correlations used have been reported in Table 3.4.

Finally, the Lithium-Lead properties have been drawn from [67] and the data and/or correlations used have been reported in Table 3.5.

Property	**Correlation**	**Range**
$\boldsymbol{\rho}$ [kg/m^3]	$19302.7 - 0.23786 \cdot T - 2.2448 \cdot 10^{-5} \cdot T^2$	$20 \leq$ T [°C] ≤ 1200
k [W/(m·°C)]	$174.9274 - 0.1067 \cdot T + +5.0067 \cdot 10^{-5} \cdot T^2 - 7.8349 \cdot 10^{-9} \cdot T^3$	$20 \leq$ T [°C] ≤ 1000
$\mathbf{c}_p$ [J/(kg·°C)]	$128.308 + 0.032797 \cdot T - 3.4097 \cdot 10^{-6} \cdot T^2$	$20 \leq$ T [°C] ≤ 1000

Table 3.4: Tungsten (ITER-grade) thermo-physical properties [66].

Property	Correlation	Range
$\boldsymbol{\rho}$ [kg/m^3]	$10520.35 - 1.19051 \cdot T$[K]	$235 \leq$ T [°C] ≤ 607
$\mathbf{k}$ [W/(m·°C)]	$14.51 + 0.019631 \cdot T$[°C]	$235 \leq$ T [°C] ≤ 600
$\mathbf{c}_p$ [J/(kg·°C)]	$195 - 9.116 \cdot 10^{-3} \cdot T$[K]	$235 \leq$ T [°C] ≤ 527

Table 3.5: Lithium-Lead thermo-physical properties [67].

Loads and Boundary Conditions

As already done in the past [14][42], two relevant operating scenarios need to be investigated for the WCLL BB design: (1) the Normal Operation (NO) scenario, and (2) the Over-Pressurization (OP) scenario.

While the former can be represented by the steady-state condition reached during the flat top of each DEMO pulse, the latter corresponds to an accidental scenario following a rupture of one (or more) DWT inside the BZ (e.g. in-box LOCA) leading to an over-pressurization of the SB.

According to that, different sets of thermal and mechanical loads and boundary conditions have to be applied during the simulation in order to investigate both the loading scenarios.

As to the thermal loads and boundary conditions, it is possible to assume preliminary that the temperature distributions in either fluids and structure do not change significantly from the NO scenario to the OP scenario (considering the first time instants after the DWT break). Hence, for the heat transfer simulation the following set of loads and boundary conditions pertinent to the steady-state NO scenario are used:

- surface heat flux q'' [MW/m^2] onto the W-armour plasma facing surface;
- volumetric density of nuclear-deposited heat power (or nuclear heating) q''' [MW/m^3];
- forced convective heat transfer at coolant/wall interface;
- pure diffusive heat transfer within the breeder (assumed as stagnant).

Regarding the heat flux acting onto the W-armour plasma facing surface, the value of 0.32 MW/m^2 has been applied, pertinent to the equatorial region of the COB segment [16]. The value has been applied uniformly on the straight part of the FW, whereas a cosine law has been used in correspondence of the bends connecting the FW to the SWs (see Figure 3.9).

The non-uniform nuclear heating distribution inside the equatorial cell has been considered by using the radial profiles computed at University of Palermo by means of MCNP neutron-photon transport analyses carried out on fully heterogeneous model of a recent, similar version of the equatorial cell [68].

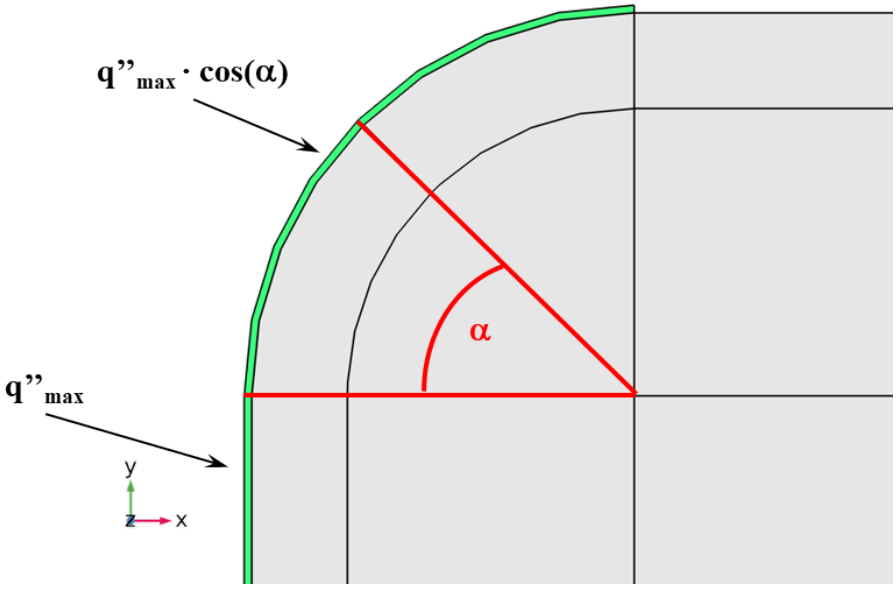

Figure 3.9: Surface heat flux onto the FW bends.

Figure 3.10 shows a cut view of the 3D MCNP model used for the analysis and the nuclear heating radial profiles obtained for different domains of the cell, used for the optimization analyses.

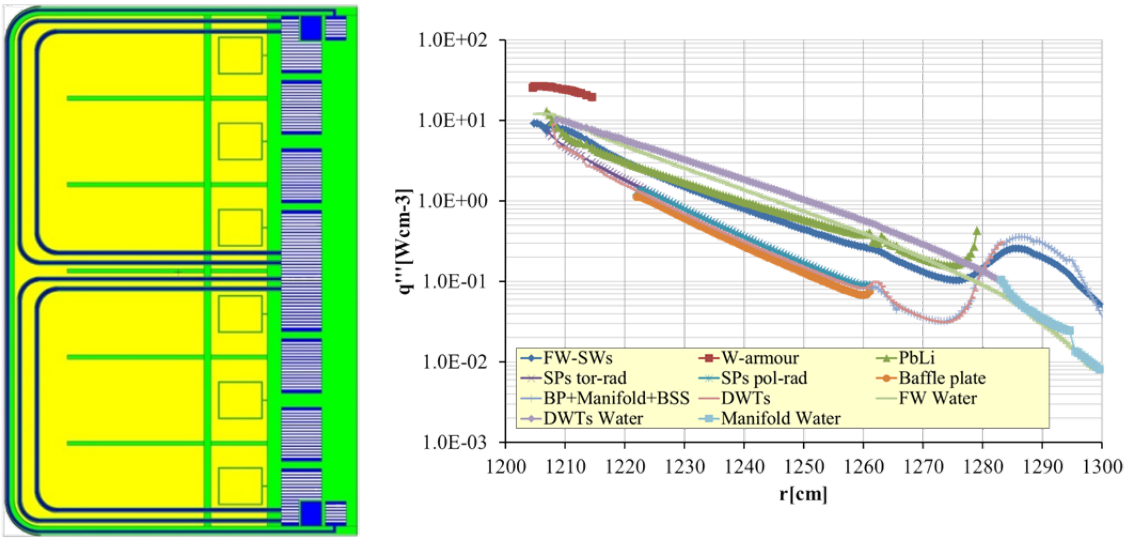

Figure 3.10: MCNP5.1.6 model of the equatorial cell (left) and radial distributions of the non-uniform nuclear heating obtained for different components (right) [68].

Although the change of the FW channels layout has an impact on the nuclear heating distributions in the elementary cell, the radial profiles in Figure 3.10 have been used independently from the configuration analysed during the optimization process. Indeed, the weak dependency of the nuclear heating profiles from the cooling channels layout has been already confirmed in [69]. On the other hand, performing a neutron-photon transport simulation for each configuration would have

a required a massive computational and time effort.

Since water domain is not modelled, proper convective boundary conditions have been imposed at the coolant/wall interfaces. In particular, the following iterative procedure has been adopted for each FW cooling channels layout analysed:

1. First analysis run with uniform bulk temperature set to the average temperature of 311.5 °C and initial heat transfer coefficients (different for FW channels and DWTs) computed by the Dittus&Bölter correlation [70],

$$h = Nu\frac{k}{D_h} = 0.023Re^{0.8}Pr^{0.4}\frac{k}{D_h}$$

   assuming first attempt mass flow rate for either the DWTs circuit and the FW cooling system, and calculating the coolant thermo-physical properties at its average temperature.

2. Evaluation of the power extracted by the coolant flowing through each cooling circuit (FW and DWTs) and calculation of the pertaining revised mass flow rates assuming the nominal in-out ΔT_n of 33 °C (295 °C - 328 °C) for the coolant, as follow

$$\dot{m}_j = \frac{2\int_{A_j} q''(A_j)dA_j + Q_{nh,j}}{c_{p,ave}\Delta T_n}$$

   where j stands for j^{th} cooling circuit (i.e. FW or DWTs), A_j is the coolant-wetted surface of the j^{th} circuit, $q''(A_j)$ is the outward heat flux crossing that surface, $Q_{nh,j}$ is the total heat power due to nuclear heating inside the water domain of the j^{th} circuit, computed by the nuclear analysis in [68] (i.e. $Q_{nh,FWwater}$=10.224 kW, $Q_{nh,DWTswater}$=6.659 kW). The factor 2 multiplying the surface integral of the heat flux is due to the fact that thanks to its toroidal symmetry, only half of the cell has been modelled.

3. Sub-sequential analysis run with the revised heat transfer coefficients based on the mass flow rates computed in the Step 2.

By means of this iterative procedure (usually, no more than two iterations are needed), it has been possible to get more realistic heat transfer coefficients for each blanket configuration, as a function of the required mass flow rates to have the prescribed ΔT. Conversely, a first-kind boundary condition (i.e. fixed temperature) has been imposed to the water-wetted surfaces of the manifold region, considering the average temperature of 311.5 °C.

Finally, the breeder domain has been modelled as a solid domain (i.e. stagnant breeder), neglecting the contribution due to advection on its heat transport mode. This assumptions has been already adopted in several studies [14][36][58][59] and can be justified by its very low velocity inside the cell as well as the MHD effects on its flow.

As far as the mechanical simulations are concerned, the loads and the boundary conditions pertinent to both NO and OP loading scenarios have been taken into account:

- pressure loads onto the cooling water-wetted surfaces: 15.5 MPa under NO scenario and 18.6 MPa under OP scenario;
- pressure loads onto the breeder-wetted surfaces: 0.5 MPa under NO scenario and 18.6 MPa under OP scenario;
- thermal expansion induced by the thermal field predicted by the steady state thermal analysis;
- a proper set of mechanical constraints, with the aim of simulating the structural behaviour of the DEMO breeding blanket as realistic as possible (see Figure 3.11).

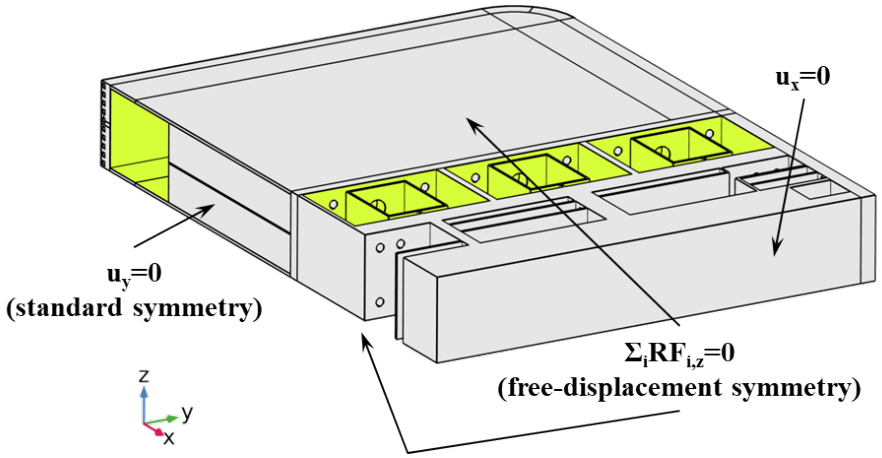

Figure 3.11: Mechanical constraints on the parametric FE model of the WCLL COB equatorial cell.

In particular, the adopted mechanical constraints prevent the radial (x) displacement of the nodes on the back surface of the BSS and the toroidal (y) displacement of the nodes on the middle toroidal plane of the whole elementary cell. Regarding the poloidal displacement, a *free-displacement* symmetry condition has been applied to both the poloidal surfaces of the cell, in order to allow all the i nodes belonging to each symmetry plane to translate in the normal (z) direction of a uniform displacement, determined by the criterion that there is no resulting reaction force (RF) in the normal direction. Such mechanical restraints on the two poloidal surfaces based on the *plane strain* assumption have been already used in the past [36][42] and, even though it might be misleading on the FW behaviour, it represents the easiest and most widely adopted option so far.

Solutions and Post-Processing

Once identified all the loads and boundary conditions acting onto the WCLL BB equatorial cell, the overall thermo-structural response of each FW channels configuration has been obtained by means of the following sequence of simulations:

1. a first study to evaluate the thermal field arising within the structure at the end of the flat top of each DEMO pulse. To do that, the above-mentioned iterative procedure has been applied and a couple of steady-state thermal analyses are carried out to converge to a final temperature distributions.

2. Two linear elastic structural analyses are performed applying only the primary loads (i.e. pressure loads) pertinent to NO and OP scenario, respectively, in order to compute the primary stresses arising within the structure under the combined effects of loads and boundary conditions.

3. Finally, a linear elastic structural analysis is carried out considering only the secondary loads (i.e. only the thermal expansion) relying on the thermal field obtained from Step 1. From this last analysis, the distribution of secondary stresses is computed.

The evaluation of the peak stresses (requiring the combined action of primary and secondary loads) has not been considered for the FW optimization analysis, and will be performed only during the final structural analysis of the optimized configuration (presented in Chapter 4), where it has been possible to adopt a more detailed model discretization.

The structural performances of each FW configuration analysed are evaluated out adopting the linear elastic approach as suggested in the RCC-MRx. Such code foresees the use of the stress linearization procedure to be performed in the most critical regions of the component. In order to do that, a set of Supporting Lines (SLs) is identified, placed along the thickness of the sections to be assessed. As far as the parametric FE model of the equatorial cell, the attention has been focused on the object of the optimization, i.e. the complex of FW and SW. In particular, a set of ten (parametric) supporting lines have been selected, as shown in Figure 3.12, placing six of them at the middle of the FW, whereas other four ones in correspondence of the bend between the FW and the SW.

Such set of paths allows to check the stress level in correspondence of the most relevant sections of the FW, looking at the points with maximum bending (i.e. SL 1, SL 2, SL 3, SL 7) and maximum resulting moment (i.e. SL 9, SL 10). Furthermore, the region at the FW bend (i.e. SL 4, SL 5, SL 6, SL 8) needs also attention due to bending effects.

As already described in the section concerning the structural requirements, the verification of the design criteria is performed comparing an equivalent stress,

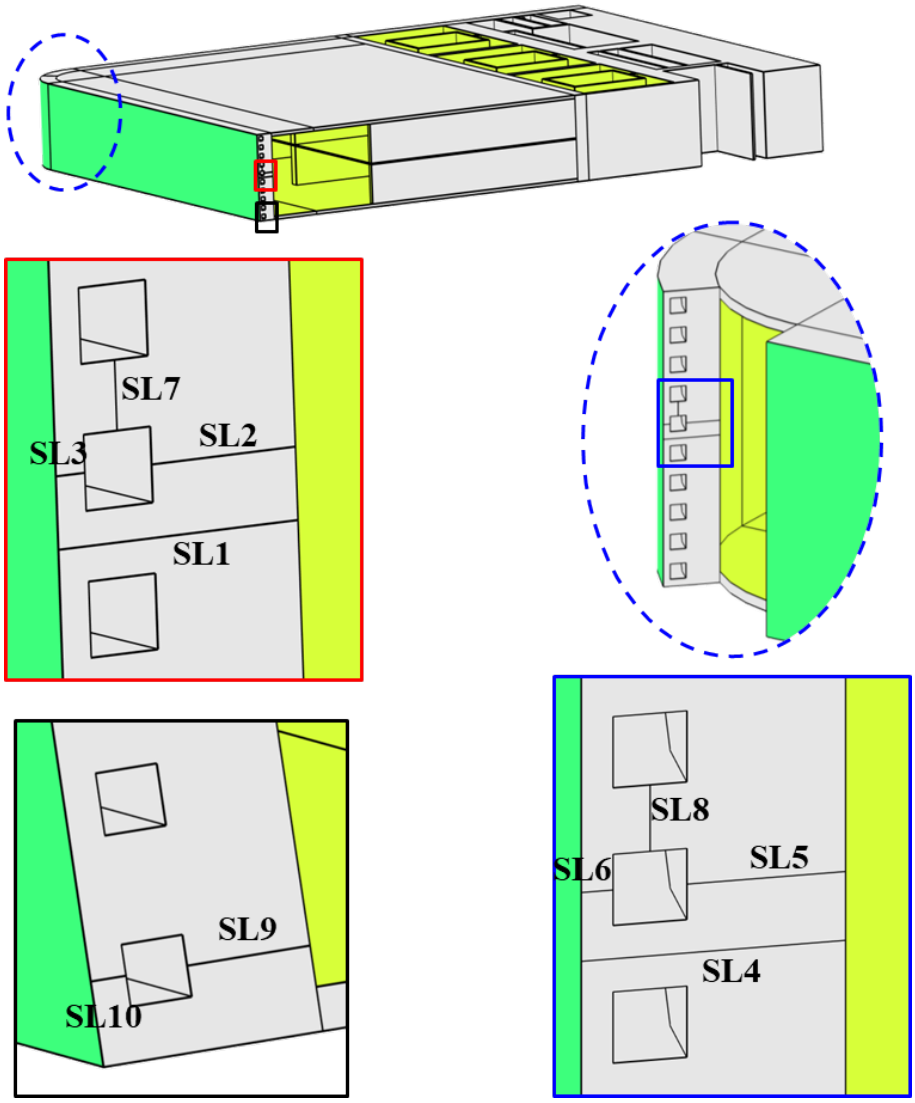

Figure 3.12: Supporting lines used for stress linearization procedure.

combining different kind of stresses depending upon the criterion, with the specific allowable stress presented above, depending also upon the service level. In particular, according to the standards, the NO and the OP scenarios are classified as Level A and Level D, respectively.

During the optimization process, not all of the RCC-MRx design criteria have been taken into account, but only the ones considered as more relevant and severe for the FW design. In particular, verifications against exhaustion of ductility, fatigue, creep-rupture and creep-fatigue failure modes have been excluded and verified only during the structural integrity assessment of the optimized cell reported in Chapter 4.

According to that, the stress analysis has been carried out taking into account three different allowable stresses S_m, S_t and S_{em} for Eurofer97. Their values are reported respectively in Figures 3.13 to 3.15, as a function of both temperature and service level.

Since it was not possible to draw the stress limits S_t and S_{em} from the RCC-MRx 2012 edition, [19] and [71] have been selected as sources for them.

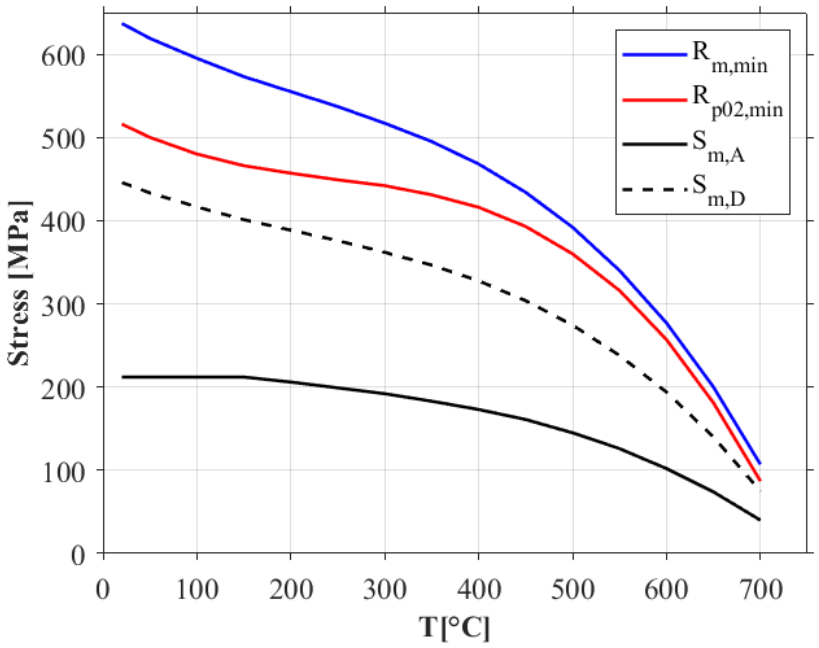

Figure 3.13: Eurofer97 allowable stress S_m vs. temperature [63].

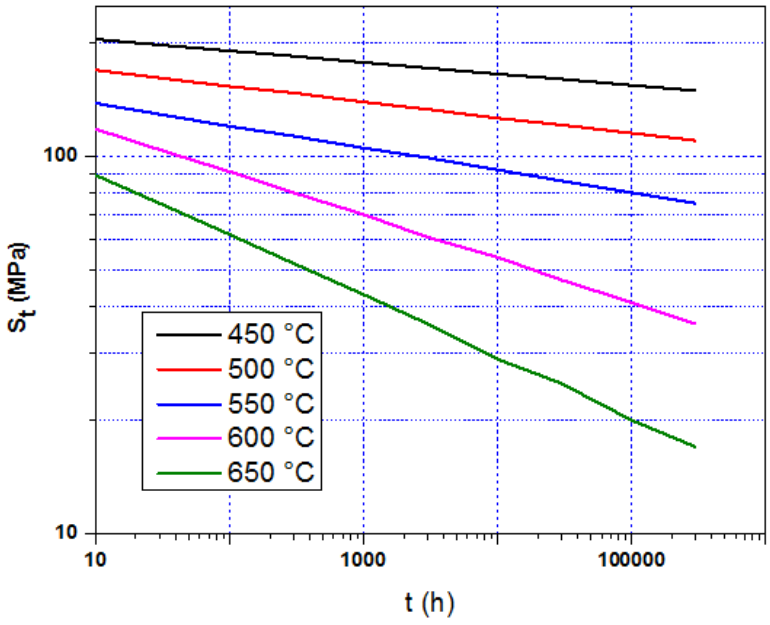

Figure 3.14: Eurofer97 allowable stress S_t vs. time-to-1%strain [19] (not available in RCC-MRx 2012 edition).

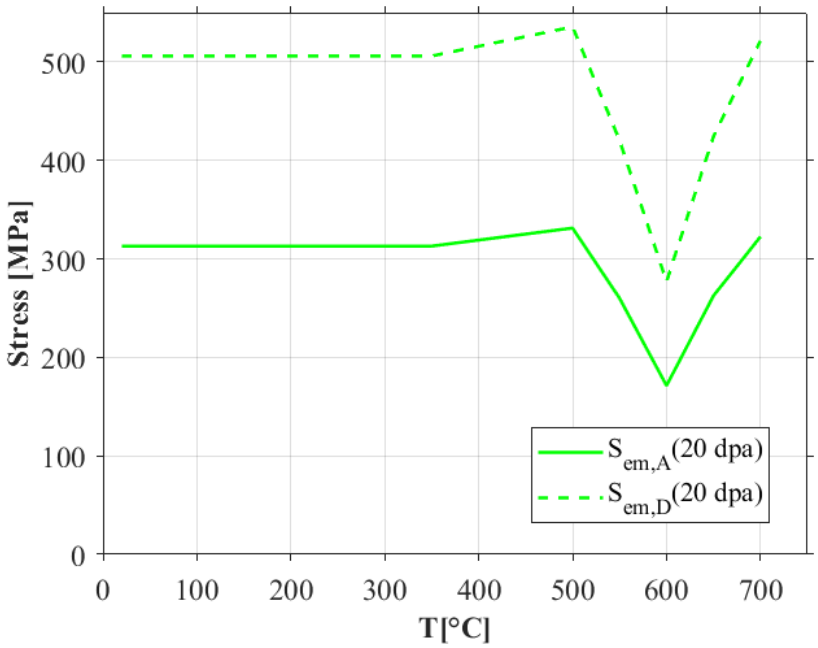

Figure 3.15: Eurofer97 allowable stress S_{em} vs. temperature [71] (not available in RCC-MRx 2012 edition).

3.3.2 Objective Function and Constrained Problem Set-Up

As stated above, the main goal of this work is to present an optimization procedure to enhance the water-cooled breeding blankets design, taking as reference the European DEMO WCLL BB concept. According to that, the optimization analysis here-presented focused on the identification of a layout for the FW cooling channels that might improve the tritium breeding performances (i.e. the TBR) of such concept, while complying with most of the severe thermal-hydraulic and structural requirements.

Objective Function Definition

Any optimization method requires the definition of an objective function to be minimized (or maximized) to get the desired result.

Focusing on the main object of this work, the ideal objective function is represented by the hypothetical function

$$TBR(\mathbf{X}) = TBR(N, R, a, b) \tag{3.26}$$

where $\mathbf{X}$ is the design vector containing the four design variables identified above ($\mathbf{X} = [N, R, a, b]$).

However, the definition of a function like that above would be very demanding and tough to achieve. In fact, it would require several hundreds of MCNP neutron transport analyses and, finally, a trial of a multiple regression analysis in order to fit

all the variables into a single function. Moreover, handling different kind of variables, being N a discrete variable whereas R, a and b are continuous, would make this last step much more complex. Considering the aim of this work, mostly oriented towards the definition of a general procedure, such activity has been considered out of scope, and a rational-heuristic approach has been adopted instead, identifying a potential objective function based on rational assumptions requiring less nuclear analyses.

According to that, the leading idea was to determine a scalar function $f(\mathbf{X})$ of the vectorial variable $\mathbf{X}$ so that minimizing $f(\mathbf{X})$ implies maximizing the TBR. The function $f(\mathbf{X})$ is defined as

$$f(\mathbf{X}) : \Omega \rightarrow \mathbb{R} \qquad \text{with} \qquad \mathbf{X} = [N, R, a, b]$$

where Ω represents the phase space of the four variables N, R, a and b.

The relation between the TBR and $f(\mathbf{X})$ has been investigated by means of several neutron transport analyses carried out on the same layout as the parametric model FE model of the WCLL BB, but considering the whole elementary cell rather than half. In particular, a numerical approach based on the Monte Carlo method has been used adopting the MCNP5.1.6 code [74] along with the JEFF3.2 cross section libraries [75]. A fully heterogeneous 3D MCNP model of the equatorial slice has been set up (see Figure 3.16), and the same planar neutron source built-up within a recent collaboration between the University of Palermo and the Karlsruhe Institute of Technology [72][73] has been used.

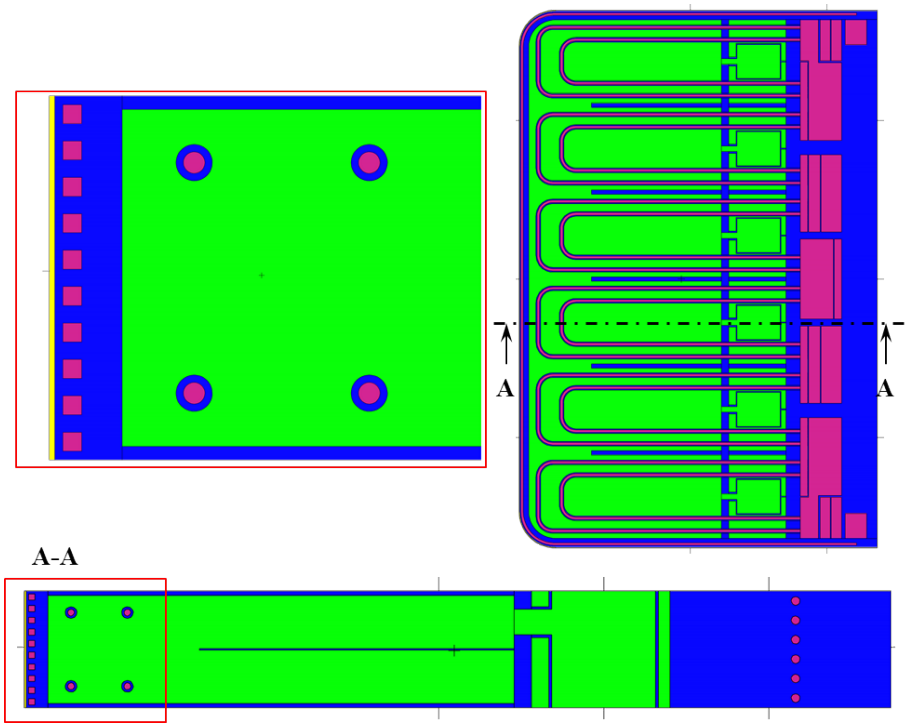

Figure 3.16: 3D fully heterogeneous MCNP model of the WCLL COB equatorial cell (configuration with N=10, R=15 mm, a=7 mm, b=7 mm).

In particular, such source takes into account both the neutrons coming directly from the plasma (D-T reactions) and the neutrons due the albedo in the whole DEMO reactor. As far as the boundary conditions are concerned, pure reflecting boundary conditions have been imposed to the top and bottom poloidal surfaces, whereas *white* boundary conditions [76] have been applied to the toroidal direction, as already used in [73].

With the aim to investigate how the tritium breeding performance of the elementary cell is affected by the water amount and distribution in the FW, eight MCNP models have been set-up, each one equipped with a different FW channels layout. In particular, the configurations reported in the Table 3.6 correspond to the matrix of cases analysed. The analyses have been carried out by simulating a large number of histories ($\sim 10^{10}$) so that the results obtained are affected by relative errors lower than 1% even in the slice regions more distant from the source.

Configuration	**N** [-]	**R** [mm]	**a** [mm]	**b** [mm]	**TBR** [-]
#1	10	15	7	7	3.207E-01
#2	5	15	7	7	3.141E-01
#3	10	5	7	7	3.313E-01
#4	5	5	7	7	3.191E-01
#5	10	9.75	12.25	4	3.216E-01
#6	10	18	4	12.25	3.189E-01
#7	5	9.75	12.25	4	3.153E-01
#8	5	18	4	12.25	3.134E-01

Table 3.6: Matrix of cases with TBR results.

As shown in the table, the first investigation carried out was to assess the impact of the water amount (represented by the term $N \cdot a \cdot b$), without changing neither the aspect ratio of the channel (i.e. b/a) nor the distance R. In order to do that, two cases equipped with 10 and 5 cooling channels (Case #1 and Case #2, respectively) have been analysed, considering the reference dimensions of the channels (7 mm x 7 mm) with R=15 mm.

Secondly, starting from the first two cases, the impact of the distance between the channels and the BZ has been evaluated reducing R from 15 mm to 5 mm, for both the configurations with 10 (Case #3) and 5 (Case #4) cooling channels.

Finally, other four simulations (from Case #5 to Case #8) have been performed keeping, for the two main cases 1 and 2, the same number of channels N as well as the water amount Nab but changing the aspect ratio b/a of the channels, together with R accordingly. For each configuration the channels have been re-arranged and equally spaced along the poloidal direction.

In order to better understand the results obtained, two different plots are reported below. In particular, Figure 3.17 shows the TBR performances of all the layout

analysed as a function of the reciprocal of the total cross-sectional area of the channels (i.e. $1/Nab$), which is proportional to the water amount inside the FW.

Looking at the results, it is easy to observe that the water amount plays a pivotal role in the increase/decrease of the TBR and, in particular, higher is the water amount higher is the TBR. Such unexpected result goes towards the opposite direction of what observed in [39] and stated also in [43], and further investigations would be needed to get to know which are the modelling assumptions (i.e. heterogenous vs. homogeneous model and elementary cell vs. whole blanket sector) that make such a difference come out.

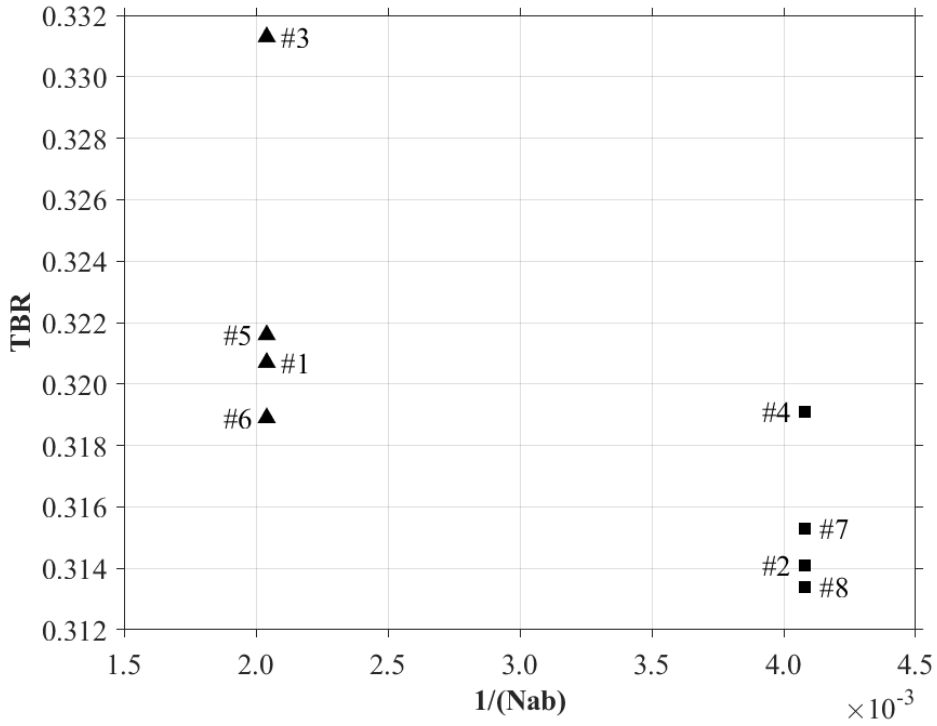

Figure 3.17: TBR vs $1/Nab$.

From Figure 3.17 it was also possible to observe that, for each level of water amount, a certain behaviour exists between different configurations. In particular, it was found that the TBR increases when the quantity $R(Nb)^{\beta}$ decreases, as shown in Figure 3.18.

This last plot shows that the reduction of the parameter R has a positive influence on the tritium breeding, as already noted in [69], as well as the reduction of the poloidal surface occupied by the channels Nb, with a second-order effect though.

In fact, as already stated in [69], both contributes to the reduction of the steel thickness enclosed between the channels and the BZ, wherein lots of neutron are captured after having been moderated by the water.

Combining both the aspects observed in Figures 3.17 and 3.18, a unique scalar function $f(\mathbf{X})$ of the design variable vector $\mathbf{X}$ has been defined by a linear

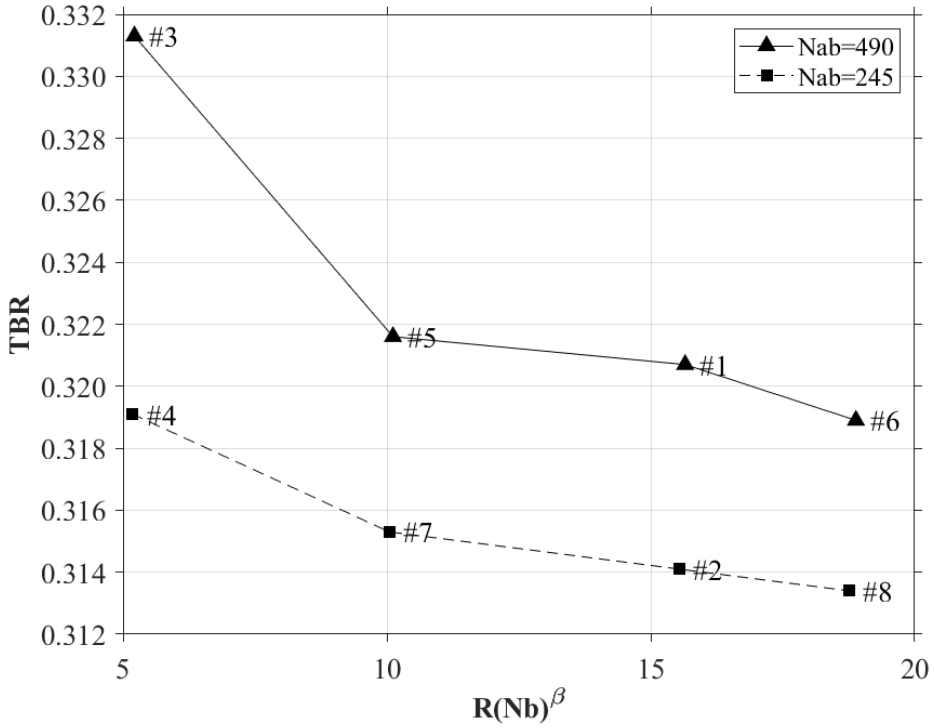

Figure 3.18: TBR vs $R(Nb)^{\beta}$ with β=0.01.

combination between $1/Nab$ and $R(Nb)^{\beta}$ as follow,

$$f(\mathbf{X}) = \frac{1}{Nab} + \gamma R(Nb)^{\beta} \tag{3.27}$$

where β=0.01 and γ=1.75·10^{-4}. In particular, the low value of the coefficient β justifies the weak influence of the factor Nb with respect to R, whereas the coefficient γ combines the two addends of the function. Plotting the TBR obtained vs. the function $f(\mathbf{X})$ (see Figure 3.19), it is possible to observe how the minimization of the latter implies an increase of the TBR.

However, being the function in Equation (3.27) not bijective (i.e. different combinations of the design variable may have the same value of the function), it must be stressed that is not possible to assert that the TBR is function of $f(\mathbf{X})$. Indeed, two different vectors $\mathbf{X}_i$ and $\mathbf{X}_j$ might have the same value of the function $f(\mathbf{X})$, but show different values of TBR. In math formulation,

$$f(\mathbf{X}_i) = f(\mathbf{X}_j) \implies TBR(\mathbf{X}_i) = TBR(\mathbf{X}_j) \tag{3.28}$$

According to that, before implementing the function in Equation (3.27) as the objective function to be minimized in our multiphysics optimization framework, its goodness has been also tested with other four different cases (see Table 3.7) to verify if it is at least sufficiently monotonic in the interval of interest for the problem's purposes.

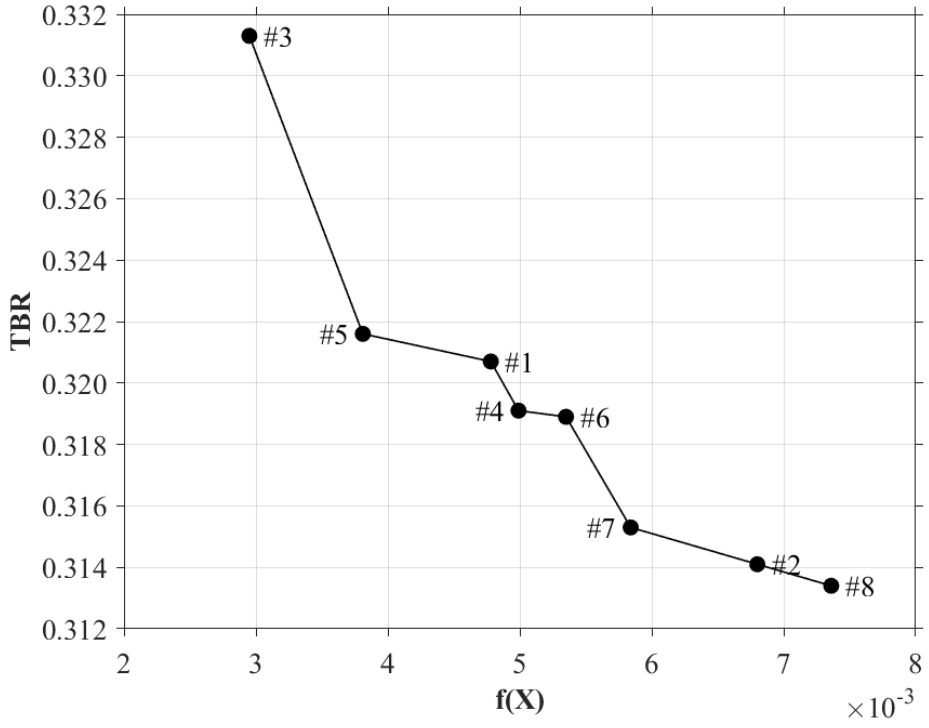

Figure 3.19: TBR vs $f(\mathbf{X})$.

Configuration	**N** [-]	**R** [mm]	**a** [mm]	**b** [mm]	**TBR** [-]
#9	10	8	14	7	3.395E-01
#10	5	6.75	15	5.4	3.222E-01
#11	5	13	7	7	3.149E-01
#12	5	5.3	13.8	20.8	3.621E-01

Table 3.7: Additional cases analysed with TBR results.

The same plot as in Figure 3.19 has been reported in Figure 3.20 with the addition of the four more cases analysed.

As expected, the four additional configurations analysed confirmed the trend already outlined by the first eight simulations, without showing any inversion of concavity. Furthermore, even though $f(\mathbf{X})$ is not bijective, it can be agreed that combinations of parameters having similar values of the objective function, show also similar values of TBR.

Finally, as already stated above, such heuristic approach has been used to obtain, without performing hundreds of MCNP calculations, an acceptable objective function to be easily implemented in such multiphysics optimization framework in order to increase the tritium breeding performances in the equatorial cell of the WCLL COB segment. Moreover, having been confirmed by neutron transport calculations, the function in Equation (3.27) might represent a good starting point for further studies in the development of a general function $TBR(\mathbf{X})$.

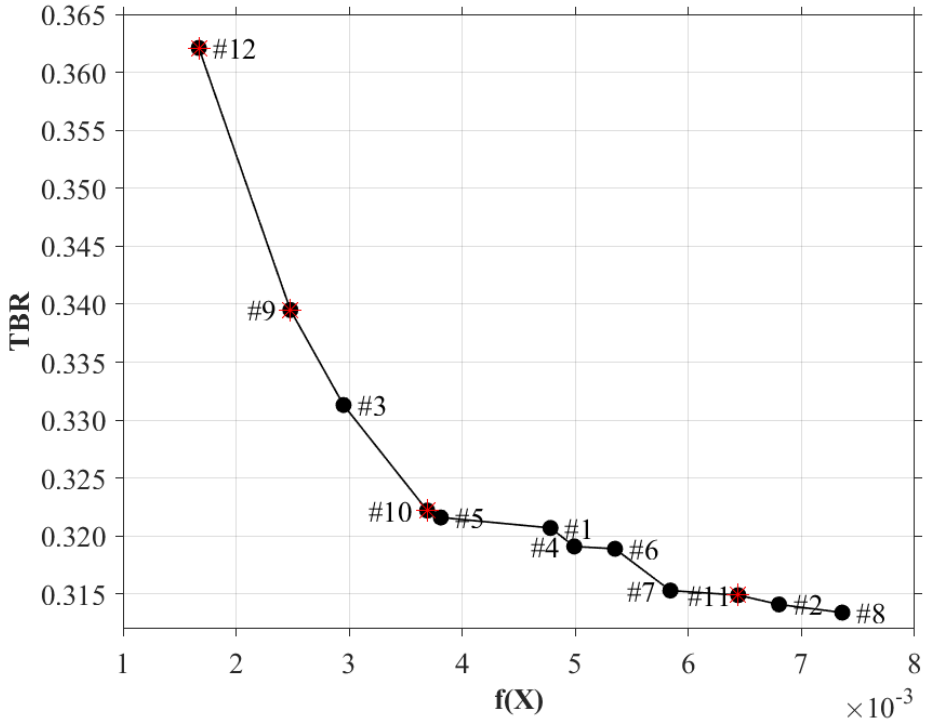

Figure 3.20: TBR vs $f(\mathbf{X})$ with additional points analysed (marked in red).

Constraints Definition

As far as the constraints are concerned, their definition had to deal with different aspects of a water-cooled breeding blanket design. In particular, as already described in Chapter 2, two different types of constraints had to be defined: (1) the *side constraints*, that are the limits of the design variables, and (2) the *functional constraints*, depending upon the performances and the prescribed requirements.

The design variable limits have been defined relying on the recent experiences in the WCLL BB design [13][16] as well as on rational assumptions. In particular, the following intervals have been adopted for the design variables N, R, a and b during the optimization process:

$$N \in [4\,;\,10] \subset \mathbb{N} \tag{3.29}$$

$$R \in [s\,;\,t_{FW} - 3s] \subset \mathbb{R} \tag{3.30}$$

$$a \in [2s\,;\,t_{FW} - R - s] \subset \mathbb{R} \tag{3.31}$$

$$b \in [2s\,;\,(H - Ns)/N] \subset \mathbb{R} \tag{3.32}$$

where s=2 mm, assumed as the minimum thickness of any section in the FW domain, t_{FW}=25 mm, that is the FW thickness as reported in Table 3.1, and H=135 mm, that is the poloidal height of the elementary cell as reported in Table 3.1. Concerning the channel dimensions a and b, a lower limit of 4 mm has been imposed to both dimensions, whereas the upper limits depend on the values of the R and N,

respectively. Moreover, it must be stressed that all the design variables belong to the set of real numbers, with the except of N that clearly must be natural.

As to the functional constraints, since the main nuclear requirement (i.e. the TBR) has been considered during the objective function definition, only thermal-hydraulic and structural requirements have been imposed for the FW optimization. In particular, considering the coarseness of the numerical model used for the optimization, not all of the requirements presented above have been implemented, but the ones identified as the most critical for our purposes.

Regarding the thermal-hydraulic constraints, limitations on coolant maximum velocity as well as on maximum or minimum temperature in the structure have been implemented:

$$u_{FW} \leq 7 \text{ m/s} \tag{3.33}$$

$$T_{Eurofer,max} \leq 550 \text{ °C} \tag{3.34}$$

$$T_{SLi,ave} \geq 350 \text{ °C} \tag{3.35}$$

where u_{FW} is the average coolant velocity in the FW cooling channels, $T_{Eurofer,max}$ is the maximum temperature reached in the Eurofer97 domain (with the except of the Baffle Plate which does not play any structural role), and $T_{SLi,ave}$ is the average temperature on the supporting line SL_i. As to the latter, those limits have been imposed due to DBTT considerations as shown in Figure 1.14 and stated also in [22].

From the structural point of view, constraints on the verification of some of the RCC-MRx design criteria have been imposed:

$$(\overline{P_m})_{SLi,A} \leq S_{m,A}(T_{SLi,ave}) \tag{3.36}$$

$$(\overline{P_L + P_b})_{SLi,A} \leq 1.5 S_{m,A}(T_{SLi,ave}) \tag{3.37}$$

$$(\overline{P_m + Q_m})_{SLi,A} \leq S_{em,A}(T_{SLi,ave}) \tag{3.38}$$

$$(\Omega\overline{P_m})_{SLi,A} \leq S_t(T_{SLi,ave}, t{=}18000\text{h}) \qquad \text{if } T_{SLi,ave} \geq 450 \text{ °C} \tag{3.39}$$

$$(\overline{P_L + \Phi P_b})_{SLi,A} \leq S_t(T_{SLi,ave}, t{=}18000\text{h}) \qquad \text{if } T_{SLi,ave} \geq 450 \text{ °C} \tag{3.40}$$

$$(\max\left[\overline{P_L + P_b}\right] + \overline{\Delta Q})_{SLi,A} \leq 3 S_{m,A}(T_{SLi,ave}) \tag{3.41}$$

$$(\overline{P_m})_{SLi,D} \leq S_{m,D}(T_{SLi,ave}) \tag{3.42}$$

$$(\overline{P_L + P_b})_{SLi,D} \leq 1.5 S_{m,D}(T_{SLi,ave}) \tag{3.43}$$

$$(\overline{P_m + Q_m})_{SLi,D} \leq S_{em,D}(T_{SLi,ave}) \tag{3.44}$$

where the symbols are the same as the ones presented above. In particular, for creep failure considerations, an activation temperature of 450 °C has been set as lower limit, mainly due to lack of data at lower temperatures, and an operating

time of 18000 h (≈2 fpy) has been assumed for the blanket. As to the verification against ratcheting failure mode, $\overline{\Delta Q}$ has been conservatively approximated to $\overline{Q}$, having been considered only one steady-state thermal analysis.

The entire stress linearization procedure carried out along the whole set of supporting lines has been performed by means of a proper MATLAB script linked to COMSOL. In order to simplify the architecture of the optimization process, all the criteria presented-above have been condensed into a single one, as follow

$$\max(uf_{SLi,j}) \leq \frac{1}{n} \tag{3.45}$$

where $uf_{SLi,j}$ is the *utilization factor* (i.e. the ratio of the equivalent stress to the allowable stress) in the supporting line SLi considering the j^{th}-criterion among the one reported in Equations (3.36) to (3.44). Moreover, a small safety margin n (=1.05) has been added to take into account uncertainties on temperature distribution, which in turn depends upon the nuclear heating.

Remaining criteria that were not considered during the optimization process have been verified directly into the optimized layout of the equatorial cell, analysed in Chapter 4 considering its specific nuclear heating profiles.

3.3.3 Results of the Optimization Campaign

The optimization campaign has been carried out relying on the Complex method presented in Chapter 2 and implemented in a MATLAB script able to link with the COMSOL FE model for the evaluation of most of the constraints. The MATLAB script used for the FW optimization is reported in Appendix B.

As already stated in Chapter 2, the definition of the initial complex requires that the first point $\mathbf{X}_1$ must be feasible. According to that, the choice of the first point fell on the reference FW channels layout in the equatorial region of the COB segment [39], which is featured by N=6, R=15 mm, a=7 mm and b=7 mm.

However, the check on its feasibility resulted in the violation of several thermo-structural constraints, all of them concerning the minimum average temperature in the main thicknesses of the FW, as in Equation (3.35). In particular, the average temperature in lines SL3, SL6, SL7, SL8 and SL10 (see Figure 3.12) was below 350 °C. If reducing R from 15 to 14 mm was sufficient to satisfy the requirement in lines SL3, SL6 and SL10, no feasible actions were identified to make the average temperature between two consecutive channels (SL7 and SL8) higher than 350 °C.

With the aim of finding other feasible points that fulfill all the prescribed requirements, lots of configurations have been analysed but none of them was able to satisfy contextually all the constraints inherent to either stress limits and minimum irradiation temperature due to DBTT positive shifts effects.

Nevertheless, being non-productive to relax the constraint to a lower temperature (see Figure 1.14), it has been decided to remove such temperature constraint from the thicknesses along the lines SL7 and SL8. In fact, the eventual crack nucleation and propagation along the thickness separating two water channels can be considered as less relevant than along thicknesses separating the coolant from other environments (i.e. BZ, plasma chamber). Furthermore, a temperature constraint in the thickness between channels is somehow considered in the minimum allowable average temperature along the lines SL1 and SL4.

Despite that, irradiation embrittlement in the material very close to the water cooling channels will definitely occur and, if not properly tackled, such phenomenon might cause gross failure of the FW. Hence, it is important to underline how much further R&D activities on fusion reactor materials is still needed, so to allow the designers to conceive feasible, reliable and performing components.

Once the first feasible point was identified, the initial complex $\mathbf{X}_{start}$, defined as an array with n=4 columns by k=2n rows, wherein each row (N, R, a, b) represents a point of the complex, has been randomly determined by means of Equation (2.1). If some point violates any of the functional constraints, it is adjusted according to Step 1 in Section 2.4.1 before starting the reflection process.

Since the Complex method is intrinsically unable to recognize a local minimum from the global minimum of a function, good rationale to investigate more deeply the feasible n-dimensional space is to run more than a single optimization analysis and compare the final results obtained. According to that, five simulations have been carried out for the optimization of the FW cooling channels (each one starting with a different initial complex), and the results are reported in Tables 3.8 to 3.10.

As already adopted in Chapter 2, the procedure made of sequential reflections and shaping of the complex to reach the minimum of the objective function (while complying with the constraints) is shown in the Figures 3.21 and 3.22. The former reports in a log-log graph the objective function value at the centroid of the complex $f(\mathbf{X}_0)$ vs. the number of reflections completed, while the latter reports in a log-log graph the standard deviation value of the complex σ as defined in Equation (2.7) vs. the number of reflections completed.

In order to make both calculation and visualization easier, the objective function $f(\mathbf{X})$ has been scaled with a multiplication factor of $1 \cdot 10^3$, so to obtain values in the order of the unity. In fact, such operation does not modify the outcome of an optimization process [45]. As a consequence of that operation, the minimum threshold ε, as defined in Equation (2.7), has been set to $1 \cdot 10^{-2}$, in order to have a deviation between the objective function value at each point and the value at the centroid lower than $1{\cdot}10^{-1}$ on average.

Run	$\mathbf{X}_{start}$	$f(\mathbf{X}_{start})$	$\mathbf{X}_{end}$	$f(\mathbf{X}_{end})$	Reflections	σ
#1	$\begin{pmatrix} 6 & 14.000 & 7.000 & 7.000 \\ 6 & 12.087 & 5.697 & 13.378 \\ 6 & 10.156 & 8.895 & 12.587 \\ 7 & 10.316 & 9.106 & 9.774 \\ 6 & 9.705 & 9.458 & 11.122 \\ 5 & 9.163 & 7.237 & 8.194 \\ 6 & 13.486 & 6.438 & 9.567 \\ 6 & 14.300 & 6.145 & 10.721 \end{pmatrix}$	$\begin{pmatrix} 5.945 \\ 4.397 \\ 3.344 \\ 3.488 \\ 3.356 \\ 5.037 \\ 5.164 \\ 5.139 \end{pmatrix}$	$\begin{pmatrix} 6 & 6.898 & 12.296 & 17.027 \\ 6 & 6.824 & 12.304 & 17.059 \\ 6 & 6.887 & 12.162 & 17.323 \\ 6 & 6.798 & 12.379 & 17.027 \\ 6 & 6.836 & 12.319 & 16.956 \\ 6 & 6.851 & 12.340 & 17.019 \\ 6 & 6.852 & 12.196 & 17.040 \\ 6 & 6.778 & 12.402 & 16.884 \end{pmatrix}$	$\begin{pmatrix} 2.060 \\ 2.045 \\ 2.054 \\ 2.037 \\ 2.051 \\ 2.049 \\ 2.058 \\ 2.038 \end{pmatrix}$	49	$8.046 \cdot 10^{-3}$
#2	$\begin{pmatrix} 6 & 14.000 & 7.000 & 7.000 \\ 6 & 14.013 & 6.993 & 6.999 \\ 6 & 11.176 & 7.268 & 6.281 \\ 7 & 9.057 & 11.442 & 6.017 \\ 5 & 13.596 & 6.315 & 18.846 \\ 6 & 13.420 & 7.863 & 11.435 \\ 7 & 9.796 & 7.580 & 9.744 \\ 6 & 13.468 & 6.939 & 11.020 \end{pmatrix}$	$\begin{pmatrix} 5.945 \\ 5.951 \\ 5.679 \\ 3.720 \\ 4.171 \\ 4.304 \\ 3.722 \\ 4.637 \end{pmatrix}$	$\begin{pmatrix} 5 & 6.242 & 15.081 & 14.680 \\ 5 & 6.052 & 15.063 & 13.961 \\ 5 & 6.189 & 15.214 & 14.065 \\ 5 & 6.158 & 15.127 & 13.890 \\ 5 & 6.113 & 15.021 & 14.095 \\ 5 & 6.254 & 15.210 & 14.338 \\ 5 & 6.160 & 15.239 & 13.873 \\ 5 & 6.236 & 15.118 & 14.179 \end{pmatrix}$	$\begin{pmatrix} 2.044 \\ 2.056 \\ 2.065 \\ 2.076 \\ 2.061 \\ 2.059 \\ 2.071 \\ 2.072 \end{pmatrix}$	59	$9.705 \cdot 10^{-3}$

Table 3.8: Results obtained (Run #1 and Run #2) using the Complex method as implemented in Appendix B to solve the WCLL BB FW optimization.

Run	$\mathbf{X}_{start}$	$f(\mathbf{X}_{start})$	$\mathbf{X}_{end}$	$f(\mathbf{X}_{end})$	Reflections	σ
#3	$\begin{pmatrix} 6 & 14.000 & 7.000 & 7.000 \\ 5 & 6.578 & 14.527 & 12.805 \\ 8 & 9.531 & 8.777 & 6.392 \\ 5 & 8.906 & 10.097 & 6.387 \\ 7 & 9.153 & 11.437 & 9.664 \\ 7 & 11.702 & 8.983 & 9.751 \\ 9 & 10.241 & 5.287 & 9.366 \\ 7 & 12.254 & 8.088 & 10.620 \end{pmatrix}$	$\begin{pmatrix} 5.945 \\ 2.275 \\ 3.963 \\ 4.715 \\ 2.963 \\ 3.767 \\ 4.117 \\ 3.902 \end{pmatrix}$	$\begin{pmatrix} 5 & 6.310 & 15.147 & 14.481 \\ 5 & 6.277 & 15.178 & 13.951 \\ 5 & 6.130 & 15.405 & 13.390 \\ 5 & 6.180 & 15.340 & 13.663 \\ 5 & 6.284 & 15.251 & 14.122 \\ 5 & 6.231 & 15.284 & 13.697 \\ 5 & 6.360 & 15.079 & 14.432 \\ 5 & 6.232 & 15.459 & 13.557 \end{pmatrix}$	$\begin{pmatrix} 2.064 \\ 2.091 \\ 2.088 \\ 2.082 \\ 2.076 \\ 2.093 \\ 2.081 \\ 2.092 \end{pmatrix}$	26	$9.122 \cdot 10^{-3}$
#4	$\begin{pmatrix} 6 & 14.000 & 7.000 & 7.000 \\ 7 & 11.218 & 10.170 & 6.782 \\ 7 & 10.467 & 10.248 & 7.732 \\ 5 & 11.362 & 5.821 & 22.833 \\ 6 & 12.608 & 8.748 & 8.780 \\ 7 & 9.656 & 10.353 & 9.306 \\ 5 & 10.626 & 7.547 & 13.069 \\ 7 & 12.891 & 7.838 & 10.745 \end{pmatrix}$	$\begin{pmatrix} 5.945 \\ 4.112 \\ 3.709 \\ 3.590 \\ 4.465 \\ 3.245 \\ 3.967 \\ 4.052 \end{pmatrix}$	$\begin{pmatrix} 8 & 8.054 & 9.537 & 12.800 \\ 8 & 8.048 & 9.523 & 12.904 \\ 8 & 8.080 & 9.704 & 13.024 \\ 8 & 8.027 & 9.699 & 12.750 \\ 8 & 8.031 & 9.684 & 12.810 \\ 8 & 8.065 & 9.523 & 13.014 \\ 8 & 8.011 & 9.769 & 12.737 \\ 8 & 8.043 & 9.588 & 12.780 \end{pmatrix}$	$\begin{pmatrix} 2.500 \\ 2.492 \\ 2.470 \\ 2.482 \\ 2.480 \\ 2.487 \\ 2.473 \\ 2.494 \end{pmatrix}$	37	$9.835 \cdot 10^{-3}$

Table 3.9: Results obtained (Run #3 and Run #4) using the Complex method as implemented in Appendix B to solve the WCLL BB FW optimization.

Run	$\mathbf{X}_{start}$	$f(\mathbf{X}_{start})$	$\mathbf{X}_{end}$	$f(\mathbf{X}_{end})$	Reflections	σ
#5	$\begin{pmatrix} 6 & 14.000 & 7.000 & 7.000 \\ 8 & 11.553 & 6.405 & 6.795 \\ 6 & 11.569 & 5.717 & 8.790 \\ 8 & 9.615 & 8.323 & 9.927 \\ 7 & 10.422 & 6.638 & 9.725 \\ 10 & 15.341 & 4.575 & 8.458 \\ 7 & 12.286 & 7.591 & 9.880 \\ 5 & 12.719 & 4.165 & 11.903 \end{pmatrix}$	$\begin{pmatrix} 5.945 \\ 4.977 \\ 5.423 \\ 3.271 \\ 4.115 \\ 5.391 \\ 4.148 \\ 6.353 \end{pmatrix}$	$\begin{pmatrix} 5 & 6.351 & 13.395 & 20.664 \\ 5 & 6.231 & 13.058 & 20.339 \\ 5 & 6.378 & 13.160 & 21.069 \\ 5 & 6.254 & 13.708 & 19.693 \\ 5 & 6.250 & 13.704 & 19.744 \\ 5 & 6.227 & 14.547 & 17.902 \\ \mathbf{5} & \mathbf{6.194} & \mathbf{13.744} & \mathbf{19.497} \\ 5 & 6.399 & 12.840 & 21.624 \end{pmatrix}$	$\begin{pmatrix} 1.887 \\ 1.895 \\ 1.891 \\ 1.887 \\ 1.884 \\ 1.908 \\ \mathbf{1.881} \\ 1.894 \end{pmatrix}$	66	$7.978 \cdot 10^{-3}$

Table 3.10: Results obtained (Run #5) using the Complex method as implemented in Appendix B to solve the WCLL BB FW optimization. The optimum point obtained is highlighted in bold.

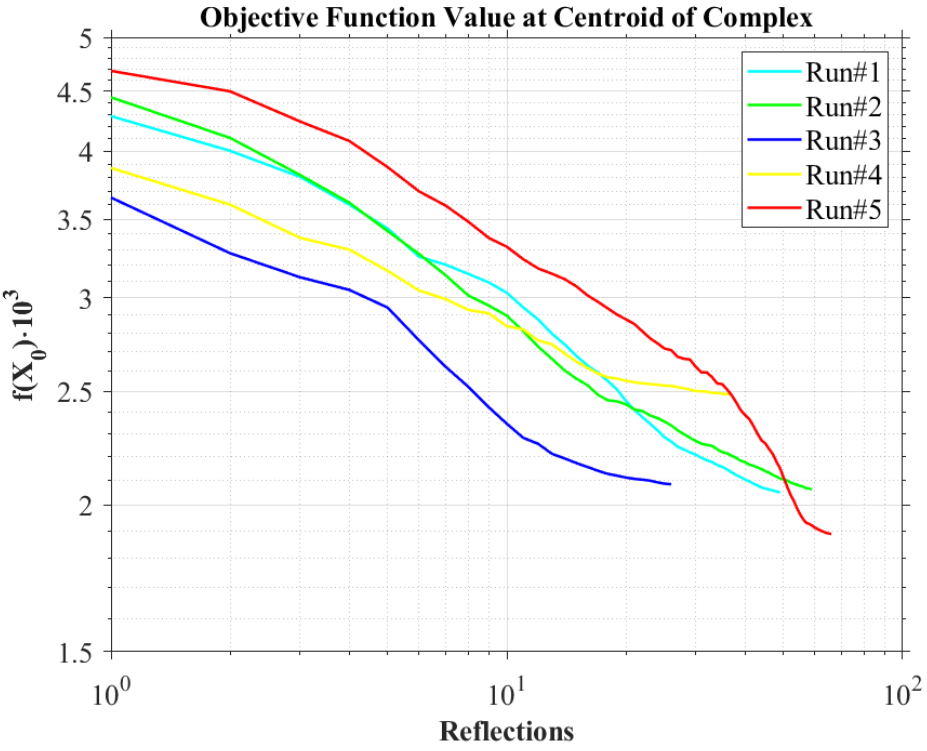

Figure 3.21: Objective function value at centroid vs. number of reflections.

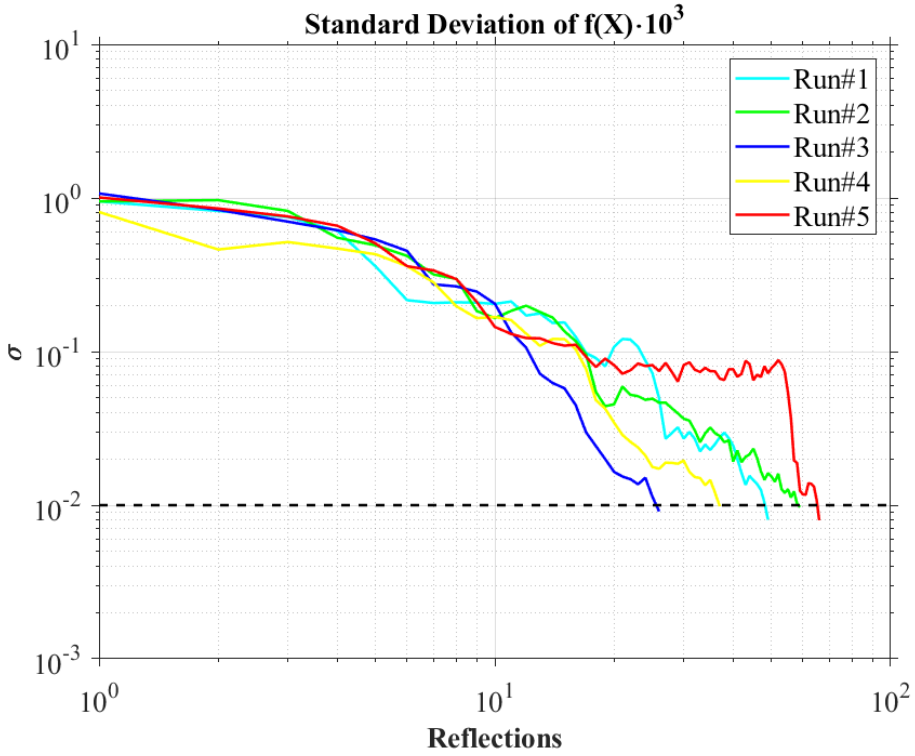

Figure 3.22: Standard deviation of $f(\mathbf{X})$ vs. number of reflections.

The final results show that around 25÷65 reflections are necessary to get the standard deviation σ lower than $1{\cdot}10^{-2}$, depending upon the initial complex and

that little of randomness acting during the optimization process. However, similar values of the objective function have been reached at the end of the five runs, even if obtained with different combinations of variables. In particular, Runs #1, #2 and #3 ended almost to the same objective function value (2.04÷2.09), although the first run got that value with a different variables combination. Hence, the results of the first three runs said that, considering all the constraints, a potential global minimum of the objective function is located around those values.

Conversely, Run #4 finished with a higher objective function value, meaning that the complex got stuck in a local minimum and could not proceed towards the global one. As stated above, this event can happen using the Complex method when lots of constraints are imposed.

Finally, the fifth run ended almost with the same combination of variables of Runs #2 and #3 (i.e. N=5, R≈6.2 mm), but was able to reach a lower value of the objective function (≈1.90) by means of a slightly different combination of the channels' dimension a and b.

The optimum point, thus, is the one highlighted in bold in Table 3.10 with an objective function value of 1.881 and featured by N=5, R=6.194 mm, a=13.744 mm and b=19.497 mm.

Although the final multiphysics assessment of the optimized design of the WCLL COB equatorial cell is treated in Chapter 4, some results obtained at the end of the optimization process in terms of constraints evaluation and temperature/stress field in the picked configuration have been reported for interested readers in Appendix C.

To conclude, using the Complex method has speed up a lot the identification of an optimized FW channels layout, mainly thanks to the capability of such method to manage easily four variables as well as deal with a large number of constraints, working then in *narrow* feasible regions. However, some observations concerning the adoption of this method for the FW optimization have to be reported. Firstly, the high number of constraints might have increased the probability to get the complex stuck in a local minimum, impeding it to *move out* from there looking to better points. Secondly, handling a natural number as N has forced to insert a round operation after every reflection or adjustment of a point. Although this aspect would need to be further investigated, it can be agreed that the round operation could have a small impact on the movement of the complex during the optimization.

Chapter 4

Multiphysics Assessment of the WCLL COB Equatorial Cell Equipped with the Optimized FW

4.1 Introduction

In this last chapter, a more detailed multiphysics assessment of the WCLL COB equatorial cell equipped with an optimized FW channels layout is reported. As obtained at the end of the optimization campaign presented in the previous chapter, the selected optimized layout of FW cooling channels is featured by N=5, R=6.194 mm, a=13.744 mm and b=19.497 mm.

Since such tolerances are not significant for manufacturing such kind of component, the dimensions in the final layout have been approximated so to give more reasonable values as follow: N=5, R=6.2 mm, a=13.7 mm and b=19.5 mm.

The first section of the chapter regards to the preliminary nuclear analysis performed to evaluate the TBR performances as well as the specific nuclear heating profiles to be adopted for the thermo-mechanical analysis.

Secondly, a more detailed thermo-mechanical analysis of the equatorial cell is carried out, evaluating its global thermal-hydraulic parameters as well as the temperature distribution in the several domains. The latter is, then, used together with pressure loads to perform the mechanical analyses and compute the primary, secondary and primary plus secondary stress distributions arising within the structural domain in both NO and OP loading scenarios.

Finally, the enhanced elastic approach as per RCC-MRx is applied to carry out the structural integrity assessment of the component, focusing the attention on the FW domain, and evaluating strengths and weaknesses of the optimized design against the most relevant failure modes for nuclear irradiated components.

4.2 Nuclear Analysis

Following the same approach as during the definition of the objective function, the TBR performances of the optimized concept has been evaluated by a numerical approach based on the Monte Carlo method, adopting the MCNP5.1.6 code [74] along with the JEFF3.2 cross section libraries [75]. A fully heterogeneous 3D MCNP model of the optimized equatorial slice has been set up (see Figure 4.1), and the same planar neutron source and boundary conditions as those adopted for the definition of the objective function have been applied.

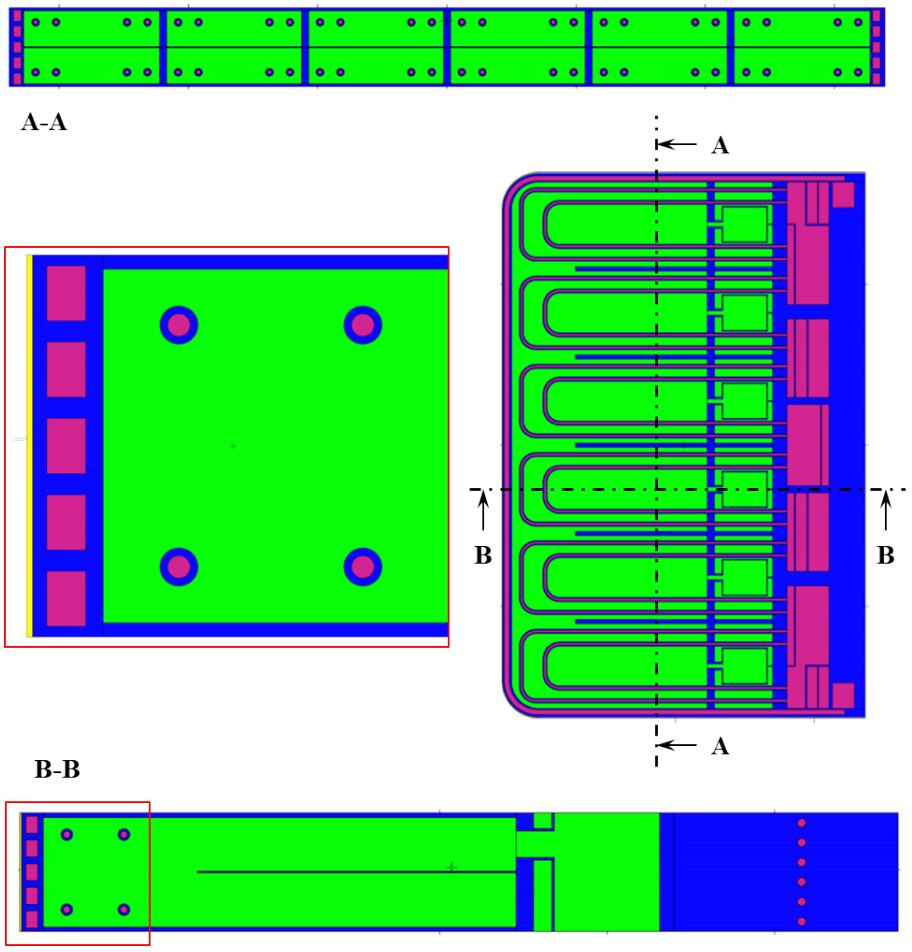

Figure 4.1: 3D fully heterogeneous model of the WCLL COB equatorial cell equipped with the optimized FW.

The analyses have been carried out by simulating a large number of histories ($\sim 10^{10}$) so that the results obtained are affected by relative errors lower than 1% even in the slice regions more distant from the source.

The nuclear response of the equatorial cell has been investigated focusing the attention onto the TBR performances as well as onto the neutronic and photonic deposited power. As far as the tritium breeding performances are concerned, the global evaluation of the tritium produced by means of the reactions in Equations (1.1) and (1.2) has been computed and equal to 0.3558. Plotting this

result inside the graph of Figure 3.20, it is still in good agreement with the definition of the objective function $f(\mathbf{X})$ (see Figure 4.2).

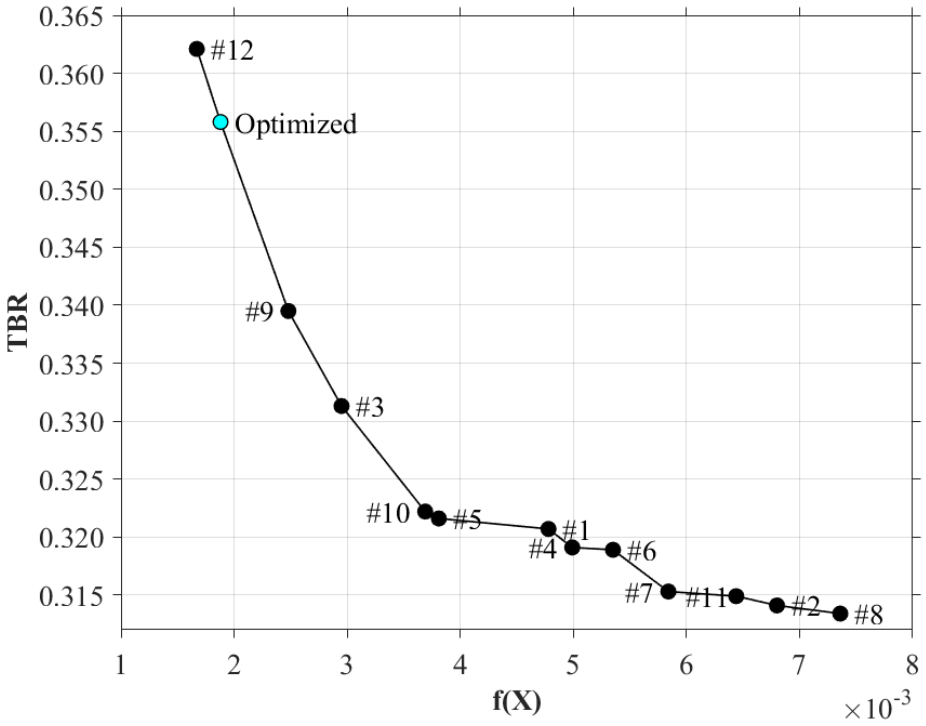

Figure 4.2: TBR performances of the optimized layout.

The results show also a very positive increment of the TBR thanks to the optimized layout with respect to the cases #1 (+10.95%) and #2 (+13.28%), that can be considered as reference values being the number of FW channels varying from 4 to 10 poloidally along the COB segment while keeping R=15 mm, a=7 mm and b=7 mm. Together with the TBR, the power deposited in the module by neutrons and photons has been evaluated in order to provide useful data for the investigation of the thermal–hydraulic performances of the WCLL COB equatorial cell. It has been estimated that a total power of 282.53 kW is released within the equatorial cell and a detailed description of its distribution is reported in Table 4.1.

As shown in the table, more than 2/3 of the total power is deposited in the PbLi contained within the BZ, while the most relevant fraction of the nuclear heating in the structure is obtained in the complex of FW-SWs.

The spatial distribution of the deposited nuclear power volumetric density (i.e. nuclear heating), q''', was evaluated to allow the study of the thermo-mechanical performances to be carried out. In particular, its radial profiles were assessed within several sub-domains of the cell, as shown in Figure 4.3.

As expected, the deposited power densities reach their highest values near the plasma-facing region of the segment, both in the SB and the BZ, decreasing significantly along the radial direction.

Domain	**Sub-domain**	**Value** [kW]
Tungsten	W-armour	10.27
Eurofer97	FW + SWs	28.82
	Toroidal-radial SPs	9.70
	Poloidal-radial SPs	1.10
	Baffle plate	0.34
	BP	0.29
	Manifold + BSS	3.80
	DWTs	2.56
PbLi	BZ	196.43
	Manifold	5.98
Water	FW-SWs channels	18.71
	DWTs	3.78
	Manifold	0.76
TOT		282.53

Table 4.1: Neutronic and photonic power deposited in the optimized WCLL COB equatorial cell.

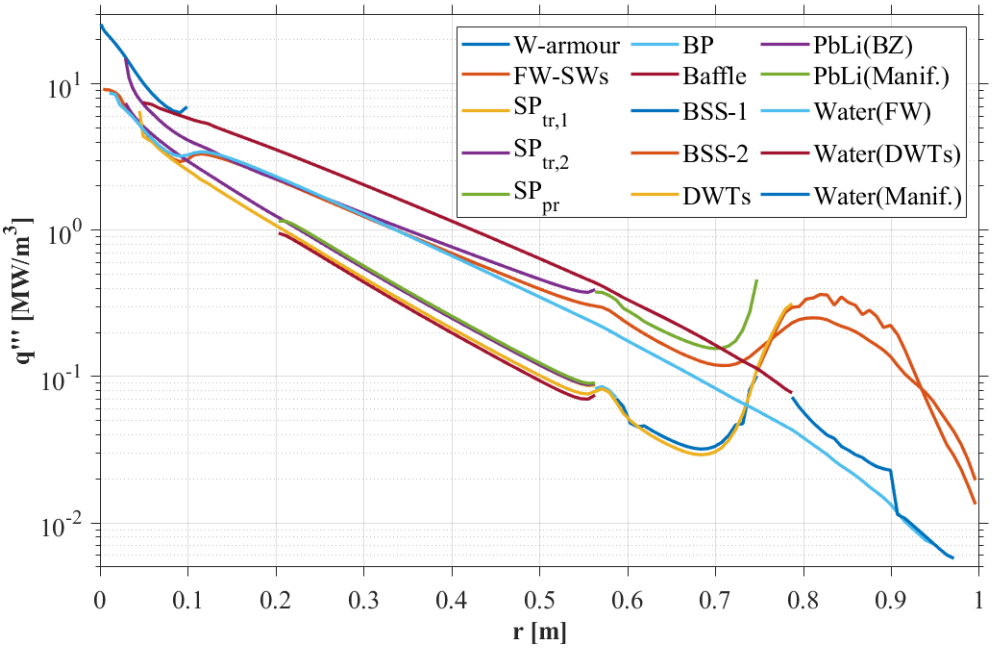

Figure 4.3: Radial profiles of the deposited nuclear power volumetric density q''' in the optimized WCLL COB equatorial cell.

The highest value of around 26 MW/m^3 is reached in the W-armour, which is the layer directly facing the plasma. The average value of nuclear power deposited in the FW is around 8÷9 MW/m^3, in agreement with what calculated in [39][68]. The maximum value of q''' obtained in the breeder is around 14.9 MW/m^3. As to the water, a significant fraction of about 8.2% of the total power is deposited on it,

also due to the increment of the water amount that came out from the optimization campaign. Finally, it is worth to notice the appearance of peaks and, more general, of increased values in the rear region of the cell, probably due to *back-scattering* of the neutrons in those regions induced by the significant amount of water contained in the manifold close to the BSS. However, such effect involves regions featured by nuclear power density values decreased of almost two order of magnitude with respect to the highest values.

4.3 Thermo-Mechanical Analysis

The thermo-structural assessment of the optimized configuration of the equatorial cell has been carried out adopting the same procedure as the one used for the optimization campaign, but relying on a more detailed numerical model as well as specific loads and boundary conditions.

Firstly, the optimized configuration has been modelled by means of FE model featured by a finer mesh, with particular attention in the FW-SWs domain. The mesh resulted as composed of 415116 nodes connected into 2192699 quadratic tetrahedral elements (see Figures 4.4 and 4.5).

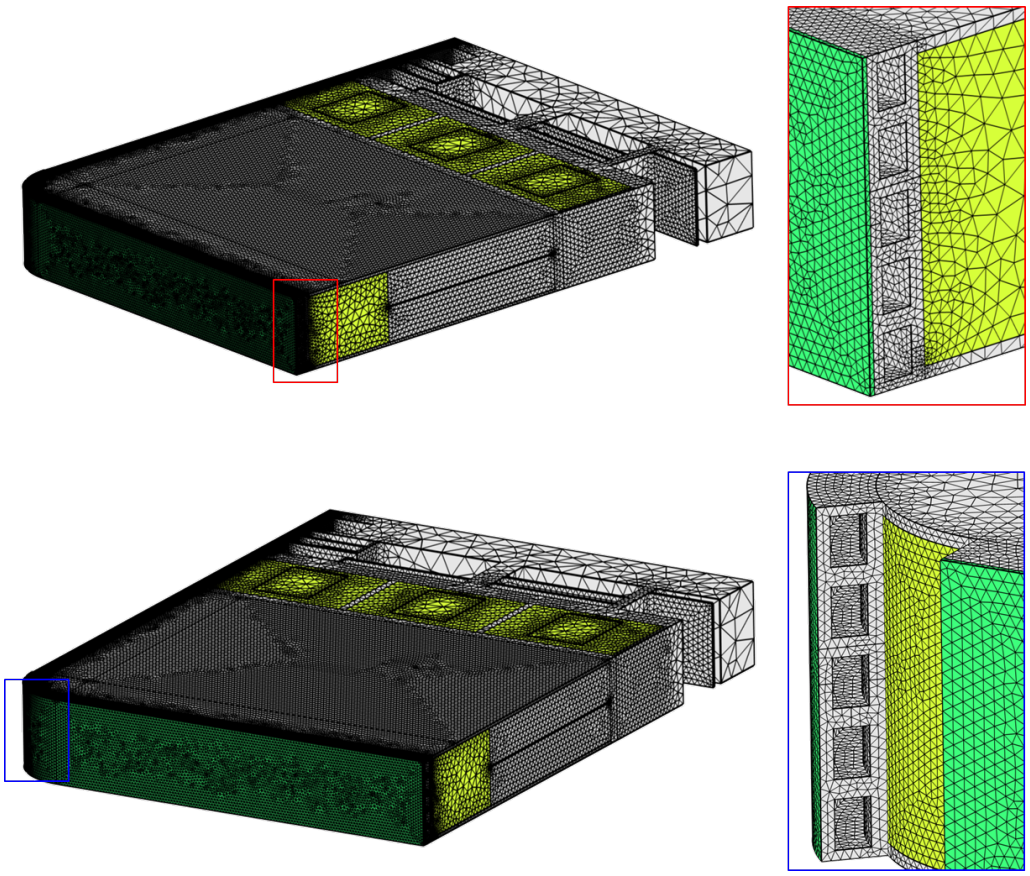

Figure 4.4: Front view of the FE model of the equatorial cell equipped with the optimized FW channels layout.

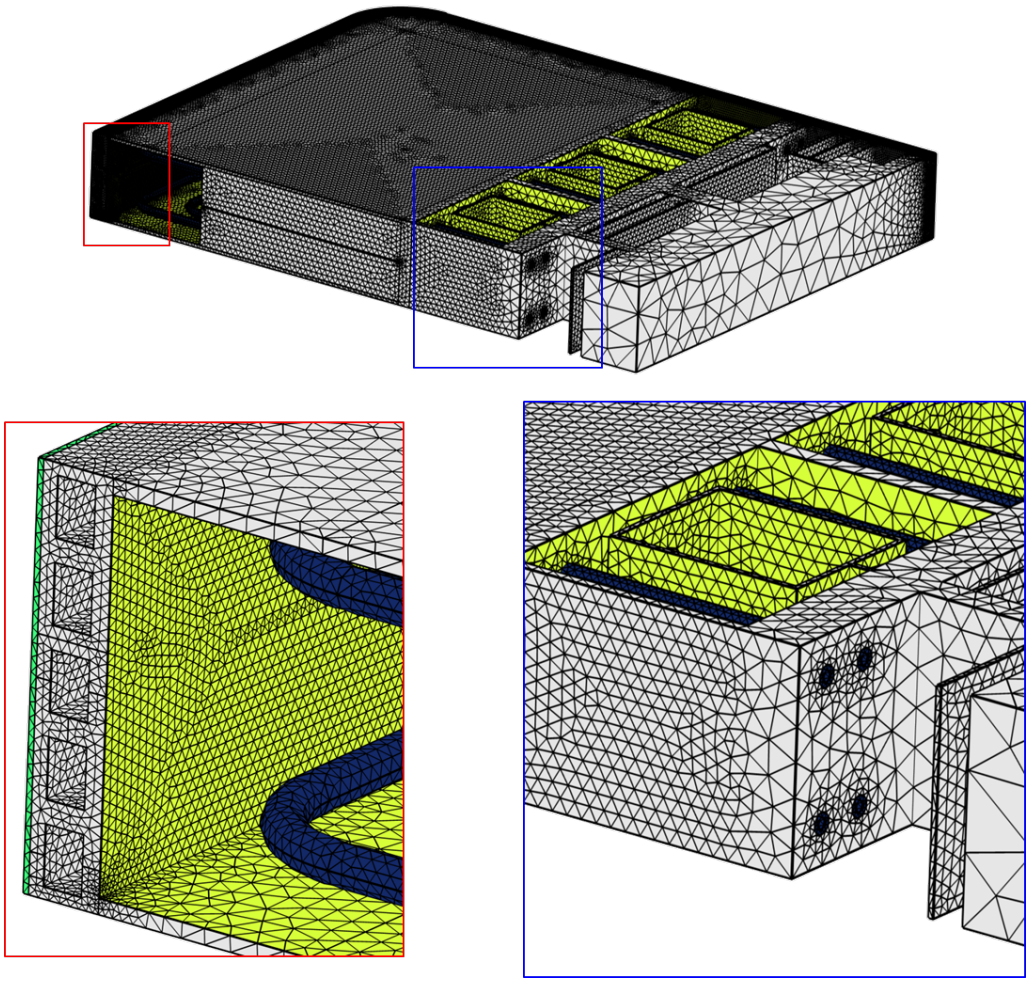

Figure 4.5: Back view of the FE model of the equatorial cell equipped with the optimized FW channels layout (breeder domain not shown).

As to the material properties, the same values used for the optimization campaign have been adopted. Concerning the thermo-mechanical performances of the WCLL BB, the two main relevant steady-state scenarios have been assessed considering again: the Normal Operation and the Over-Pressurization scenarios.

4.3.1 Thermal Analysis

The same kind of thermal loads and boundary conditions used for the optimization campaign have been adopted for the computation of the temperature distribution in the model. Hence, for the heat transfer simulation the following set of loads and boundary conditions pertinent to the steady-state NO scenario have been applied:

- surface heat flux of 0.32 MW/m^2 onto the W-armour plasma facing surface;
- volumetric density of nuclear-deposited heat power q''' [MW/m^3] computed by means of a specific MCNP nuclear analysis;

- forced convective heat transfer at coolant/wall interface;
- pure diffusive heat transfer within the breeder (assumed as stagnant).

According to that, the main difference with respect to the thermal field computed during the optimization analysis is the nuclear heating distribution inside the cell, this time calculated specifically for this geometry as shown in Figure 4.3.

As to the boundary conditions, water domain was not modelled as in the optimization campaign, but its cooling effect on the structure have been simulated by specific convective boundary conditions. In particular, the same iterative procedure described in Section 3.3.1 to calculate the required mass flow rates and the related heat transfer coefficients has been adopted.

The temperature distributions obtained in different domains from a steady-state heat transfer analysis are reported in Figures 4.6 to 4.11.

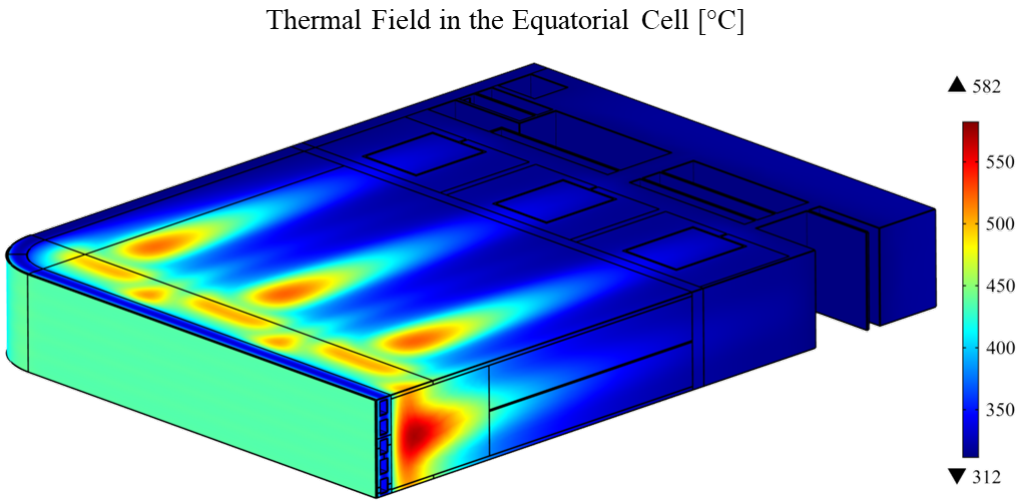

Figure 4.6: Temperature distribution in the equatorial cell.

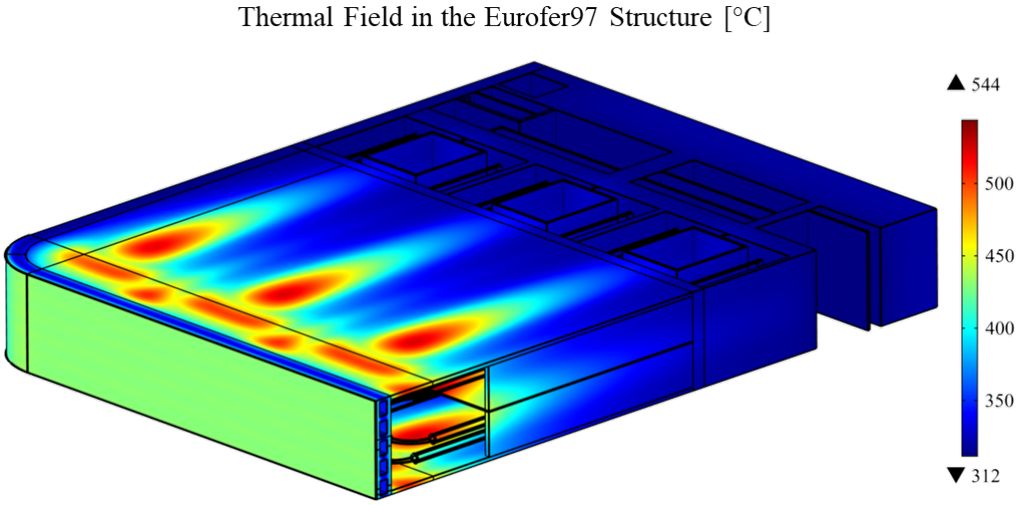

Figure 4.7: Temperature distribution in the Eurofer97 structure.

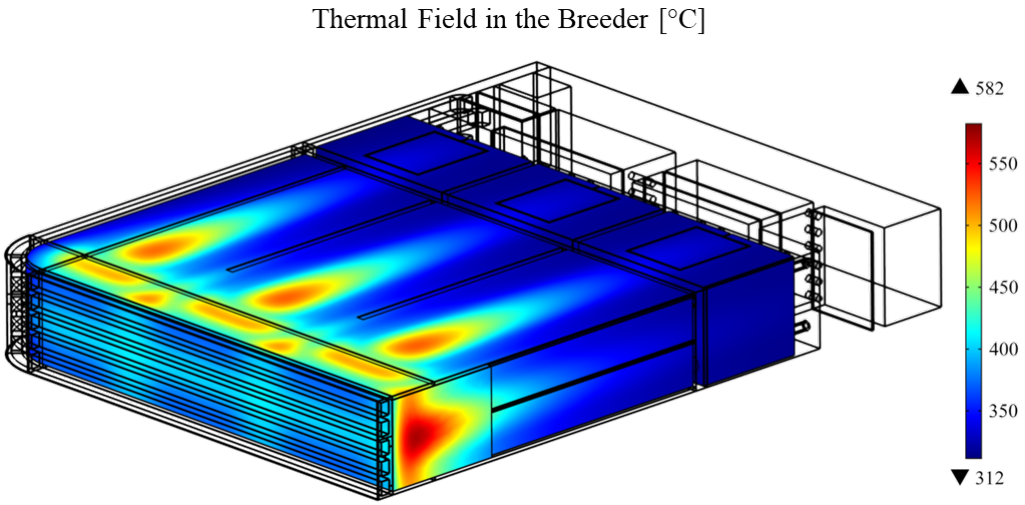

Figure 4.8: Temperature distribution in the breeder.

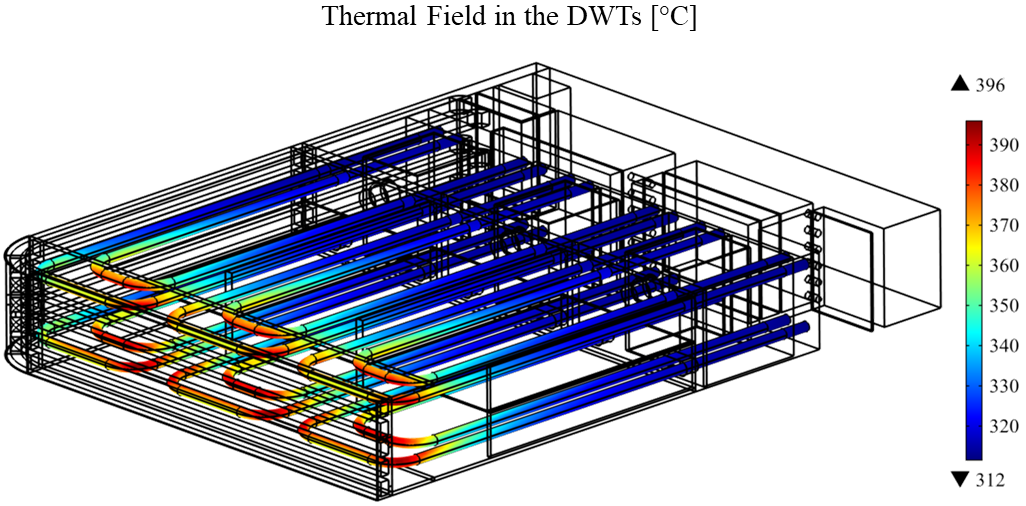

Figure 4.9: Temperature distribution in the DWTs.

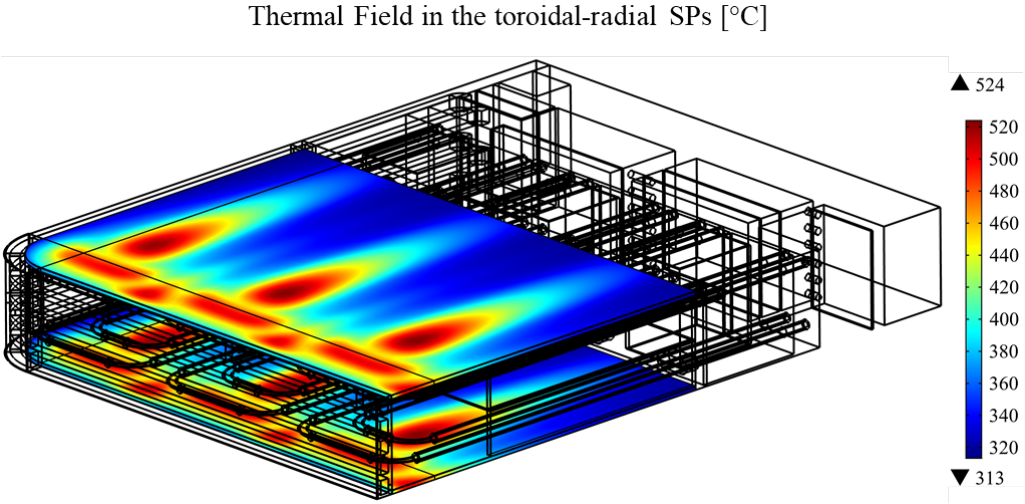

Figure 4.10: Temperature distribution in the toroidal-radial SPs.

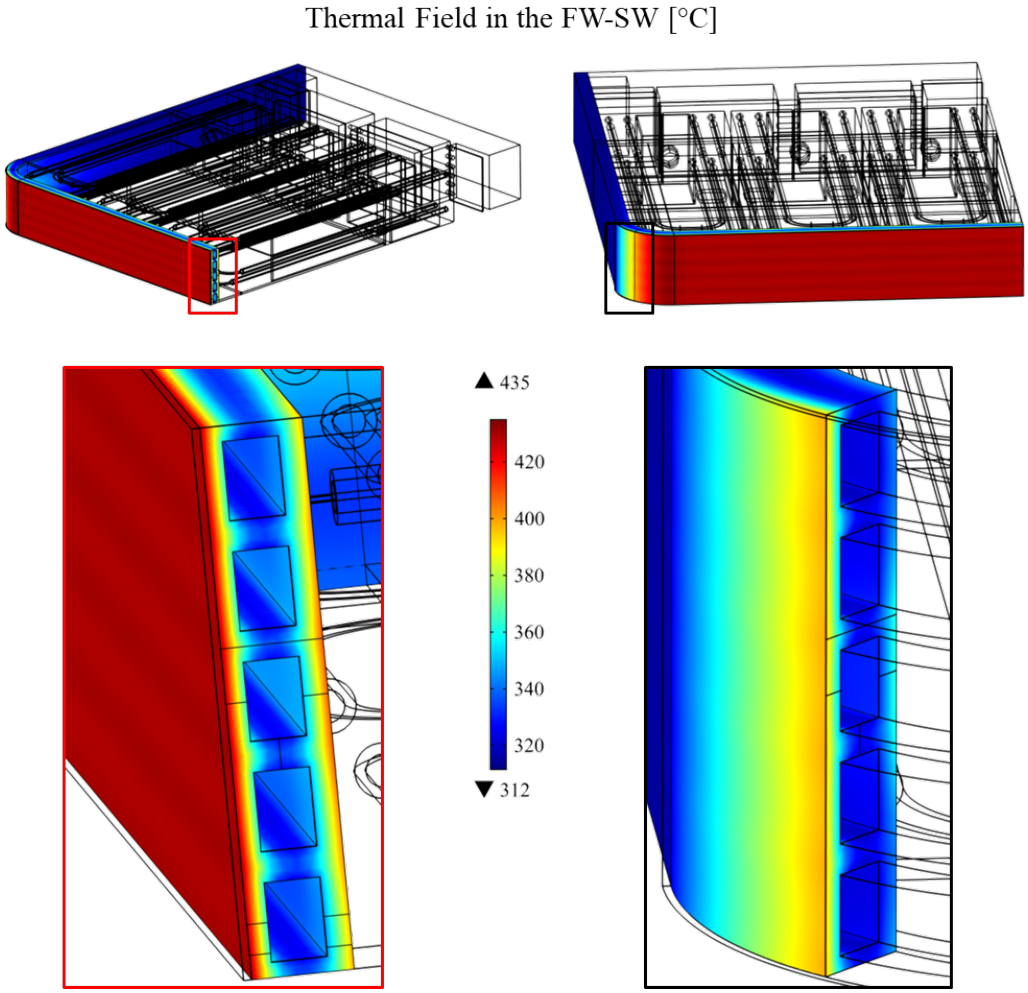

Figure 4.11: Temperature distribution in the complex of FW-SW.

The maximum temperature in the whole equatorial cell is, of course, obtained within the PbLi domain and hits the value of 582 °C. Concerning the highest temperature in the Eurofer97, it is reached in correspondence of the Baffle plate where a value of 544 °C has been computed (see Figure 4.7), slightly below the maximum allowable limit of the material set to 550 °C. However, since the Baffle plate does not contribute to the structural integrity of the component, the maximum temperature to be checked inside the Eurofer domain should be computed taking into account the components actively involved in maintaining the structural integrity of the box, such as the FW, SWs and the SPs (rear parts are not considered because of their lower temperature). According to that, the maximum value of 524 °C is obtained in the toroidal-radial SPs, with a margin of about 25 °C with respect to the Eurofer97 limit value.

As far as the FW-SW complex is concerned, the maximum temperature is around 435 °C in correspondence of the interface with the W-armour, whereas the minimum value is very close to the fluid bulk temperature of 311 °C. A further assessment regarding the implication of the FW temperature distribution to the irradiation

embrittlement of the material is reported in the next sections.

As to the hydraulic performances, the pressure drops in the both circuits have been calculated by using the Darcy-Weisback equation [70],

$$\Delta p = \zeta \frac{\rho u^2}{2}$$

where ρ is the fluid density at the average temperature, u is the average fluid velocity and ζ is the coefficient of fluid resistance. Using the formula reported in [77], the latter can be expressed by the sum of several factors, basically considering distributed pressure losses ζ_d and concentrated pressure losses ζ_c,

$$\zeta = \sum_i \zeta_{d,i} + \sum_j \zeta_{c,j} = \sum_i 4 f_i \frac{L_i}{D_{h,i}} + \sum_j \zeta_{c,j}$$

where i refers to the i^{th}-straight line featured by a Fanning friction factor f_i, a length L_i and a hydraulic diameter $D_{h,i}$, and j refers to the j^{th}-concentrated loss. Considering the different empirical correlations that can be used to calculate the Fanning friction factor, the one developed by Haaland [78] under flow conditions of $4 \cdot 10^4 < Re < 10^7$ when pipes have certain roughness $\epsilon/D_h < 0.05$, has been selected,

$$\frac{1}{\sqrt{f}} = -3.6 \log_{10} \left[\frac{6.9}{Re} + \left(\frac{\epsilon}{D_h} \right)^{\frac{10}{9}} \right]$$

assuming a roughness of the surface ϵ equal to 15μm, which is a conservative value for commercial steel pipes [77].

As to the concentrated losses, 1 and 0.5 have been conservatively assumed as loss coefficients for sudden expansion and contraction of the stream flow, respectively, whereas for the FW and DWTs bends, the following relation has been used [77],

$$\zeta_{c,bend} = 0.0175 \lambda \frac{R_0}{D_h} \delta$$

where R_0 is the bend radius, δ is the angle of the turn and λ is an enhanced friction factor (Darcy-type) depending upon the cross section and the Reynolds number [77]. In particular, being $R_0/D_h > 3$ for both FW channels and DWTs bends, the equation above can be used without the addition of any local resistance coefficient.

The main thermal hydraulic features have been collected in Table 4.2.

Finally, a verification against the phenomenon of DNB, in which the vapour basically insulates the bulk of the liquid from the hot surface making the heat flux dramatically decrease, has been performed. The onset of such phenomenon is caused by a heat flux of a potential boiling systems that reaches the CHF value. Hence, in order to prevent this to happen, it is necessary to compute the so called CHF_{ratio}, which represents a safety margin and can be expressed by the ratio of

Parameter	Description	Value	Unit
$\dot{m}_{FW}$	mass flow rate in FW-SWs cooling circuit	0.8658	kg/s
$\dot{m}_{DWT}$	mass flow rate in DWTs cooling circuit	0.9279	kg/s
$D_{h,FW}$	hydraulic diameter of the FW cooling channel	16.093	mm
$D_{h,DWT}$	hydraulic diameter of the DWT	8	mm
u_{FW}	average coolant velocity in FW-SWs channels	0.923	m/s
u_{DWT}	average coolant velocity in DWTs	3.294	m/s
Re_{FW}	average Reynolds number in FW-SWs channels	124079	-
Re_{DWT}	average Reynolds number in DWTs	220065	-
h_{FW}	heat transfer coefficient in FW-SWs channels	8792	W/(m^2·°C)
h_{DWT}	heat transfer coefficient in DWTs	27973	W/(m^2·°C)
$R_{0,FW}$	bend radius of the FW cooling channels	90.05	mm
$R_{0,DWT}$	bend radius of the DWTs	40.5	mm
L_{FW}	length of a FW channel (no bends)	3.483	m
L_{DWT}	length of a DWTs (no bends)	4.518	m
f_{FW}	Fanning friction factor in FW channels	5.3E-03	-
f_{DWT}	Fanning friction factor in DWTs	5.9E-03	-
λ_{FW}	enhanced Darcy friction factor in FW bends	0.05	-
λ_{DWT}	enhanced Darcy friction factor in DWT bends	0.038	-
ζ_{FW}	overall Darcy coefficient in FW channels	6.99	-
ζ_{DWT}	overall Darcy coefficient in DWTs	19.75	-
Δp_{FW}	pressure drop in FW-SWs cooling circuit	2.09	kPa
Δp_{DWT}	pressure drop in DWTs cooling circuit	75.12	kPa

Table 4.2: Thermal-hydraulic features of the optimized equatorial cell.

the CHF, calculated using specific correlations, to the peak of the heat flux at the wall/coolant interface. Inside the WCLL BB, the maximum heat flux is reached in the FW cooling channels, of course. Using the TONG-75 correlation [62] (as also used for ITER Divertor [79]) developed for light water fission reactors, the Critical Heat Flux [W/m^2] is given by,

$$CHF = 0.23 f G H_{fg} \left(1 + 0.00216 P_r^{1.8} \sqrt{Re} Ja\right) C_f$$

where,

$$f = 8 Re^{-0.6} \left(\frac{D_h}{D_0}\right)^{0.32}$$

$$P_r = \frac{P}{P_c}$$

$$Ja = \frac{\rho_f}{\rho_g} \frac{c_p (T_{sat} - T)}{H_{fg}} \qquad \text{(Jacob number)}$$

with: f is a friction factor; G is the coolant mass velocity [kg/m^{2}s]; T is the local coolant temperature [°C]; P is the local coolant pressure [MPa]; T_{sat} is the saturation temperature corresponding to P [°C]; H_{fg} is the latent heat of vaporization of water at T_{sat} [J/kg]; P_c is the water critical pressure 22.1 MPa; D_0 is a reference diameter $12.7{\cdot}10^{-3}$m; ρ_f is the water density at T [kg/m^3]; ρ_g is the vapour density at T_{sat} [kg/m^3]; c_p is the water specific heat at T [J/(kg·°C)]; C_f is a factor depending upon the tube configuration (≈ 1.2 for a smooth channel).

According to this correlation, the CHF for the FW channels is equal to 1.621 MW/m^2. Computing the peak heat flux at the coolant/wall interface as 0.461 MW/m^2 from the heat transfer analysis, the safety margin against DNB is largely above 1 and given by,

$$CHF_{ratio} = \frac{CHF}{q''_{peak,FW}} = 3.516$$

However, it must be pointed out that both pressure drops and CHF calculations have been based on empirical correlations and numerical results computed by FEM analyses where water domain is missing. Hence, they must be taken as preliminary calculations. Further investigations by using a CFD approach are strongly encouraged to get more accurate results.

4.3.2 Mechanical Analysis

With regards to the mechanical analysis of the equatorial cell equipped with the optimized FW, the same loads and the boundary conditions used for the optimization campaign and pertinent to both NO and OP loading scenarios have been applied:

- pressure loads onto the cooling water-wetted surfaces: 15.5 MPa under NO scenario and 18.6 MPa under OP scenario;
- pressure loads onto the breeder-wetted surfaces: 0.5 MPa under NO scenario and 18.6 MPa under OP scenario;
- thermal expansion induced by the thermal field predicted by the steady state heat transfer analysis;
- a proper set of mechanical constraints, with the aim of simulating the structural behaviour of the DEMO breeding blanket as realistic as possible (see Figure 3.11).

The overall thermo-structural response of the system has been obtained by means of three different static linear elastic simulations, each one characterized by a specific set of loads:

1. Only primary loads (i.e. pressure loads) pertinent to the Normal Operation scenario;
2. Only primary loads pertinent to the Over-Pressurization scenario;
3. Only secondary loads (i.e. only the thermal expansion);
4. Primary plus secondary loads pertinent to the Normal Operation scenario;
5. Primary plus secondary loads pertinent to the Over-Pressurization scenario.

Those five distinct simulations have allowed to evaluate several stress distributions arising inside the structure under both the loading scenarios considered, distinguishing them among primary, secondary and peak stresses, as required by the main nuclear standards.

With particular attention to the FW, the primary, secondary and primary plus secondary Von Mises stress fields have been plotted in Figures 4.12 to 4.16 for both the NO and OP scenarios.

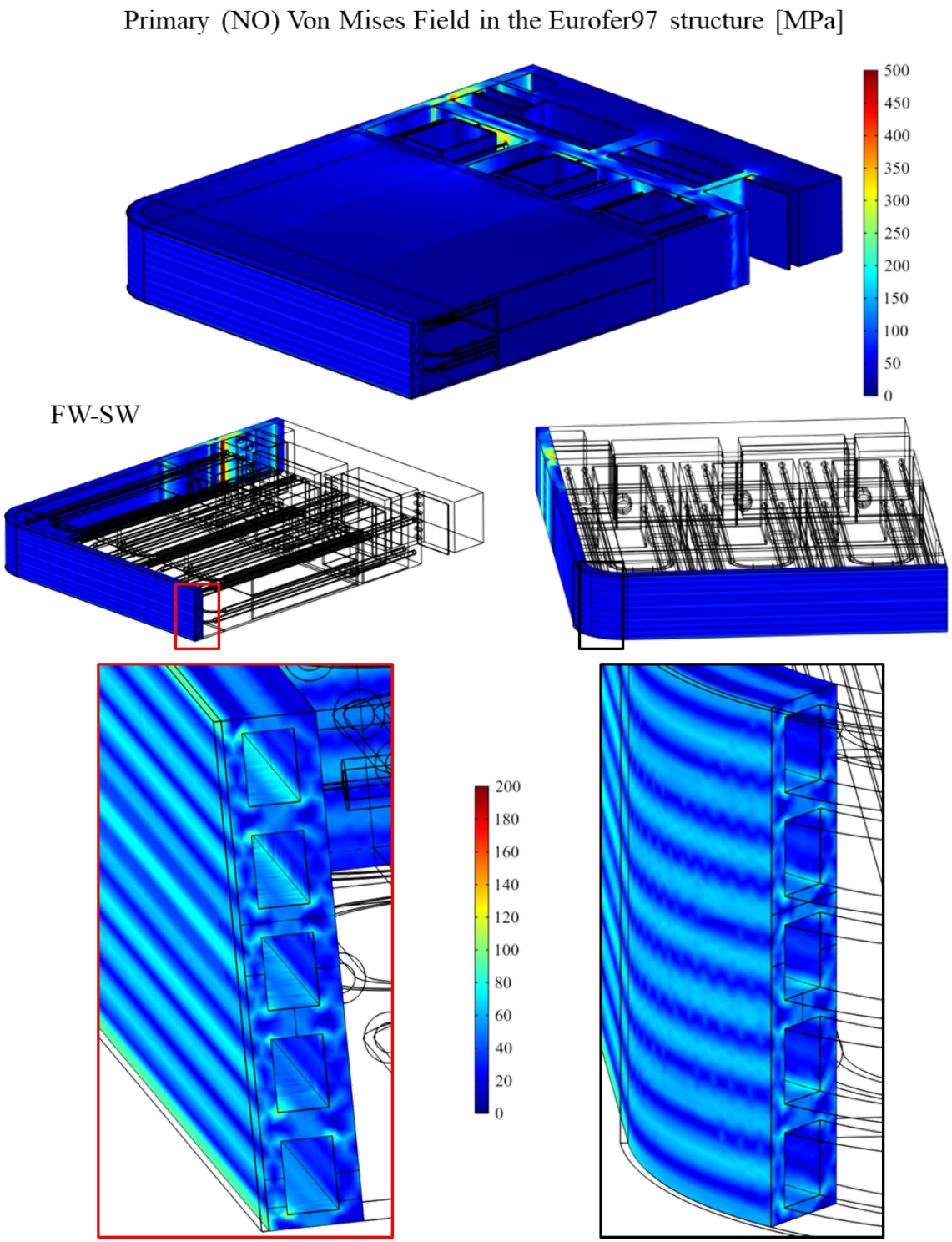

Figure 4.12: Primary stresses distribution in the complex of FW-SW under the NO scenario.

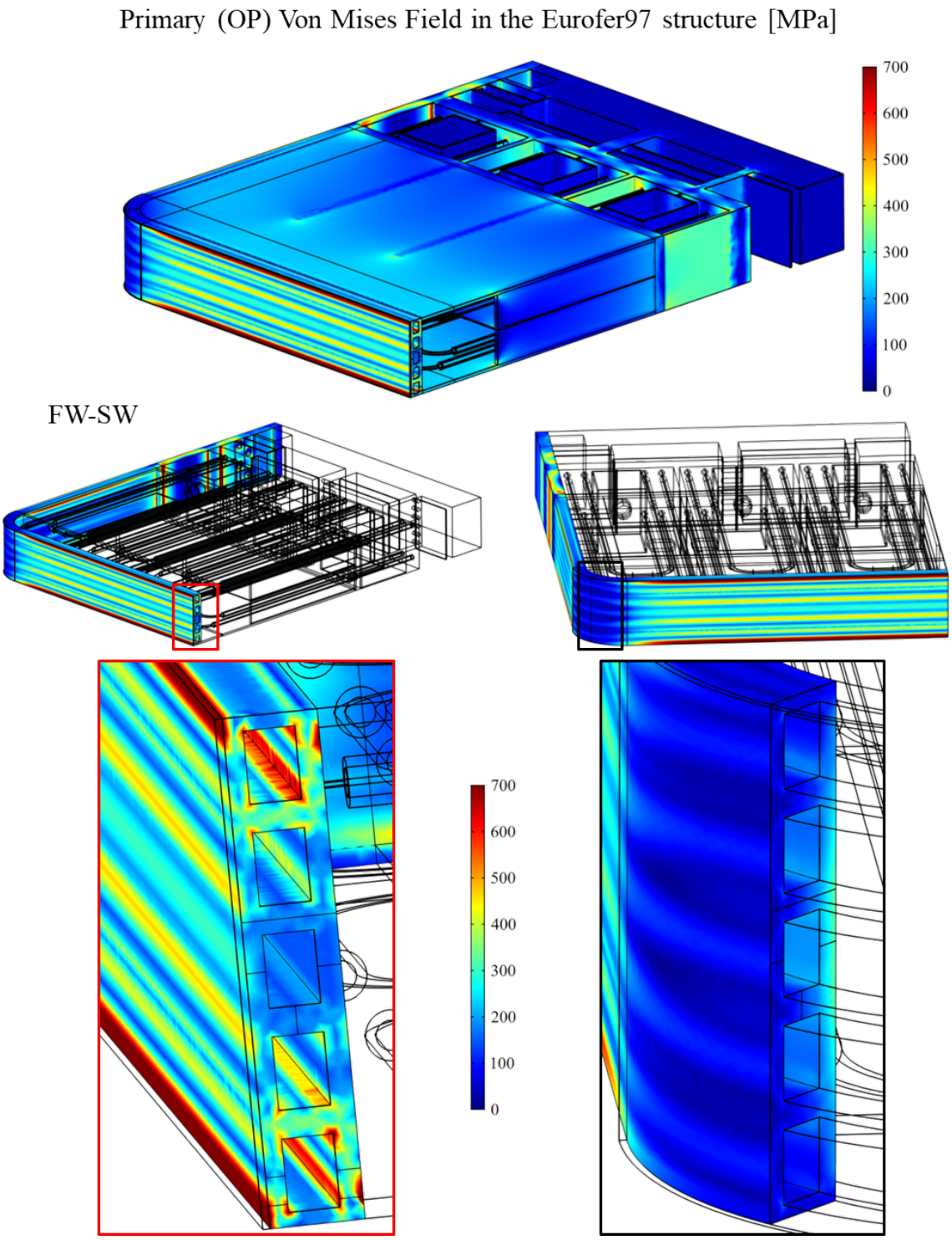

Figure 4.13: Primary stresses distribution in the complex of FW-SW under the OP scenario.

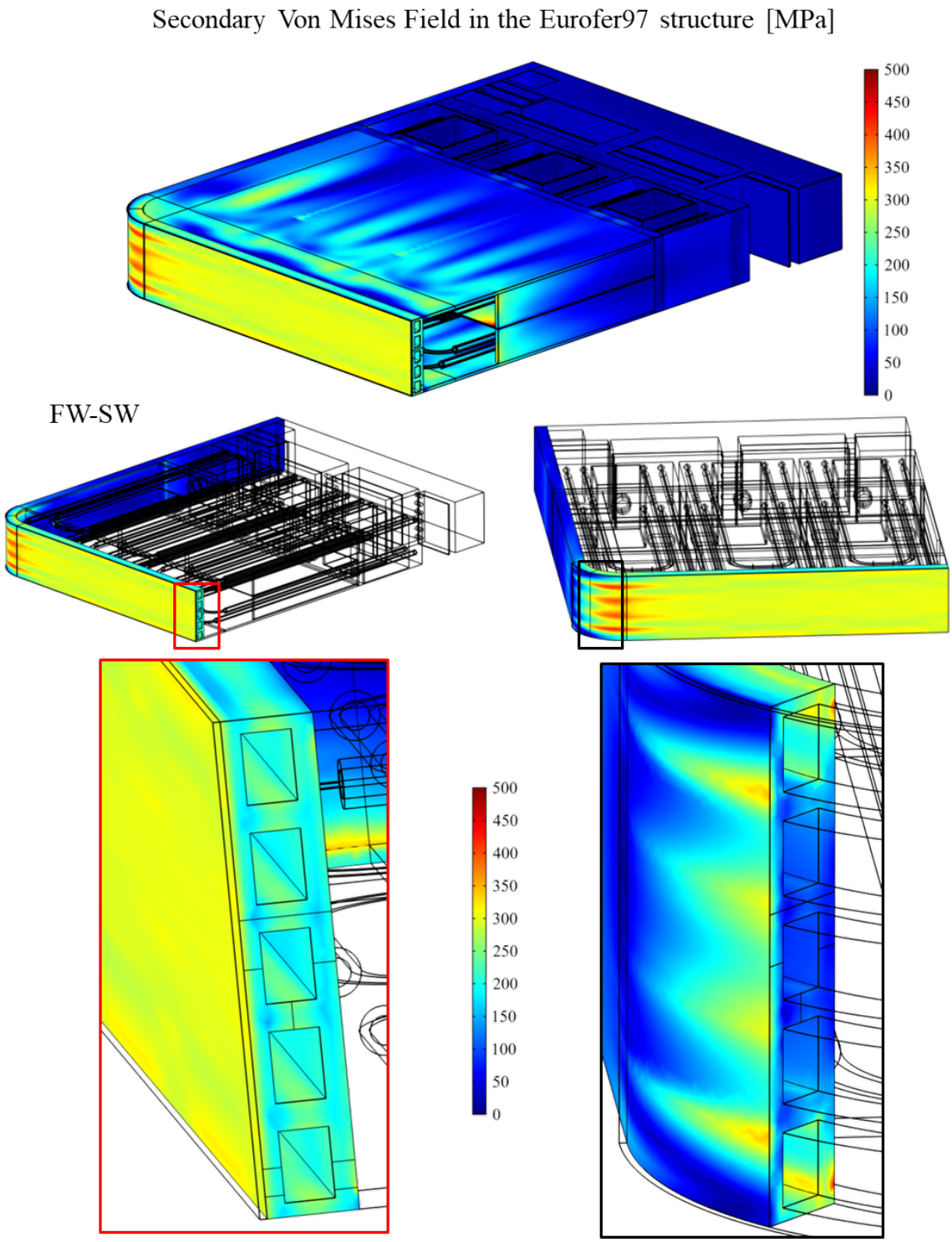

Figure 4.14: Secondary stresses distribution in the complex of FW-SW (the same for both NO and OP scenarios).

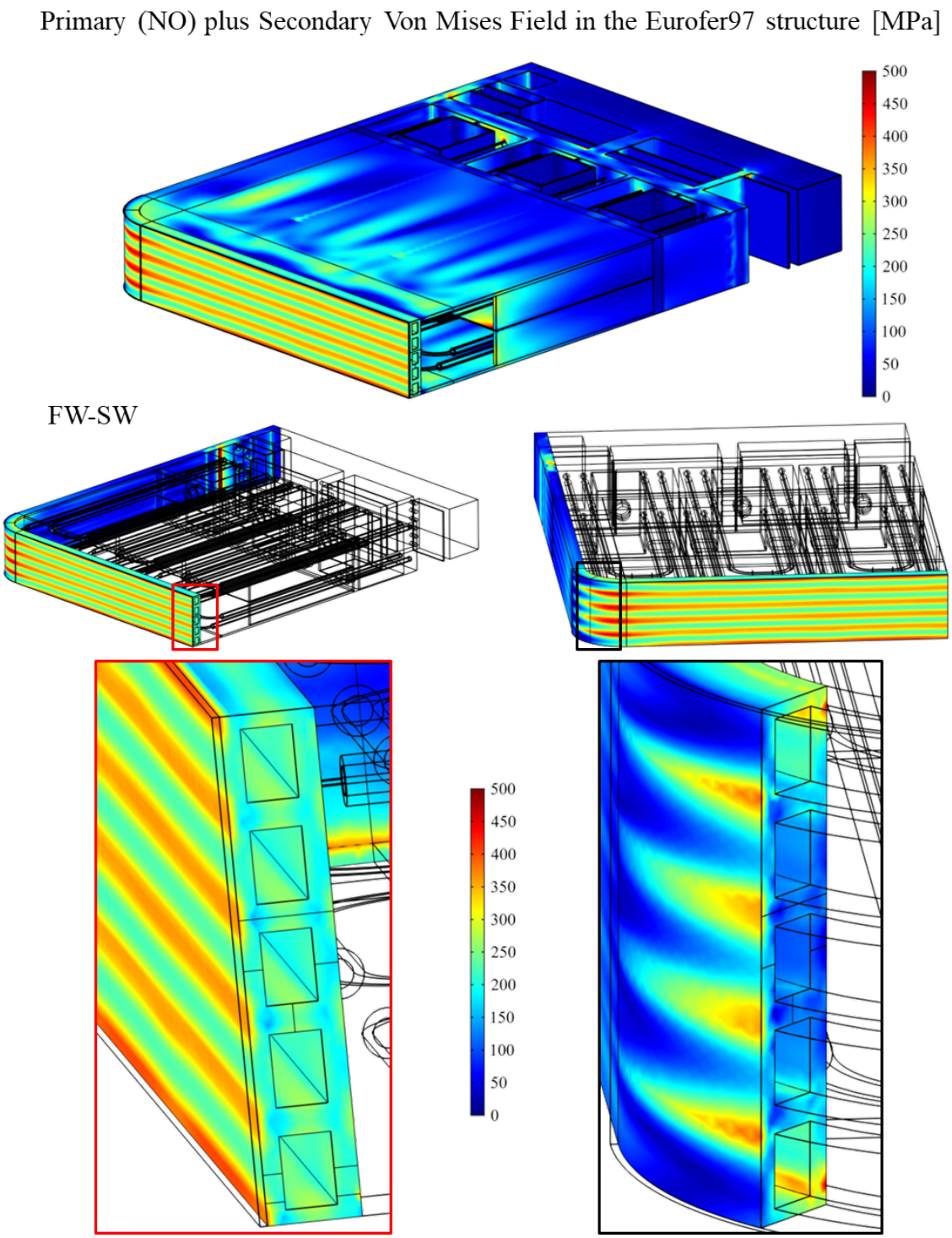

Figure 4.15: Primary plus Secondary stresses distribution in the complex of FW-SW under the NO scenario.

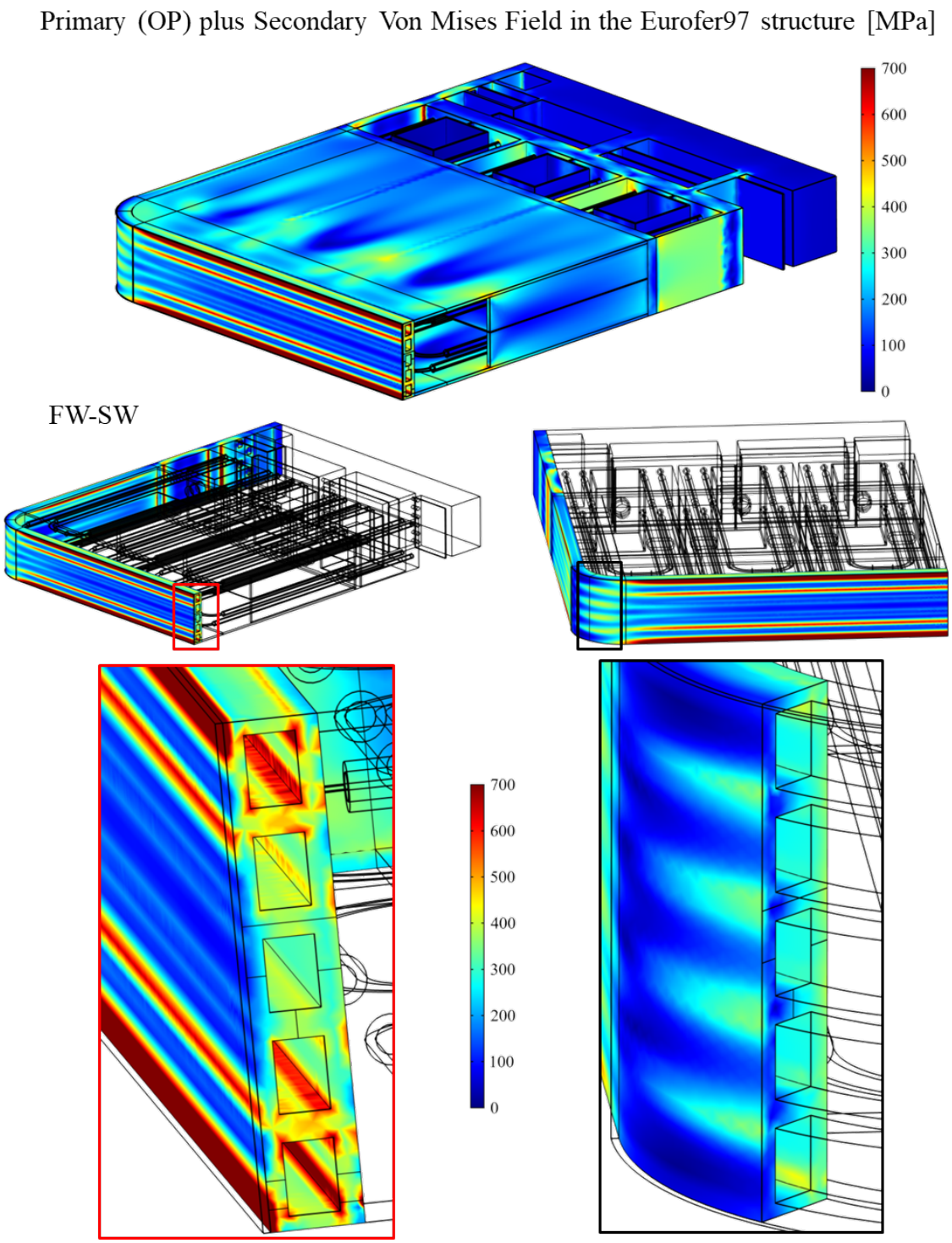

Figure 4.16: Primary plus Secondary stresses distribution in the complex of FW-SW under the OP scenario.

With regards to the OP loading scenario, primary stresses become very significant due to the huge increment of the internal pressure inside the SB (0.5 MPa vs. 18.6 MPa). Such a high value of pressure load generates a relevant bending of the FW, implying high stresses concentrated in correspondence of the joint with the toroidal-radial SPs.

As shown in the plots, during the normal operation of the blanket, pressure loads do not generate high stresses in the FW-SW complex, while the combined effect of internal and external constraints makes significant secondary stresses arise in the FW domain caused by the thermal expansion. As to the latter, Figure 4.17 shows the important tensile yy-component of the secondary stress tensor in the FW.

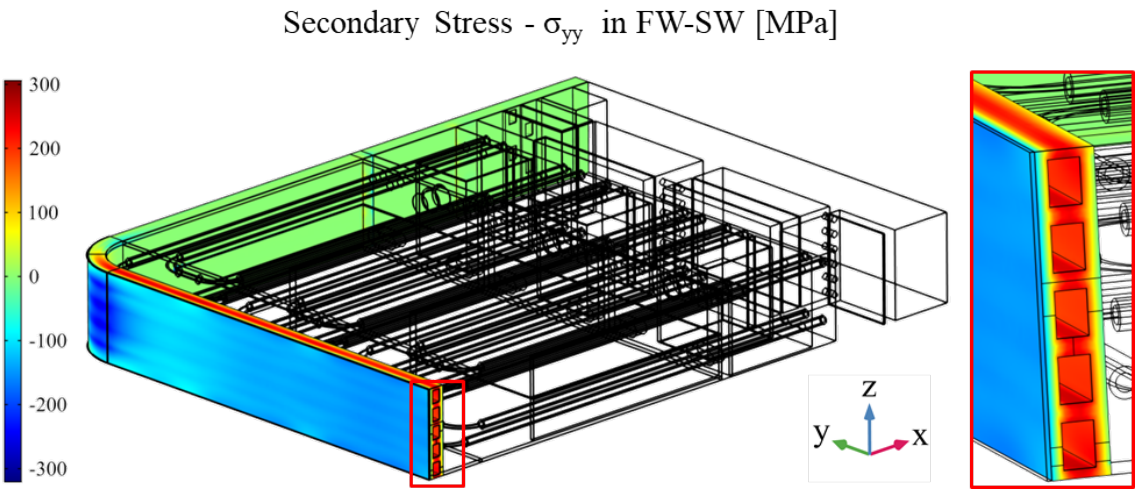

Figure 4.17: Secondary stresses - σ_{yy} component - in the complex of FW-SW.

Nevertheless, it must be pointed out that those high stresses might be caused by the mechanical plain strain boundary conditions applied along the z-direction, which perhaps generates an excessive compressive effect on the FW. In particular, the arise of a radial decreasing temperature profile in the structure together with imposing a uniform poloidal deformation ($\varepsilon_z(x, y)$=const.) to both upper and lower surfaces of the cell, forces the hottest and the coldest regions to undergo the same poloidal deformation, putting hence the regions near the plasma under compression while the rear ones under tensile.

However, the realistic thermo-mechanical behaviour of a continuum *banana-shaped* structure such as the COB segment is still under investigation, and the adoption of the afore-mentioned mechanical boundary condition is currently the most widely adopted for this kind of mechanical analyses involving breeding blanket sub-models, as well as the most conservative one.

For the sake of completeness, the displacement field along the three spatial directions x, y and z, generated by the combined effect of primary and secondary loads during the normal operation has been reported in Figures 4.18 to 4.20, respectively, where also a comparison between deformed and undeformed (in white wireframe) configuration is shown with an iso-amplification factor equal to 10.

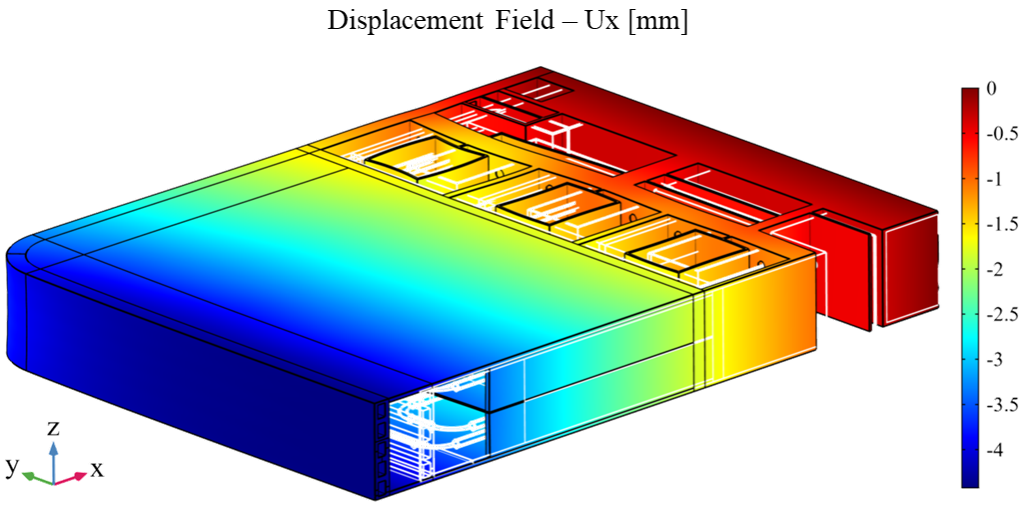

Figure 4.18: Displacement field along the x-direction (iso-amplification factor = 10).

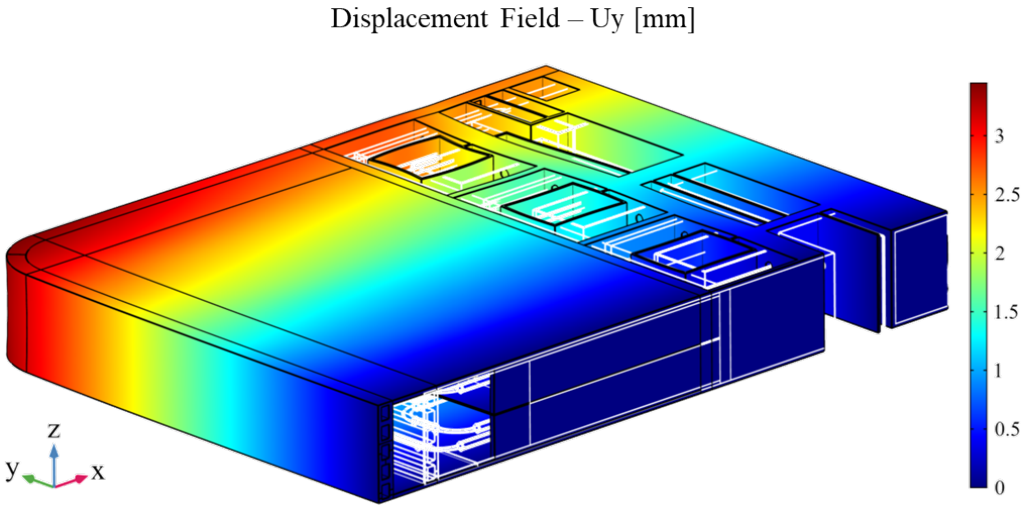

Figure 4.19: Displacement field along the y-direction (iso-amplification factor = 10).

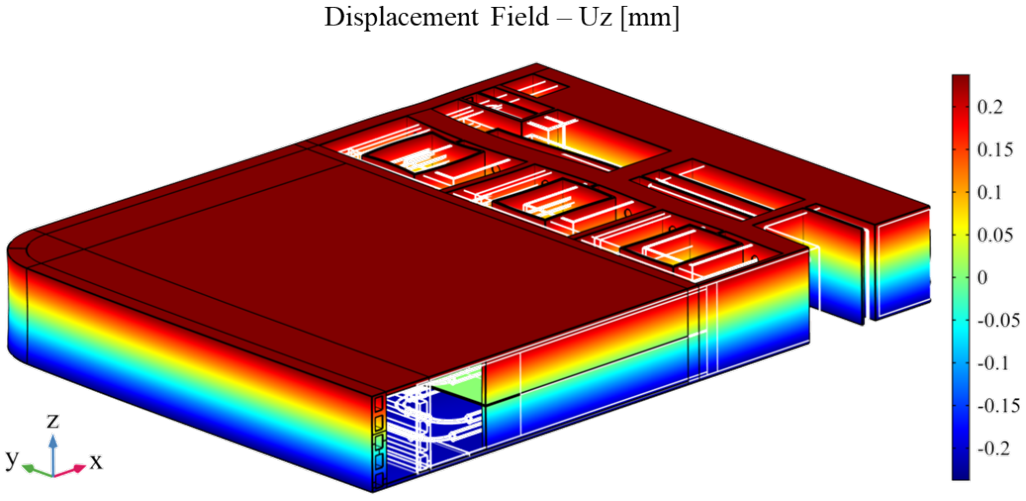

Figure 4.20: Displacement field along the z-direction (iso-amplification factor = 10).

4.4 Structural Integrity Assessment

The structural integrity assessment of the optimized FW has been carried out relying on the numerical results obtained by means of the thermo-mechanical analyses presented above, and following the linear elastic approach outlined in the RCC-MRx.

According to what already described in Chapter 3, a set of supporting lines wherein perform the stress linearization has been identified in the FW-SW domain, focusing the attention on the main relevant thicknesses to be checked. With respect to the paths selected for the optimization campaign, the more detailed discretization has allowed to select two additional supporting lines (SL#11 and SL#12) located in correspondence of the junction between the FW and the toroidal-radial SPs, as shown in Figure 4.21.

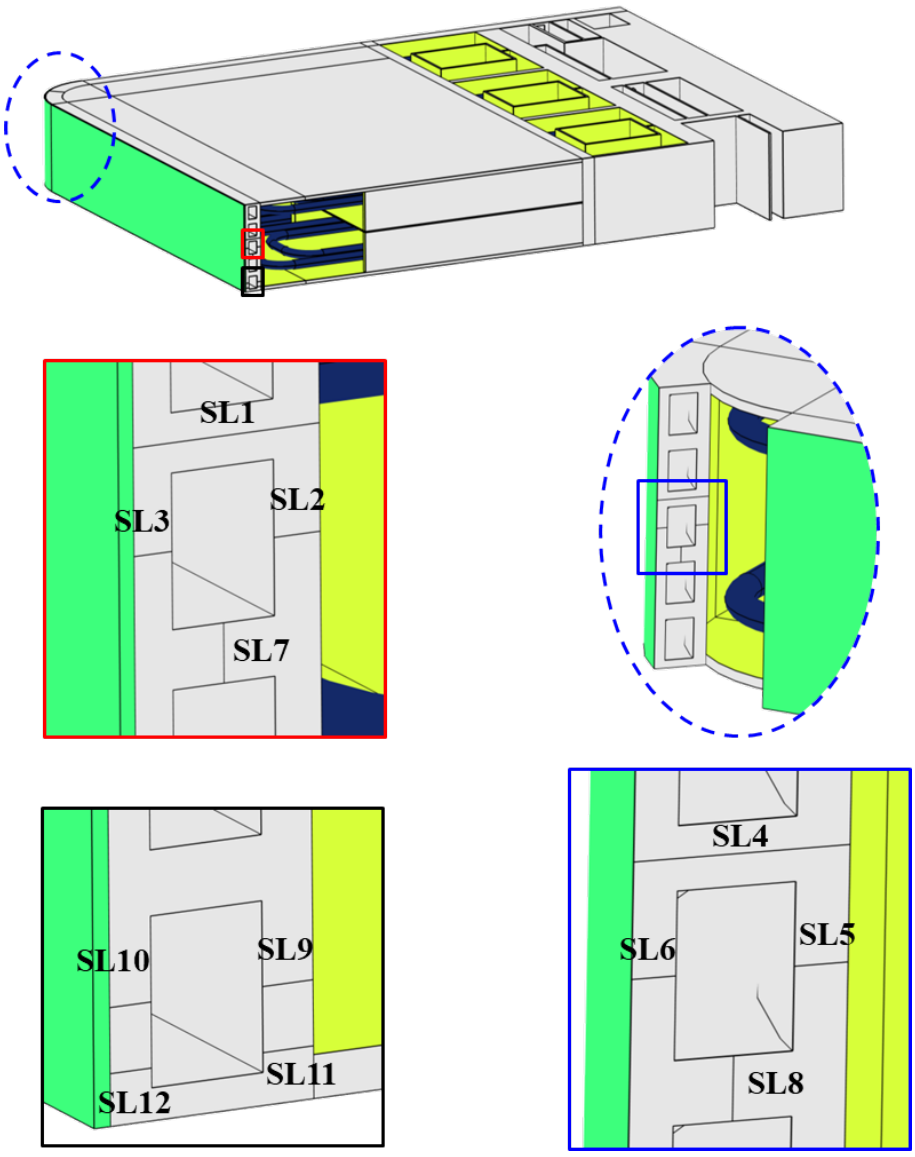

Figure 4.21: Enhanced set of supporting lines used for stress linearization procedure.

With regards to the design criteria without considering neither creep nor irradiation effects, failure due to plastic collapse and instability (i.e. P-type damages) has been assessed, and the results of the application of the rules RB 3251.1 are reported in Tables Tables 4.3 and 4.4 for Level A and Level D, respectively. The allowable stresses S_m have been drawn from Figure 3.13.

Path	$\mathbf{T}_{ave}$ [°C]	$(\overline{P_m})_A/S_{m,A}$	$(\overline{P_L+P_b})_A/1.5S_{m,A}$
SL1	366.8	0.138	0.095
SL2	378.9	0.084	0.159
SL3	395.3	0.105	0.283
SL4	346.4	0.138	0.106
SL5	347.6	0.061	0.178
SL6	372.4	0.131	0.237
SL7	331.3	0.260	0.175
SL8	324.2	0.259	0.178
SL9	371.2	0.101	0.202
SL10	395.2	0.086	0.248
SL11	371.6	0.179	0.123
SL12	395.9	0.292	0.299

Table 4.3: Results for plastic collapse and instability in Level A (satisfied if value is lower than 1).

Path	$\mathbf{T}_{ave}$ [°C]	$(\overline{P_m})_D/S_{m,D}$	$(\overline{P_L+P_b})_D/1.5S_{m,D}$
SL1	366.8	0.369	0.309
SL2	378.9	0.403	0.353
SL3	395.3	0.630	0.609
SL4	346.4	0.341	0.556
SL5	347.6	0.722	0.627
SL6	372.4	0.125	0.201
SL7	331.3	0.443	0.299
SL8	324.2	0.342	0.236
SL9	371.2	0.798	0.818
SL10	395.2	0.588	0.403
SL11	371.6	0.575	**1.590**
SL12	395.9	0.724	**1.446**

Table 4.4: Results for plastic collapse and instability in Level D (satisfied if value is lower than 1).

The results show that, as to the normal operation, both criteria are satisfied in all the selected supporting lines, whereas failure for plastic instability occurs in paths

SL11 and SL12 considering the Level D scenario. Indeed, the over-pressurization of the SB generates a significant bending of the FW causing a high resultant moment in correspondence of the junction between the FW and the toroidal-radial SPs. Nonetheless, it must be pointed out that both lines SL11 and SL12 have been put in regions where the impact of the plane strain boundary conditions might be slightly misleading.

As to the cyclic loads when both creep and irradiation are neglected, failure against ratcheting and fatigue in non-singular zones have been verified. Since no thermo-mechanical analysis has been performed at the end of the cycle, the stress has been conservatively assumed to vary between zero and maximum of the cycle (i.e. $\Delta\sigma \approx \sigma$). The results obtained applying the $3S_m$ rule for progressive deformations have been reported in Table 4.5.

Path	$\mathbf{T}_{ave}$ [°C]	$(\max \overline{[\boldsymbol{P_L} + \boldsymbol{P_b}]} + \overline{\boldsymbol{\Delta Q}})_{\boldsymbol{A}}/\boldsymbol{3S_{m,A}}$
SL1	366.8	0.388
SL2	378.9	0.492
SL3	395.3	0.725
SL4	346.4	0.266
SL5	347.6	0.232
SL6	372.4	0.564
SL7	331.3	0.508
SL8	324.2	0.259
SL9	371.2	0.577
SL10	395.2	0.693
SL11	371.6	0.524
SL12	395.9	0.669

Table 4.5: Results for ratcheting (satisfied if value is lower than 1).

The results obtained show that no sections undergo failure for ratcheting, where the lowest margin has been computed in correspondence of the thickness separating the cooling channel from the W-armour.

Regarding the fatigue, the total strain range intensity $\overline{\Delta\varepsilon}$ has been calculated according to Equation (3.7). In particular, instead of using the correction factor K_ε, the additional plastic strain $\overline{\Delta\varepsilon_3}$ has been evaluated by means of the intersection of the cyclic curves with the Neuber's hyperbola, as shown in Figure 4.22.

As to the additional plastic strain due to triaxiality effect $\overline{\Delta\varepsilon_4}$, the correction factor K_ν for linear elastic calculations has been drawn from [63] (see Figure 4.23).

Finally, the total strain range obtained for each path has been used to enter in the strain-life design curves reported in Figure 4.24 to determine the maximum allowable number of cycles N for each path. The results have been reported in Table 4.6.

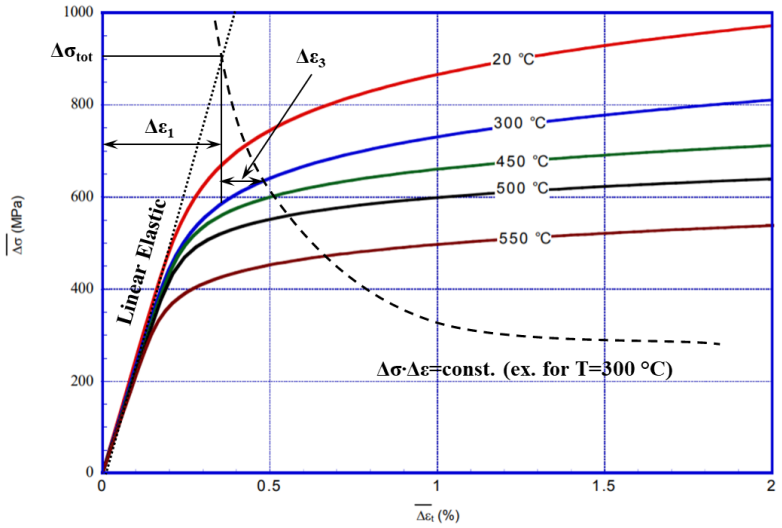

Figure 4.22: Eurofer97 cyclic curves [63] with example of Neuber's hyperbola.

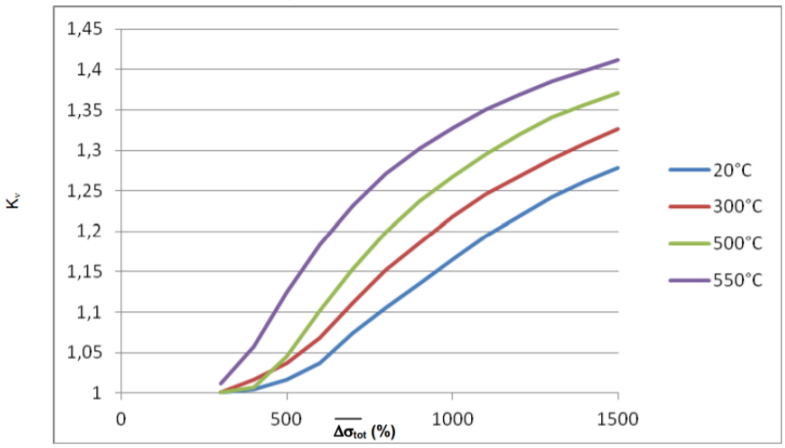

Figure 4.23: Triaxiality correction factor K_ν for Eurofer97 [63].

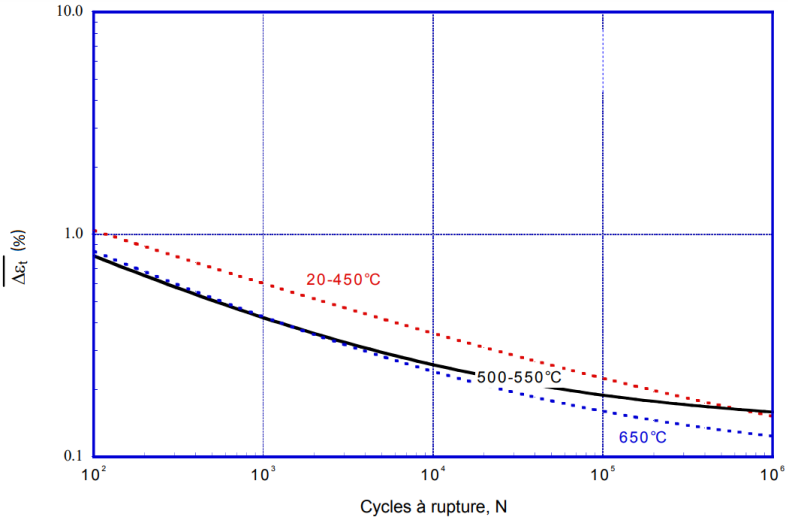

Figure 4.24: Fatigue design curves for Eurofer97 [63].

Since a single line is reported for the range 20-450 °C, all the paths selected have been referred to that curve. As shown in the table, fatigue does not seem to be an issue for the FW, at least in non-singular zones. In fact, the maximum allowable number of cycles is everywhere around or above 10^6.

Path	$\overline{\Delta\varepsilon_{tot}}$ [%]	N_{max}
SL1	0.158	$\approx 10^6$
SL2	0.099	$> 10^6$
SL3	0.101	$> 10^6$
SL4	0.153	$\approx 10^6$
SL5	0.081	$> 10^6$
SL6	0.085	$> 10^6$
SL7	0.113	$> 10^6$
SL8	0.084	$> 10^6$
SL9	0.108	$> 10^6$
SL10	0.103	$> 10^6$
SL11	0.133	$> 10^6$
SL12	0.145	$\approx 10^6$

Table 4.6: Results for fatigue in terms of maximum allowable number of cycles.

Considering the irradiation effects, low temperature rules (i.e. negligible creep) to prevent immediate plastic flow localization and immediate fracture due to exhaustion of ductility have been checked. The allowable stresses S_{em} and S_{et} have been drawn from Figures 3.15 and 4.25. The results have been reported in Tables 4.7 and 4.8 for Level A and Level D, respectively.

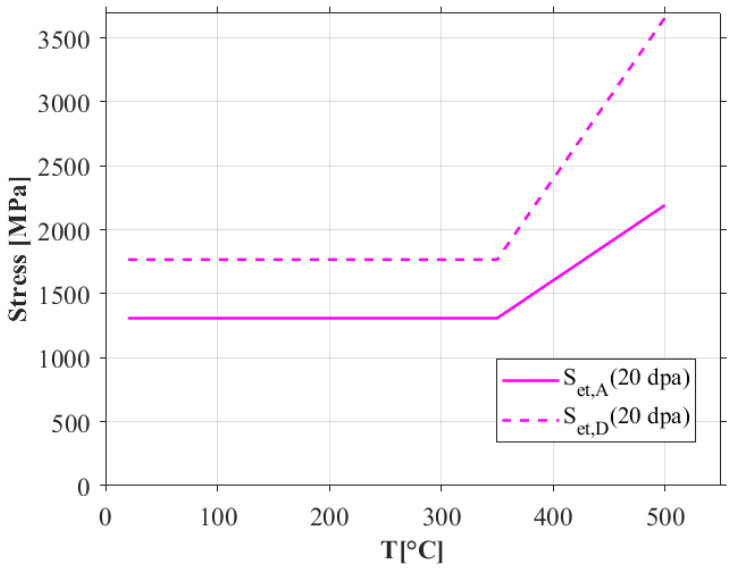

Figure 4.25: Eurofer97 allowable stress S_{et} vs. temperature [71] (not available in RCC-MRx 2012 edition).

Path	$\mathbf{T}_{ave}$ [°C]	$(\overline{P_m + Q_m})_A/S_{em,A}$	$(\overline{P_m + P_b + Q + F})_A/S_{et,A}$
SL1	366.8	0.583	0.256
SL2	378.9	0.566	0.153
SL3	395.3	0.633	0.146
SL4	346.4	0.280	0.268
SL5	347.6	0.230	0.083
SL6	372.4	0.482	0.123
SL7	331.3	0.786	0.199
SL8	324.2	0.385	0.099
SL9	371.2	0.657	0.173
SL10	395.2	0.654	0.148
SL11	371.6	0.643	0.212
SL12	395.9	0.679	0.206

Table 4.7: Results for immediate plastic flow localization (column 3) and immediate fracture due to exhaustion of ductility (column 4) in Level A at 20 dpa (satisfied if value is lower than 1).

Path	$\mathbf{T}_{ave}$ [°C]	$(\overline{P_m + Q_m})_D/S_{em,D}$	$(\overline{P_m + P_b + Q + F})_D/S_{et,D}$
SL1	366.8	0.559	0.226
SL2	378.9	0.571	0.175
SL3	395.3	0.367	0.124
SL4	346.4	0.350	0.218
SL5	347.6	0.617	0.198
SL6	372.4	0.241	0.082
SL7	331.3	0.742	0.217
SL8	324.2	0.422	0.126
SL9	371.2	0.629	0.179
SL10	395.2	0.676	0.150
SL11	371.6	0.595	0.385
SL12	395.9	0.739	0.406

Table 4.8: Results for immediate plastic flow localization (column 3) and immediate fracture due to exhaustion of ductility (column 4) in Level D at 20 dpa (satisfied if value is lower than 1).

For both the rules considering irradiation effects, no issues have been observed and the criteria are fulfilled in all the selected paths.

As far as the damage caused by creep is concerned, the activation temperature for Eurofer97 is in the range between 375-450 °C. However, no data about creep stress limits are available in the RCC-MRx 2012 edition and, thus, different sources have been referred to. In particular, the stress limit S_t for creep excessive deformation

(1%), to be checked in Level A, has been drawn from [19] and plotted in Figure 3.14, whereas the stress-to-rupture S_r, to be checked in Level D, has been drawn from [80] and reported in Figure 4.26. The same data can be also plotted as a function of the Larson-Miller Parameter (P), as shown in Figure 4.27.

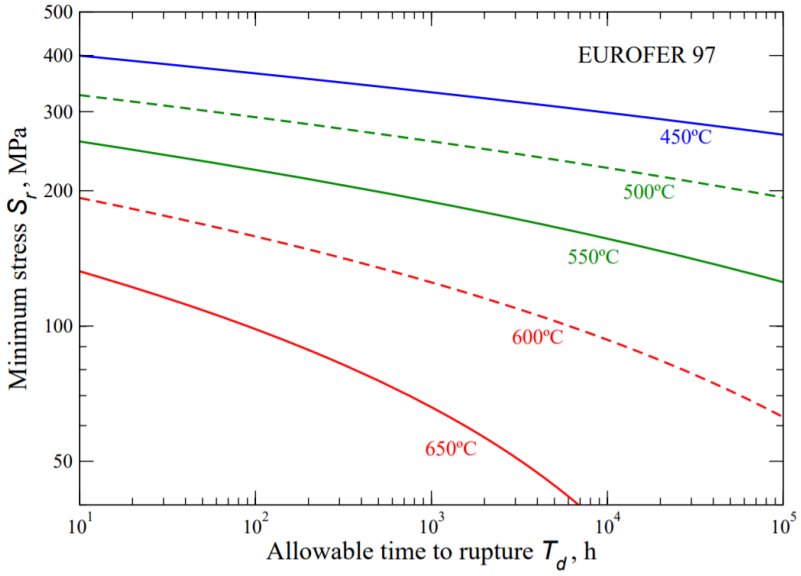

Figure 4.26: Stress-to-rupture S_r vs. Larson-Miller Parameter for Eurofer97 [80] (not available in RCC-MRx 2012 edition).

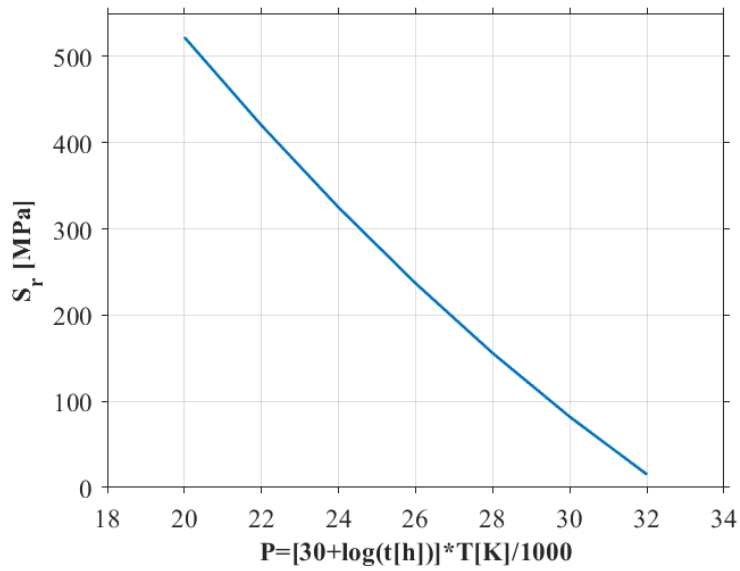

Figure 4.27: Stress-to-rupture S_r vs. time-to-rupture for Eurofer97 [80] (not available in RCC-MRx 2012 edition).

As shown in the plots, creep stress limits below 450 °C are not provided and, hence, this value has been considered as the one above which the high temperature rules should be considered. Looking at the average temperature of the selected paths in the FW domain under nominal operating conditions (see Table 4.3 for example),

all of them are lower than 400 °C and, thus, no creep failure is predicted in the FW domain, according to the available data.

Furthermore, those temperature profiles are also helpful to identify potential region when irradiation embrittlement can occur with a major impact, causing large positive shift of the DBTT.

During the optimization campaign, a lower constraint was considered on the average temperature of the majority of selected paths in the FW domain, fixing a minimum value of 350 °C, according to Figure 1.14.

The results obtained from the heat transfer analysis of the optimized FW have positively shown that the majority of the FW thicknesses are characterized by an average temperature lying in the range 350-400 °C, which is optimal to avoid either severe irradiation embrittlement and creep deformation. The paths showing an average temperature lower than 350 °C are SL4 and SL5, located in the FW corners but both very close to the limit ($\approx$ 347°C), together with SL7 and SL8. Although the average temperature on the latter are quite below 350 °C, crack propagation along those paths can be considered as of less importance, referring to thicknesses separating two consecutive cooling channels instead of different environments (i.e. cooling channels/breeder zone or cooling channels/plasma chamber).

In general, the structural integrity assessment carried out on the optimized FW of the equatorial cell of the WCLL COB segment shows that the structure withstand safely the normal operating conditions, considering both primary and secondary loads. Moreover, no significant creep deformation has been predicted within the FW-SW domain. On the other hand, particular attention needs to be addressed to the Over-Pressurization scenario, where small regions close to the junction between the FW and the toroidal-radial SPs undergo failure for plastic collapse and instability.

Conclusions

My research activity carried out during the XXXIII cycle of the Ph.D. course in Energy and Information Technologies takes place within the framework of the R&D activities on the DEMO Breeding Blanket, promoted and supported by the EUROfusion Consortium.

The main topic of such an activity concerned the development of a multiphysics tool to be used for optimizing the design of the water-cooled breeding blanket concept foreseen for DEMO, taking into account its nuclear, thermal-hydraulic and thermo-mechanical design aspects. In particular, the attention has been focused on the internal cooling channels housed within the complex of Side Walls and First Wall, trying to figure which is the best layout for maximizing the tritium breeding performances of the blanket without undermining its structural integrity.

In order to do that, the derivative-free Complex method has been applied for the design optimization of the European DEMO Water-Cooled Lithium Lead (WCLL) breeding blanket concept. To this purpose, a potential performances-based objective function to be minimized has been defined by means of a heuristic approach and validated by neutron transport analyses. Moreover, a parametric multiphysics model of a single equatorial cell of the Central Outboard Blanket segment (relying on an alternative concept developed at University of Palermo) has been set up inside the FEM code COMSOL in order to solve the coupled thermo-mechanical problem and check the fulfillment of the prescribed functional and structural requirements. Using a live-link between MATLAB (wherein the optimization algorithm has been implemented) and COMSOL, the optimization campaign led the design towards an optimum point compliant with the adopted constraints.

Considering such a complex multiphysic problem as the fusion breeding blanket design, the adoption of the Complex method has allowed to successfully enhance the design of the WCLL BB, focusing on a particular component such the FW, with a much lower number of numerical analyses than the huge amount usually required by a conventional parametric sweep approach, where conversely hundreds (or even thousands) of analyses could be needed to properly investigate all the phase space of the variables and to identify an optimized configuration.

Once obtained the optimized design, its nuclear, thermal-hydraulic and structural performances have been investigated with more detailed numerical models.

From the nuclear point of view, the new layout of the FW cooling channels allows an increment in TBR performances up to around 10% and 13% with respect to the Case#1 and Case#2, respectively, that are actual potential configurations under investigation for the WCLL BB. Being always been a weakness of the water-based breeding blanket, this achievement is surely very promising.

As to the thermal-hydraulics, the highest temperature reached in the Eurofer97 structure of the equatorial cell is lower than the maximum allowable limit of 550 °C. Moreover, no particular issues have been observed in terms of either pressure drops or DNB phenomena.

Finally, as far as the thermo-mechanical performances are concerned, the optimized FW withstand safely the design criteria reported in the RCC-MRx concerning the Normal Operation scenario (Level A), while the region in correspondence of the joint with the toroidal-radial SPs might undergo failure for plastic instability. No significant creep deformation has been predicted in the FW domain being the average temperature along the most relevant sections lower than 400 °C. However, it must be highlighted that some regions of the FW-SWs complex might suffer irradiation embrittlement due to the low operating temperature of the coolant. Indeed, the material close to the cooling channels will undergo high dpa damage working with an operative temperature lower than 350 °C, causing thus a positive shift of the DBTT quite above the room temperature. This latter aspect might introduce several problems involving the start-up and shut-down scenarios of the components, as well as its maintenance and the removal, that have to be properly managed relying for instance on thermal annealing and/or pre-heating procedures.

The overall activity shows that some improvements in water-cooled breeding blankets can be achieved increasing the amount of water in the FW, enhancing the moderating effect of the latter on the very high energy neutrons coming from the plasma and increasing, thus, the tritium production inside the component. On the other hand, more R&D activity on the structural materials to be used in the blanket is still needed if we want to enhance the design of such a component. Both high irradiation and high temperature cause several strain to the material and, in order to get sustainable lifetime for the future fusion reactors, its performances under such extreme environments have still to be improved.

Acknowledgements

I would like to really thank Prof. Pietro Alessandro Di Maio for having believed in me and encouraged me to carry out this interesting research activity.

Special thanks also to Dr. Pierluigi Chiovaro for the huge support he gave to me to set-up the optimization problem and to carry out the neutron-photon transport analyses.

Finally, I am very grateful to Prof. Nasr M. Ghoniem for having given to me the opportunity to join his group at UCLA for a while as well as for having shared his expertise with me, which has been fundamental to realize this work.

References

[1] T. Donné et al., *European Research Roadmap to the Realisation of Fusion Energy*, EUROfusion, 2018, ISBN 978-3-00-061152-0.

[2] *https://www.iter.org/*

[3] G. Federici et al., *Overview of the DEMO staged design approach in Europe*, Nuclear Fusion, (58) 2019, n.6, DOI:10.1088/1741-4326/ab1178.

[4] C. Bachmann et al., *Critical design issues in DEMO and solution strategies*, Fusion Engineering and Design, (146) 2019, pp. 178-181, DOI:10.1016/j.fusengdes.2018.12.013.

[5] F. Cismondi et al., *Progress in EU Breeding Blanket design and integration*, Fusion Engineering and Design, (136) 2018, pp. 782-792, DOI:10.1016/j.fusengdes.2018.04.009.

[6] A.A. Harms et al., *Principles of Fusion Energy. An Introduction to Fusion Energy for Students of Science and Engineering.*, World Scientific Publishing, 2002, ISBN 981-02-4335-9.

[7] E. Vallone, *Numerical Assessment of the Thermal-Hydraulic Performances of the ITER Blanket Cooling System*, Doctoral Thesis, 2018, Ref: http://hdl.handle.net/10447/338061

[8] G. Pérez-Pichel et al., *Analysis of a tile repair technique based on brazing process for ITER First Wall*, Fusion Engineering and Design, (122) 2017, pp. 186-195, DOI:10.1016/j.fusengdes.2017.08.019

[9] L. Giancarli et al., *Overview of recent ITER TBM Program activities*, Fusion Engineering and Design, (158) 2020, 111674, DOI:10.1016/j.fusengdes.2020.111674

[10] F. Hernández et al., *Consolidated Design of the HCPB Breeding Blanket for the pre-Conceptual Design activities of the EU DEMO and Harmonization with the ITER HCPB TBM Program*, Fusion Engineering and Design, (157) 2020, 111614, DOI:10.1016/j.fusengdes.2020.111614

[11] F. Hernández et al., *Advancements in the Helium Cooled Pebble Bed Breeding Blanket for the EU DEMO: Holistic Design Approach and Lessons Learned*, Fusion Science and Technology, (75) 2019, pp. 352-364, DOI:10.1080/15361055.2019.1607695

[12] I. Moscato, *Thermal-hydraulic Study in Support of the Design of the DEMO Balance Of Plant*, Doctoral Thesis, 2020, Ref: http://hdl.handle.net/10447/395492

[13] A. Del Nevo et al., *Recent progress in developing a feasible and integrated conceptual design of the WCLL BB in EUROfusion project*, Fusion Engineering and Design, (146-B) 2019, pp. 1805-1809, DOI:10.1016/j.fusengdes.2019.03.040

[14] R. Forte et al., *Preliminary design of the top cap of DEMO Water-Cooled Lithium Lead breeding blanket segments*, Fusion Engineering and Design, (161) 2020, 111884, DOI:10.1016/j.fusengdes.2020.111884

[15] M. Eboli et al., *Simulation study of pressure trends in the case of loss of coolant accident in Water Cooled Lithium Lead blanket module*, Fusion Engineering and Design, (98-99) 2015, pp. 1763-1766, DOI:10.1016/j.fusengdes.2015.05.034

[16] A. Del Nevo et al., *WCLL BB design and Integration studies 2019 activities*, Internal Deliverable BB-3.2.1-T006-D001, 2019, EUROfusion IDM, Ref.:EFDA_D_2P5NE5

[17] G.R. Odette, S. Zinkle, *Structural Alloys for Nuclear Energy Applications*, Elsevier, 2019, ISBN 978-0-12-397046-6.

[18] S. Zinkle, J. Busby, *Structural materials for fission fusion energy*, materials today, (12-11) 2009, pp. 12-19, DOI:10.1016/S1369-7021(09)70294-9

[19] F. Gillemot et al., *Material Property Handbook pilot project on EUROFER97 (MTA EK, KIT)*, EUROfusion Final Report, 2016, EFDA IDM Ref.: EFDAD2MRP77.

[20] E. Lucon, W. Vandermeulen, *Overview and critical assessment of the tensile properties of unirradiated and irradiated Eurofer97*, Open Report SCK CEN-BLG-1042, 2007.

[21] H. Tanigawa et al., *Status and key issues of reduced activation ferritic/martensitic steels as the structural material for a DEMO blanket*, Journal of Nuclear Materials, (417) 2011, pp. 9-15, DOI:10.1016/j.jnucmat.2011.05.023

[22] E. Gaganidze, J. Aktaa, *Assessment of neutron irradiation effects on RAFM steels*, Fusion Engineering and Design, (88-3) 2013, pp. 118-128, DOI:10.1016/j.fusengdes.2012.11.020

[23] P. Fernández et al., *Creep strength of reduced activation ferritic/martensitic steel Eurofer'97*, Fusion Engineering and Design, (75-79) 2005, pp. 1003-1008, DOI:10.1016/j.fusengdes.2005.06.085

[24] F. Özkan, J. Aktaa, *Creep fatigue assessment for EUROFER components*, Fusion Engineering and Design, (100) 2015, pp. 563-540, DOI:10.1016/j.fusengdes.2015.08.002

[25] J. Aktaa et al., *Creep-fatigue design rules for cyclic softening steels*, Fusion Engineering and Design, (118) 2019, pp. 98-103, DOI:10.1016/j.ijfatigue.2018.08.008

[26] J. Aktaa, R. Schmitt, *High temperature deformation and damage behavior of RAFM steels under low cycle fatigue loading: Experiments and modeling*, Fusion Engineering and Design, (81-19) 2006, pp. 2221-2231, DOI:10.1016/j.fusengdes.2006.03.002

[27] S. Smolentsev et al., *Numerical study of corrosion of ferritic/martensitic steels in the flowing PbLi with and without a magnetic field*, Journal of Nuclear Materials, (432-1/3) 2013, pp. 294-304, DOI:10.1016/j.jnucmat.2012.08.027

[28] R. Moreau et al., *Eurofer corrosion by the flow of the eutectic alloy Pb–Li in the presence of a strong magnetic field*, Fusion Engineering and Design, (86-1) 2011, pp. 106-120, DOI:10.1016/j.fusengdes.2010.08.050

[29] C. Reux et al., *DEMO reactor design using the new modular system code SYCOMORE*, Nuclear Fusion, (55-7) 2015, 073011, DOI:10.1088/0029-5515/55/7/073011

[30] M. Kovari et al., *"PROCESS": A systems code for fusion power plants—Part 1: Physics*, Fusion Engineering and Design, (89-12) 2014, pp. 3054-3069, DOI:10.1016/j.fusengdes.2014.09.018

[31] S.C. Chapra, R-P. Canale, *Numerical Methods for Engineers*, McGraw-Hill, 2015, ISBN 978–0–07–339792–4.

[32] G.S. Fishman, *Monte Carlo: Concepts, Algorithms, and Applications.*, New York: Springer, 1995, ISBN 978-0-387-94527-9.

[33] J. Spanier, E.M. Gelbard, *Monte Carlo Principles and Neutron Transport Problems*, Dover Pubns, 2008, ISBN 978-0-486-46293-6.

[34] H.K. Versteeg, W. Malalasekera, *An Introduction to Computational Fluid Dynamics: the Finite Volume Method.*, Pearson, 2007, ISBN 978-0-131-27498-3.

[35] K. Bathe, *Finite Element Procedures*, Pearson, 1995, ISBN 978-0-133-01458-7.

[36] Y. Huang et al., *Thermo-structural design of the European DEMO water-cooled blanket with a multiscale-multiphysics framework*, Fusion Engineering and Design, (135-A) 2018, pp. 31-41, DOI:10.1016/j.fusengdes.2018.07.007

[37] G.A. Spagnuolo et al., *A multi-physics integrated approach to breeding blanket modelling and design*, Fusion Engineering and Design, (143) 2019, pp. 35-40, DOI:10.1016/j.fusengdes.2019.03.131

[38] F. Maviglia et al., *Effect of engineering constraints on charged particle wall heat loads in DEMO*, Fusion Engineering and Design, (124) 2017, pp. 385-390, DOI:10.1016/j.fusengdes.2017.02.077

[39] F. Moro et al., *Nuclear analysis of the Water cooled lithium lead DEMO reactor*, Fusion Engineering and Design, (160) 2020, 111833, DOI:10.1016/j.fusengdes.2020.111833

[40] P. Chiovaro et al., *Study of the helium-cooled lithium lead test blanket module nuclear behaviour under irradiation in ITER*, Fusion Engineering and Design, (84-12) 2009, pp. 2178-2186, DOI:10.1016/j.fusengdes.2009.04.001

[41] F. Edemetti et al., *DEMO WCLL breeding zone cooling system design: Analysis and discussion*, Fusion Engineering and Design, (146-B) 2019, pp. 2632-2638, DOI:10.1016/j.fusengdes.2019.04.063

[42] P.A. Di Maio et al., *On the thermo-mechanical behaviour of DEMO water-cooled lithium lead equatorial outboard blanket module*, Fusion Engineering and Design, (124) 2017, pp. 725-729, DOI:10.1016/j.fusengdes.2017.05.051

[43] U. Fischer et al., *Required, achievable and target TBR for the European DEMO*, Fusion Engineering and Design, (155) 2020, 111553, DOI:10.1016/j.fusengdes.2020.111553

[44] J. Aubert et al., *Thermo-mechanical analyses and ways of optimization of the helium cooled DEMO First Wall under RCC-MRx rules*, Fusion Engineering and Design, (124) 2017, pp. 473-474, DOI:10.1016/j.fusengdes.2016.12.040

[45] S.S. Rao, *Engineering Optimization: Theory and Practice*, John Wiley & Sons Inc., 2009, ISBN 978-0-470-18352-6.

[46] W.W. Garvin, *Introduction to Linear Programming*, McGraw-Hill, 1960, ISBN 978-0-070-22910-5.

[47] M. Avriel, *Nonlinear Programming: Analysis and Methods*, Dover, 2003, ISBN 978-0-486-43227-4.

[48] J.A. Nelder and R. Mead, *A simplex method for function minimization*, Computer Journal, (7) 1965, pp. 308-313.

[49] M.J. Box, *A new method of constrained optimization and a comparison with other method*, Computer Journal, (8-1) 1965, pp. 42-52.

[50] J. Guin, *Modification of the Complex method of constraint optimization*, Computer Journal, (10) 1968, pp. 416-417.

[51] P. Krus et al., *Optimization Based on Simulation for Design of Fluid Power Systems*, Proceedings of ASME Winter Annual Meeting, 1992, Anaheim, USA.

[52] J. Andersson, *Multiobjective Optimization in Engineering Design: Applications to Fluid Power Systems*, Doctoral Thesis, 2001, Linköpings Universitet, Sweden.

[53] N.K. Sahoo et al., *Modified complex method for constrained design and optimization of optical multilayer thin-film devices*, Applied Physics A-Solids & Surfaces, (59) 1994, pp. 317-326.

[54] M.I. Haque, *Optimal frame design with discrete members using the complex method*, Computers & Structures, (59) 1996, pp. 847-858.

[55] The Mathworks Inc., Matlab, R2019b, 2019.

[56] F. Edemetti et al., *Thermal-hydraulic analysis of the DEMO WCLL elementary cell: BZ tubes layout optimization*, Fusion Engineering and Design, (160) 2020, 111956, DOI:10.1016/j.fusengdes.2020.111956

[57] F. Edemetti et al., *Optimization of the first wall cooling system for the DEMO WCLL blanket*, Fusion Engineering and Design, (161) 2020, 111903, DOI:10.1016/j.fusengdes.2020.111903

[58] I. Catanzaro et al., *Parametric study of the influence of double-walled tubes layout on the DEMO WCLL breeding blanket thermal performances*, Fusion Engineering and Design, (161) 2020, 111893, DOI:10.1016/j.fusengdes.2020.111893

[59] J. Aubert et al., *Design and preliminary analyses of the new Water Cooled Lithium Lead TBM for ITER*, Fusion Engineering and Design, (160) 2020, 111921, DOI:10.1016/j.fusengdes.2020.111921

[60] L. Maqueda et al., *Thermal-mechanical analysis in support of WCLL BB: ESTEYCO contribution*, Internal Deliverable BB-3.2.1-T005-D003, 2019, EUROfusion IDM, Ref.:EFDA_D_2NY8VX

[61] U. Fischer et al., *Neutronics requirements for a DEMO fusion power plant*, Fusion Engineering and Design, (98-99) 2015, pp. 2134-2137, DOI:10.1016/j.fusengdes.2015.02.029

[62] L.S. Tong, *A phenomcnological study of critical heat flux*, ASME Paper, 75-HT-68, 1975.

[63] RCC-MRx, Design and Construction Rules for Mechanical Components of Nuclear Installations, AFCEN, 2013.

[64] J. Aubert et al., *Contribution for WCLL TBM specificity to methodology for steady-state calculations, design criteria and SLS*, PMI-7.1.1.Task 2-T002-D001 Deliverable D3.1, 2019, EUROfusion IDM, Ref.:EFDA_D_2LP589

[65] D. Annaratone, *Pressure Vessel Design*, Springer, 2007, ISBN 978-3-540-49144-6

[66] ITER SDC-IC, Appendix A, Materials Design Limit Data, 2013, ITER IDM, Ref.:ITER_D_222RLN.

[67] D. Martelli et al., *Literature review of lead-lithium thermophysical properties*, Fusion Engineering and Design, (138) 2019, pp. 183-195, DOI:10.1016/j.fusengdes.2018.11.028

[68] P. Chiovaro et al., *Neutronics: Design Analyses*, Presentation at the WCLL BB Design Review Meeting 2019, July 8-10, 2019.

[69] P. Chiovaro et al., *Parametric study of the influence of First Wall cooling water on the Water Cooled Lithium Lead Breeding Blanket nuclear response*, Fusion Engineering and Design, (146-B) 2019, pp. 2070-2073, DOI:10.1016/j.fusengdes.2019.03.105

[70] F. Incropera, *Fundamentals of Heat and Mass Transfer*, Wiley, 1985, ISBN 978-0-471-88550-4.

[71] G. Bongiovì, Private Communication, March, 2020.

[72] G.A. Spagnuolo et al., *A multi-physics integrated approach to breeding blanket modelling and design*, Fusion Engineering and Design, (143) 2019, pp. 35-40, DOI:10.1016/j.fusengdes.2019.03.131

[73] R. Favetti et al., *Validation of Multi-Physics Integrated Procedure for the HCPB Breeding Blanket*, International Journal of Computational Methods, (17-6) 2020, 19500099, DOI:10.1142/S0219876219500099

[74] X-5 Monte Carlo Team, *MCNP—A General Monte Carlo N-Particle Transport Code*, Version 5, LANL, Los Alamos, New Mexico, USA, 2003.

[75] JEFF3.2 Nuclear Data Library, *http://www.oecd-nea.org/*, 2008.

[76] D. She, *On the white boundary condition in Monte Carlo simulation*, Annals of Nuclear Energy, (132) 2019, pp. 413-414, DOI:10.1016/j.anucene.2019.05.006

[77] I. Idelchik, *Handbook of Hydraulic Resistance*, Begell House, 2007, ISBN 978-1-567-00251-5.

[78] S.E. Haaland, *Simple and Explicit Formulas for the Friction Factor in Turbulent Flow*, Journal of Fluids Engineering, (105-1) 1983, pp. 89-90, DOI:10.1115/1.3240948

[79] A.R. Raffray et al., *Critical heat flux analysis and R&D for the design of the ITER divertor*, Fusion Engineering and Design, (45-4) 1999, pp. 377-407, DOI:10.1016/S0920-3796(99)00053-8.

[80] J. Aktaa, *High Temperature Creep-Fatigue Structural Design Criteria for Fusion Components Built from EUROFER 97*, Final Report: TW2-TTMS-005b and TW5-TTMS-005, Forschungszentrum Karlsruhe, August, 2007.

Appendices

A Matlab Code for Complex Method Validation

```
%% Validation of author's Complex Method implementation
%
clear all
clc
%
%  Author:
%
%    Ruggero Forte
%
%  Parameters:
%
cont=0;
%
%  Define algorithm constants
%
alpha = 1.3;     % rho > 0
tol = 1e-4;
%
max_feval = 1000;
k_max = 8;
%
%  Initialization
%
n_dim=2;
x=zeros(2*n_dim, n_dim);
x_bar=zeros(1,n_dim);
x_h=zeros(1,n_dim);
y=zeros(2*n_dim,1);
f_bar=zeros(1,max_feval);
stndev=zeros(1,max_feval);
```

```
%
x0 = [8  0.5];
x(1,:)=x0;
%
sigma_y=500;
%
%  Define variables boundaries
%
B=zeros(2,n_dim);
B(1,1) = 2; % N low
B(2,1) = 14; % N up
B(1,2) = 0.2; % R low
B(2,2) = 0.8; % R up
%
%  Define initial complex
%
rng('shuffle')
for i=2:(2*n_dim)
    x(i,1)=B(1,1)+rand*(B(2,1)-B(1,1));
    x(i,2)=B(1,2)+rand*(B(2,2)-B(1,2));
end
%
%  Assess and adjust initial complex
%
for i=1:(2*n_dim)
    sigma_b=(pi^2)*(0.85e6)*(x(i,1)^2+x(i,2)^2)/(8*250^2);
    sigma=2500/(pi*x(i,1)*x(i,2));
    cont=cont+1;
    if (sigma <= sigma_y) && (sigma <= sigma_b)
        y(i,1)=9.81*x(i,1)*x(i,2)+2*x(i,1); % objective function f(x)
    else
        k=1;
        for j=1:n_dim
            x_bar(1,j) = sum(x(1:(i-1),j))/(i-1);
        end
        while (sigma > sigma_y) || (sigma > sigma_b)
            if k > k_max
                error('k is greater than k_max')
            end
            for j=1:n_dim
```

```
71                      x(i,j)=(x_bar(1,j)+x(i,j))/2;
72                      if (x(i,j) >= B(1,j) && x(i,j) <= B(2,j))
73                          x(i,j)=x(i,j);
74                      else
75                          if x(i,j) < B(1,j)
76                              x(i,j)=B(1,j);
77                          elseif x(i,j) > B(2,j)
78                              x(i,j)=B(2,j);
79                          end
80                      end
81                  end
82                  sigma_b=(pi^2)*(0.85e6)*(x(i,1)^2+x(i,2)^2)/(8*250^2);
83                  sigma=2500/(pi*x(i,1)*x(i,2));
84                  cont=cont+1;
85                  k=k+1;
86              end
87              y(i,1)=9.81*x(i,1)*x(i,2)+2*x(i,1);
88          end
89      end
90      %
91      %  Begin Complex method iterations
92      %
93      t=1;
94      m=0;
95      %
96      x_start=x;
97      y_start=y;
98      x_bar=sum(x(1:2*n_dim,:))/(2*n_dim);
99      f_bar(1,t)=9.81*x_bar(1,1)*x_bar(1,2)+2*x_bar(1,1);
100     z=0;
101     for j=1:(2*n_dim)
102         eps=(f_bar(1,t)-y(j))^2;
103         z=z+eps;
104     end
105     stndev(1,t)=sqrt(z/(2*n_dim));
106     res=stndev(1,t);
107     %
108     while ( res > tol && cont <= max_feval)
109         %
110         [f_h,i_h]=max(y);
```

```
111     [f_l,i_l]=min(y);
112     if m==1
113         f_h=max(y(y<max(y)));
114         i_h=find(y == f_h);
115     end
116     if m==2
117         f_h=max(y(y<(max(y(y<max(y))))));
118         i_h=find(y == f_h);
119     end
120     if m==3
121         f_h=max(y(y<(max(y(y<(max(y(y<max(y)))))))));
122         i_h=find(y == f_h);
123     end
124     if m==4
125         error('m is equal to 4')
126     end
127         x_h=x(i_h,:);
128         x_l=x(i_l,:);
129         x(i_h,:)=zeros(1,n_dim);
130         x_bar=sum(x(1:2*n_dim,:))/(2*n_dim-1);
131     %
132     %  Compute the reflected point
133     %
134     %
135     x_r   = ( 1 + alpha ) * x_bar - alpha * x_h;
136     %
137     for j=1:n_dim
138         if (x_r(1,j) >= B(1,j) && x_r(1,j) <= B(2,j))
139             x_r(1,j)=x_r(1,j);
140         else
141             if x_r(1,j) < B(1,j)
142                 x_r(1,j)=B(1,j);
143             elseif x_r(1,j) > B(2,j)
144                 x_r(1,j)=B(2,j);
145             end
146         end
147     end
148     %
149     sigma_b=(pi^2)*(0.85e6)*(x_r(1,1)^2+x_r(1,2)^2)/(8*250^2);
150     sigma=2500/(pi*x_r(1,1)*x_r(1,2));
```

```
151     cont=cont+1;
152     f_r=9.81*x_r(1,1)*x_r(1,2)+2*x_r(1,1);
153     %
154     %  Accept the point
155     %
156     k=1;
157     if ( f_r <= f_h ) && (sigma <= sigma_y) && (sigma <= sigma_b)
158         x(i_h,:) = x_r;
159         y(i_h,1) = f_r;
160     else
161         while f_r > f_h || (sigma > sigma_y) || (sigma > sigma_b)
162             if k > k_max
163                 break
164             end
165             arg=(4/(4+k-1))^((4+k-1)/4);
166             for j=1:n_dim
167                 rng('shuffle')
168                 x_r(1,j)=(x_r(1,j)+arg*x_bar(1,j)+(1-arg)*...
169                 x_l(1,j))/2+(x_bar(1,j)-x_l(1,j))*(1-arg)*(2*rand-1);
170             end
171             for j=1:n_dim
172                 if (x_r(1,j) >= B(1,j) && x_r(1,j) <= B(2,j))
173                     x_r(1,j)=x_r(1,j);
174                 else
175                     if x_r(1,j) < B(1,j)
176                         x_r(1,j)=B(1,j);
177                     elseif x_r(1,j) > B(2,j)
178                         x_r(1,j)=B(2,j);
179                     end
180                 end
181             end
182             sigma_b=(pi^2)*(0.85e6)*(x_r(1,1)^2+x_r(1,2)^2)/(8*250^2);
183             sigma=2500/(pi*x_r(1,1)*x_r(1,2));
184             cont=cont+1;
185             k=k+1;
186             f_r=9.81*x_r(1,1)*x_r(1,2)+2*x_r(1,1);
187         end
188     end
189     %
190     if (f_r <= f_h) && (sigma <= sigma_y) && (sigma <= sigma_b)
```

```
191             x(i_h,:) = x_r;
192             y(i_h,1) = f_r;
193             m=0;
194             k=1;
195             t=t+1;
196         end
197         %
198         if f_r > f_h || k > k_max
199             x(i_h,:)=x_h;
200             m=m+1;
201         end
202         %
203         %  Test for convergence
204         %
205         x_bar=sum(x(1:2*n_dim,:))/(2*n_dim);
206         f_bar(1,t)=9.81*x_bar(1,1)*x_bar(1,2)+2*x_bar(1,1);
207         z=0;
208         for j=1:(2*n_dim)
209             eps=(f_bar(1,t)-y(j))^2;
210             z=z+eps;
211         end
212         stndev(1,t)=sqrt(z/(2*n_dim));
213         res=stndev(1,t);
214     end
```

B Matlab Code for FW Optimization

```
%% Complex Method implementation for FW Optimization
%
%  Author:
%
%    Ruggero Forte
%
% Link to COMSOL model
model = mphopen('C:\Folder\Model.mph');
ModelUtil.setServerBusyHandler(ServerBusyHandler(2));
ModelUtil.showProgress(true);
%
%  Parameters:
%
cont=0;
%
%  Define constants
%
alpha = 1.3;
tol = 1e-2;
n=1.05; % safety factor
beta=0.01;
gamma=1.75E-4;
%
max_feval = 250;
k_max = 8;
%
cp_w = 5791.77; % [J/(kg*K)] specific heat water at 311.5 C
deltaT = 33;
q_dwt_water = 6658.906; % NH in DWTs water [W]
q_fw_water = 10224.417; % NH in FW-SWs water [W]
%
%  Initialization
%
n_dim=4;
x=zeros(2*n_dim, n_dim);
x_bar=zeros(1,n_dim);
x_h=zeros(1,n_dim);
y=zeros(2*n_dim,1);
```

```
39 f_bar=zeros(1,max_feval);
40 stndev=zeros(1,max_feval);
41 %
42 % x0 = [7 13 7 4];
43 x0 = [6 14 7 7];
44 x(1,:)=x0;
45 %
46 %
47 %  Define variables boundaries
48 %
49 s=2;
50 H=135;
51 fw_thk=25;
52 %
53 B=zeros(2,n_dim);
54 B(1,1) = 4; % N low
55 B(2,1) = 10; % N up
56 B(1,2) = s; % R low
57 B(1,3) = 4; % a low
58 B(2,2) = fw_thk-B(1,3)-s; % R up
59 B(1,4) = 4; % b low
60 % a_up is dependent on R
61 % b_up is dependent on N
62 %
63 %  Build up initial complex
64 %
65 %
66 rng('shuffle')
67 for i=2:(2*n_dim)
68 x(i,1)=round(B(1,1)+rand*(B(2,1)-B(1,1)));
69 x(i,2)=B(1,2)+rand*(B(2,2)-B(1,2));
70 B(2,3) = fw_thk-x(i,2)-s; % a up
71 x(i,3)=B(1,3)+rand*(B(2,3)-B(1,3));
72 B(2,4) = (H-x(i,1)*s)/x(i,1); % b up
73 x(i,4)=B(1,4)+rand*(B(2,4)-B(1,4));
74 end
75 %
76 %  Check the feasibility of the initial complex
77 %
78 %
```

```
for i=1:(2*n_dim)
model.param.set('N',[num2str(x(i,1)),'[1]']);
model.param.set('R',[num2str(x(i,2)),'[mm]']);
model.param.set('a',[num2str(x(i,3)),'[mm]']);
model.param.set('b',[num2str(x(i,4)),'[mm]']);
u=0;
while u<2 % BZ
model.study('std1').run;
q_dwt=2*(abs(mphglobal(model,'q_dwt','dataset','dset1')))+q_dwt_water;
mfr_dwt=q_dwt/(deltaT*cp_w);
q_fw=2*(abs(mphglobal(model,'q_fw','dataset','dset1')))+q_fw_water;
mfr_fw=q_fw/(deltaT*cp_w);
model.param.set('mfr_dwt',[num2str(mfr_dwt),'[kg/s]']);
model.param.set('mfr_fw',[num2str(mfr_fw),'[kg/s]']);
u=u+1;
end
model.study('std2').run;
model.study('std3').run;
Stress_Linearization_Opt;
cont=cont+1;
if (mphglobal(model,'u_fw','dataset','dset2') <= 7) &&...
(mphglobal(model,'maxTemp','dataset','dset2') <= 823.15) &&...
(mphglobal(model,'aveTemp1','dataset','dset2') >= 623.15) &&...
(mphglobal(model,'aveTemp2','dataset','dset2') >= 623.15) &&...
(mphglobal(model,'aveTemp3','dataset','dset2') >= 623.15) &&...
(mphglobal(model,'aveTemp4','dataset','dset2') >= 623.15) &&...
(mphglobal(model,'aveTemp5','dataset','dset2') >= 623.15) &&...
(mphglobal(model,'aveTemp6','dataset','dset2') >= 623.15) &&...
(mphglobal(model,'aveTemp9','dataset','dset2') >= 623.15) &&...
(mphglobal(model,'aveTemp10','dataset','dset2') >= 623.15) &&...
(sl <= 1/n)
y(i,1)=1/(x(i,1)*x(i,3)*x(i,4))+...
gamma*x(i,2)*(x(i,1)*x(i,4))^beta;
y(i,1)=y(i,1)*1000;
else
k=1;
for j=1:n_dim
x_bar(1,j) = sum(x(1:(i-1),j))/(i-1);
end
while (mphglobal(model,'u_fw','dataset','dset2') > 7) ||...
```

```
(mphglobal(model,'maxTemp','dataset','dset2') > 823.15) ||...
(mphglobal(model,'aveTemp1','dataset','dset2') < 623.15) ||...
(mphglobal(model,'aveTemp2','dataset','dset2') < 623.15) ||...
(mphglobal(model,'aveTemp3','dataset','dset2') < 623.15) ||...
(mphglobal(model,'aveTemp4','dataset','dset2') < 623.15) ||...
(mphglobal(model,'aveTemp5','dataset','dset2') < 623.15) ||...
(mphglobal(model,'aveTemp6','dataset','dset2') < 623.15) ||...
(mphglobal(model,'aveTemp9','dataset','dset2') < 623.15) ||...
(mphglobal(model,'aveTemp10','dataset','dset2') < 623.15) ||...
(sl > 1/n)
if k > k_max
error('k is greater than k_max')
end
for j=1:n_dim
x(i,j)=(x_bar(1,j)+x(i,j))/2;
if j==1
x(i,j)=round(x(i,j)); % round(N)
if k==k_max
x(i,j)=round(x_bar(1,j));
end
end
if j==3
B(2,j)=fw_thk-x(i,2)-s; % a up
end
if j==4
B(2,j)=(H-x(i,1)*s)/x(i,1); % b up
end
if (x(i,j) >= B(1,j) && x(i,j) <= B(2,j))
x(i,j)=x(i,j);
else
if x(i,j) < B(1,j)
x(i,j)=B(1,j);
elseif x(i,j) > B(2,j)
x(i,j)=B(2,j);
end
end
end
model.param.set('N',[num2str(x(i,1)),'[1]']);
model.param.set('R',[num2str(x(i,2)),'[mm]']);
model.param.set('a',[num2str(x(i,3)),'[mm]']);
```

```
159 model.param.set('b',[num2str(x(i,4)),'[mm]']);
160 u=0;
161 while u<2 % BZ
162 model.study('std1').run;
163 q_dwt=2*(abs(mphglobal(model,'q_dwt','dataset','dset1')))+q_dwt_water;
164 mfr_dwt=q_dwt/(deltaT*cp_w);
165 q_fw=2*(abs(mphglobal(model,'q_fw','dataset','dset1')))+q_fw_water;
166 mfr_fw=q_fw/(deltaT*cp_w);
167 model.param.set('mfr_dwt',[num2str(mfr_dwt),'[kg/s]']);
168 model.param.set('mfr_fw',[num2str(mfr_fw),'[kg/s]']);
169 u=u+1;
170 end
171 model.study('std2').run;
172 model.study('std3').run;
173 Stress_Linearization_Opt;
174 cont=cont+1;
175 k=k+1;
176 end
177 y(i,1)=1/(x(i,1)*x(i,3)*x(i,4))+...
178 gamma*x(i,2)*(x(i,1)*x(i,4))^beta;
179 y(i,1)=y(i,1)*1000;
180 end
181 end
182 %
183 % Begin the Complex method reflection process
184 %
185 t=1;
186 m=0;
187 %
188 x_start=x;
189 y_start=y;
190 x_bar=sum(x(1:2*n_dim,:))/(2*n_dim);
191 f_bar(1,t)=1/(x_bar(1,1)*x_bar(1,3)*x_bar(1,4))+...
192 gamma*x_bar(1,2)*(x_bar(1,1)*x_bar(1,4))^beta;
193 f_bar(1,t)=f_bar(1,t)*1000;
194 z=0;
195 for j=1:(2*n_dim)
196 eps=(f_bar(1,t)-y(j))^2;
197 z=z+eps;
198 end
```

```
199 stndev(1,t)=sqrt(z/(2*n_dim));
200 res=stndev(1,t);
201 %
202 while ( res > tol && cont <= max_feval)
203 [f_h,i_h]=max(y);
204 [f_l,i_l]=min(y);
205 if m==1
206 f_h=max(y(y<max(y)));
207 i_h=find(y == f_h);
208 end
209 if m==2
210 f_h=max(y(y<(max(y(y<max(y))))));
211 i_h=find(y == f_h);
212 end
213 if m==3
214 f_h=max(y(y<(max(y(y<(max(y(y<max(y)))))))));
215 i_h=find(y == f_h);
216 end
217 if m==4
218 error('m is equal to 4')
219 end
220 x_h=x(i_h,:);
221 x_l=x(i_l,:);
222 x(i_h,:)=zeros(1,n_dim);
223 x_bar=sum(x(1:2*n_dim,:))/(2*n_dim-1);
224 %
225 %  Compute the reflected point
226 %
227 %
228 x_r   = ( 1 + alpha ) * x_bar - alpha * x_h;
229 %
230 for j=1:n_dim
231 if j==1
232 x_r(1,j)=round(x_r(1,j)); % round(N)
233 end
234 if j==3
235 B(2,j)=fw_thk-x_r(1,2)-s; % a up
236 end
237 if j==4
238 B(2,j)=(H-x_r(1,1)*s)/x_r(1,1); % b up
```

```
239 end
240 if (x_r(1,j) >= B(1,j) && x_r(1,j) <= B(2,j))
241 x_r(1,j)=x_r(1,j);
242 else
243 if x_r(1,j) < B(1,j)
244 x_r(1,j)=B(1,j);
245 elseif x_r(1,j) > B(2,j)
246 x_r(1,j)=B(2,j);
247 end
248 end
249 end
250 %
251 model.param.set('N',[num2str(x_r(1,1)),'[1]']);
252 model.param.set('R',[num2str(x_r(1,2)),'[mm]']);
253 model.param.set('a',[num2str(x_r(1,3)),'[mm]']);
254 model.param.set('b',[num2str(x_r(1,4)),'[mm]']);
255 u=0;
256 while u<2 % BZ
257 model.study('std1').run;
258 q_dwt=2*(abs(mphglobal(model,'q_dwt','dataset','dset1')))+q_dwt_water;
259 mfr_dwt=q_dwt/(deltaT*cp_w);
260 q_fw=2*(abs(mphglobal(model,'q_fw','dataset','dset1')))+q_fw_water;
261 mfr_fw=q_fw/(deltaT*cp_w);
262 model.param.set('mfr_dwt',[num2str(mfr_dwt),'[kg/s]']);
263 model.param.set('mfr_fw',[num2str(mfr_fw),'[kg/s]']);
264 u=u+1;
265 end
266 model.study('std2').run;
267 model.study('std3').run;
268 Stress_Linearization_Opt;
269 cont=cont+1;
270 f_r=1/(x_r(1,1)*x_r(1,3)*x_r(1,4))+...
271 gamma*x_r(1,2)*(x_r(1,1)*x_r(1,4))^beta;
272 f_r=f_r*1000;
273 %
274 % Accept the point:
275 %
276 k=1;
277 if ( f_r <= f_h ) && (mphglobal(model,'u_fw','dataset','dset2') <= 7) &
278 (mphglobal(model,'maxTemp','dataset','dset2') <= 823.15) &&...
```

```
(mphglobal(model,'aveTemp1','dataset','dset2') >= 623.15) &&...
(mphglobal(model,'aveTemp2','dataset','dset2') >= 623.15) &&...
(mphglobal(model,'aveTemp3','dataset','dset2') >= 623.15) &&...
(mphglobal(model,'aveTemp4','dataset','dset2') >= 623.15) &&...
(mphglobal(model,'aveTemp5','dataset','dset2') >= 623.15) &&...
(mphglobal(model,'aveTemp6','dataset','dset2') >= 623.15) &&...
(mphglobal(model,'aveTemp9','dataset','dset2') >= 623.15) &&...
(mphglobal(model,'aveTemp10','dataset','dset2') >= 623.15) &&...
(sl <= 1/n)
x(i_h,:) = x_r;
y(i_h,1) = f_r;
else
while f_r > f_h || (mphglobal(model,'u_fw','dataset','dset2') > 7) ||...
(mphglobal(model,'maxTemp','dataset','dset2') > 823.15) ||...
(mphglobal(model,'aveTemp1','dataset','dset2') < 623.15) ||...
(mphglobal(model,'aveTemp2','dataset','dset2') < 623.15) ||...
(mphglobal(model,'aveTemp3','dataset','dset2') < 623.15) ||...
(mphglobal(model,'aveTemp4','dataset','dset2') < 623.15) ||...
(mphglobal(model,'aveTemp5','dataset','dset2') < 623.15) ||...
(mphglobal(model,'aveTemp6','dataset','dset2') < 623.15) ||...
(mphglobal(model,'aveTemp9','dataset','dset2') < 623.15) ||...
(mphglobal(model,'aveTemp10','dataset','dset2') < 623.15) ||...
(sl > 1/n)
if k > k_max
break
end
arg=(4/(4+k-1))^((4+k-1)/4);
for j=1:n_dim
rng('shuffle')
x_r(1,j)=(x_r(1,j)+arg*x_bar(1,j)+(1-arg)*x_l(1,j))/2+...
(x_bar(1,j)-x_l(1,j))*(1-arg)*(2*rand-1);
end
for j=1:n_dim
if j==1
x_r(1,j)=round(x_r(1,j)); % round(N)
if k==k_max
x_r(1,j)=round(x_bar(1,j));
end
end
if j==3
```

```
319 B(2,j)=fw_thk-x_r(1,2)-s; % a up
320 end
321 if j==4
322 B(2,j)=(H-x_r(1,1)*s)/x_r(1,1); % b up
323 end
324 if (x_r(1,j) >= B(1,j) && x_r(1,j) <= B(2,j))
325 x_r(1,j)=x_r(1,j);
326 else
327 if x_r(1,j) < B(1,j)
328 x_r(1,j)=B(1,j);
329 elseif x_r(1,j) > B(2,j)
330 x_r(1,j)=B(2,j);
331 end
332 end
333 end
334 model.param.set('N',[num2str(x_r(1,1)),'[1]']);
335 model.param.set('R',[num2str(x_r(1,2)),'[mm]']);
336 model.param.set('a',[num2str(x_r(1,3)),'[mm]']);
337 model.param.set('b',[num2str(x_r(1,4)),'[mm]']);
338 u=0;
339 while u<2 % BZ
340 model.study('std1').run;
341 q_dwt=2*(abs(mphglobal(model,'q_dwt','dataset','dset1')))+q_dwt_water;
342 mfr_dwt=q_dwt/(deltaT*cp_w);
343 q_fw=2*(abs(mphglobal(model,'q_fw','dataset','dset1')))+q_fw_water;
344 mfr_fw=q_fw/(deltaT*cp_w);
345 model.param.set('mfr_dwt',[num2str(mfr_dwt),'[kg/s]']);
346 model.param.set('mfr_fw',[num2str(mfr_fw),'[kg/s]']);
347 u=u+1;
348 end
349 model.study('std2').run;
350 model.study('std3').run;
351 Stress_Linearization_Opt;
352 cont=cont+1;
353 k=k+1;
354 f_r=1/(x_r(1,1)*x_r(1,3)*x_r(1,4))+...
355 gamma*x_r(1,2)*(x_r(1,1)*x_r(1,4))^beta;
356 f_r=f_r*1000;
357 end
358 end
```

```
%
if (f_r <= f_h) &&...
(mphglobal(model,'u_fw','dataset','dset2') <= 7) &&...
(mphglobal(model,'maxTemp','dataset','dset2') <= 823.15) &&...
(mphglobal(model,'aveTemp1','dataset','dset2') >= 623.15) &&...
(mphglobal(model,'aveTemp2','dataset','dset2') >= 623.15) &&...
(mphglobal(model,'aveTemp3','dataset','dset2') >= 623.15) &&...
(mphglobal(model,'aveTemp4','dataset','dset2') >= 623.15) &&...
(mphglobal(model,'aveTemp5','dataset','dset2') >= 623.15) &&...
(mphglobal(model,'aveTemp6','dataset','dset2') >= 623.15) &&...
(mphglobal(model,'aveTemp9','dataset','dset2') >= 623.15) &&...
(mphglobal(model,'aveTemp10','dataset','dset2') >= 623.15) &&...
(sl <= 1/n)
x(i_h,:) = x_r;
y(i_h,1) = f_r;
m=0;
k=1;
t=t+1;
end
%
if f_r > f_h || k > k_max
x(i_h,:)=x_h;
m=m+1;
end
%
%  Test for convergence
%
x_bar=sum(x(1:2*n_dim,:))/(2*n_dim);
f_bar(1,t)=1/(x_bar(1,1)*x_bar(1,3)*x_bar(1,4))+...
gamma*x_bar(1,2)*(x_bar(1,1)*x_bar(1,4))^beta;
f_bar(1,t)=f_bar(1,t)*1000;
z=0;
for j=1:(2*n_dim)
eps=(f_bar(1,t)-y(j))^2;
z=z+eps;
end
stndev(1,t)=sqrt(z/(2*n_dim));
res=stndev(1,t);
end
```

C Further Details of the Optimization Campaign Results

In this appendix, the main outcomes referred to the optimum design point drawn from the results of the five optimization runs carried out are reported. As already explained in Chapter 3, the optimization process works with a sequential procedure where the worst point of the complex is substituted by a new reflected point with lower objective function value and compliant with all the constraints. Hence, every time a new point is computed, its feasibility must be checked before it get accepted.

The great majority of the functional constraints imposed concerns the thermal-hydraulic and the thermo-structural performances of the blanket and, hence, is evaluated by means of the numerical model set-up in COMSOL. Referring to the optimum design point, identified as the point of the complex with the lowest objective function value obtained at the end of Run #5 (N=5, R=6.194 mm, a=13.744 mm and b=19.497 mm), the steady-state thermal field arising within the corresponding equatorial cell under the effect of the thermal loads and boundary conditions is reported in Figure C.1. As shown in the contour plots, the overall

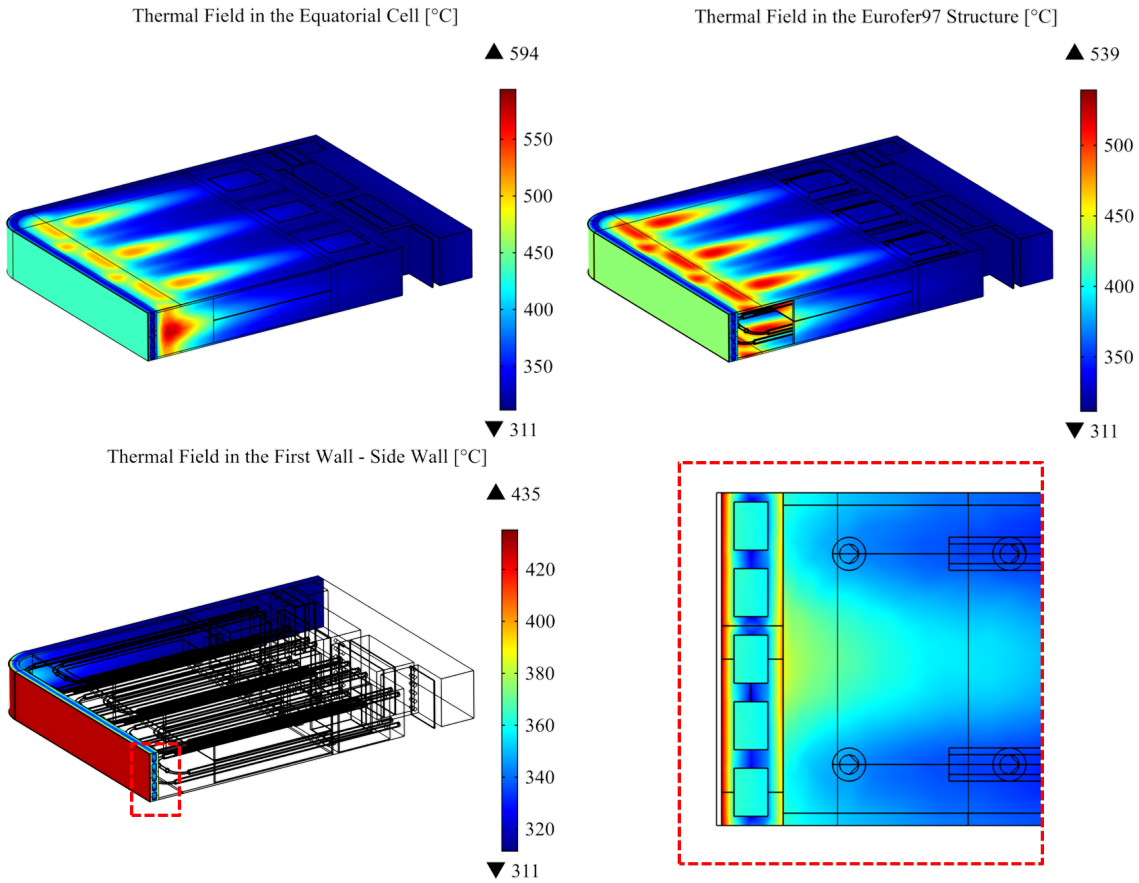

Figure C.1: Temperature distribution obtained at the end of the Run #5.

maximum temperature of 594 °C is reached in the breeder domain, whereas the maximum temperature reached in the Eurofer domain is equal to 539 °C. Looking

at the FW-SW, the maximum temperature obtained is in the plasma-facing region, equal to 435 °C.

The related thermal-hydraulic functional constraints evaluated from the FEM thermal analysis are reported in Table C.1. Just as a reminder, the $T_{Eurofer,max}$ variable does not include the Baffle plate (where the maximum temperature in the Eurofer domain is obtained) because such component does not play any structural role and no limit on its maximum temperature is needed.

Constraint	**Parameter**	**Value**
$u_{FW} \leq 7$ m/s	u_{FW}	0.877 m/s
$T_{Eurofer,max} \leq 550$ °C	$T_{Eurofer,max}$	520.8 °C
$T_{SL1,ave} \geq 350$ °C	$T_{SL1,ave}$	366.8 °C
$T_{SL2,ave} \geq 350$ °C	$T_{SL2,ave}$	376.5 °C
$T_{SL3,ave} \geq 350$ °C	$T_{SL3,ave}$	394.5 °C
$T_{SL4,ave} \geq 350$ °C	$T_{SL4,ave}$	351.2 °C
$T_{SL5,ave} \geq 350$ °C	$T_{SL5,ave}$	351.8 °C
$T_{SL6,ave} \geq 350$ °C	$T_{SL6,ave}$	378.3 °C
$T_{SL9,ave} \geq 350$ °C	$T_{SL10,ave}$	394.9 °C

Table C.1: Thermal-hydraulic constraints evaluated for the optimum design point.

From the structural point of view, the results obtained in terms of Von Mises stress field in the FW-SW are reported in Figure C.2. In particular, three different results were needed in order to apply the RCC-MRx rules: (1) one linear elastic analysis considering only the primary loads (i.e. pressure loads) related to the NO scenario, (2) one linear elastic analysis considering only the primary loads related to the OP scenario and (3) one linear elastic analysis considering only the secondary loads (i.e. thermal expansion) related to the NO scenario. As shown in the plots, under normal operation conditions the pressure load onto the FW does not generate high stresses, with except of the manifold part where a stress concentration has been observed. Conversely, the secondary stresses, but also the primary stresses arising during the OP accidental scenario, reach higher values and play a pivotal role in the FW design.

Finally, the verification of the main RCC-MRx design rules, adopted as functional constraints, on the final configuration obtained during Run #5 is reported in Table C.2. Looking at the table, all the utilization factors are lower than 1 and meaning that all the selected criteria are fulfilled. It is also interesting to note that none of the thickness analysed need to be checked against creep failure, because the average temperature along the supporting lines is always lower than 425 °C.

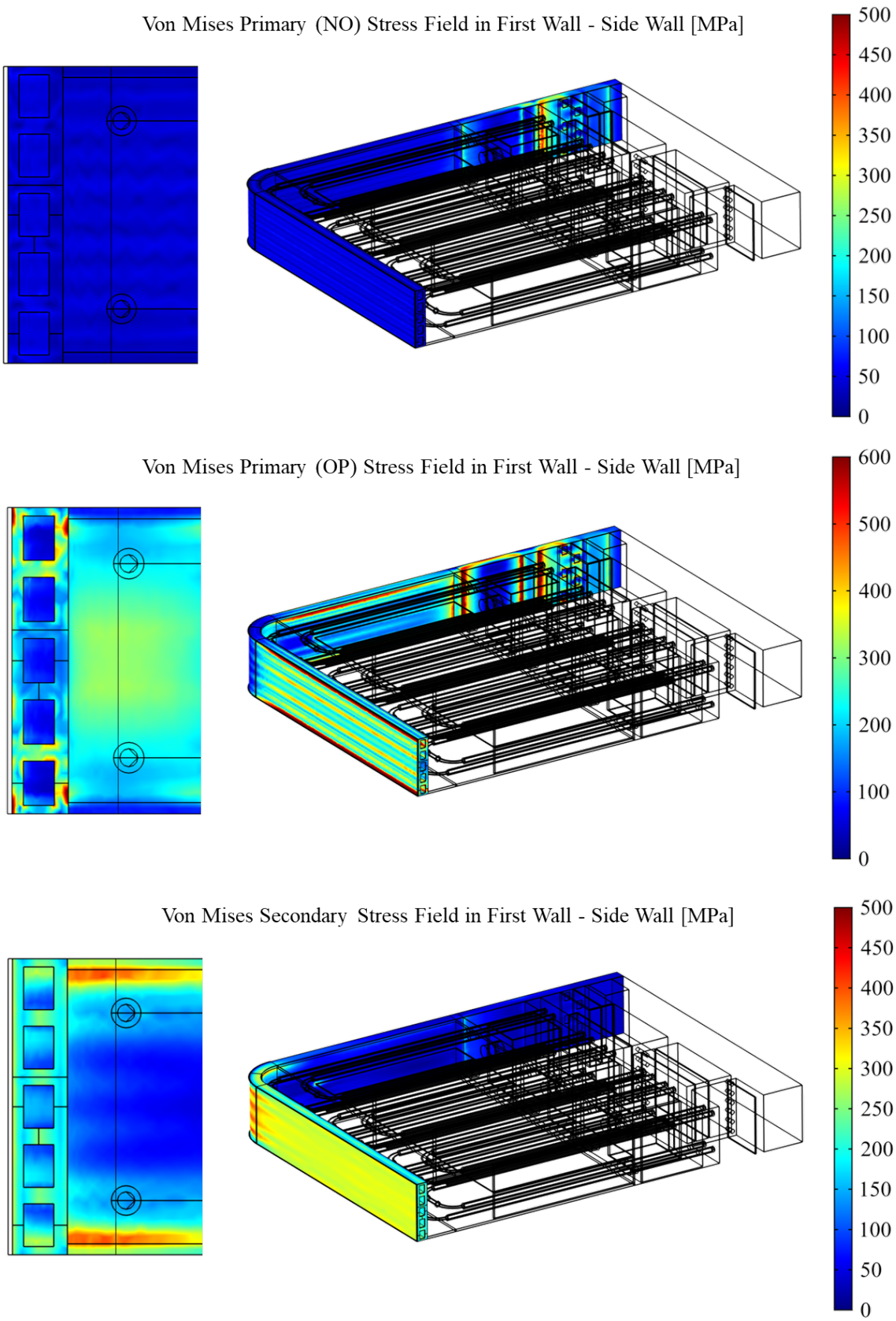

Figure C.2: Von Mises stress distribution obtained at the end of the Run #5.

Criterion	**SL1**	**SL2**	**SL3**	**SL4**	**SL5**	**SL6**	**SL7**	**SL8**	**SL9**	**SL10**
$(\overline{P_m})_A/S_{m,A}$	0.145	0.113	0.174	0.149	0.111	0.171	0.237	0.241	0.148	0.150
$(\overline{P_L + P_b})_A/1.5S_{m,A}$	0.102	0.138	0.276	0.111	0.164	0.204	0.170	0.170	0.185	0.223
$(\overline{P_m + Q_m})_A/S_{em,A}$	0.601	0.520	0.570	0.326	0.237	0.482	0.834	0.429	0.616	0.592
$(\Omega\overline{P_m})_A/S_t$	-	-	-	-	-	-	-	-	-	-
$(\overline{P_L + \Phi P_b})_A/S_t$	-	-	-	-	-	-	-	-	-	-
$(\max\left[\overline{P_L + P_b}\right] + \overline{\Delta Q})_A/3S_{m,A}$	0.404	0.456	0.705	0.294	0.207	0.596	0.555	0.302	0.552	0.669
$(\overline{P_m})_D/S_{m,D}$	0.352	0.402	0.680	0.344	0.698	0.176	0.450	0.332	0.943	0.729
$(\overline{P_L + P_b})_D/1.5S_{m,D}$	0.307	0.336	0.586	0.537	0.593	0.174	0.334	0.227	0.742	0.576
$(\overline{P_m + Q_m})_D/S_{em,D}$	0.556	0.555	0.345	0.378	0.601	0.234	0.781	0.453	0.697	0.696

Table C.2: Structural constraints evaluated for the optimum design point (satisfied if value is lower than 1).